Workshop of

Experimental Nuclear and Particle Physics

2019

13.–19. 01. 2019, Bílý Potok

Faculty of Nuclear Sciences and Physical Engineering
Czech Technical University in Prague

Workshop of Experimental Nuclear and Particle Physics 2019
Editors: L. Novotný, R. Novotný
Issued by: Czech Technical University in Prague
Faculty of Nuclear Sciences and Physical Engineering
Address: KF FJFI ČVUT, Břehová 7, 115 19 Praha 1
novotr14@fjfi.cvut.cz, +420731891801
Available at `http://wejcf2019.ejcf.cz/wejcf2019_proceedings.pdf`
First edition. 100 pages.

Contents

Foreword

This year, for the 13$^{\text{th}}$ time, students, graduates, and teachers from the field of Experimental Nuclear and Particle Physics at FNSPE CTU met at the annual winter workshop. The meeting was held during the week of 13.–19. 01. 2019 at *Penzion Krakonoš* in the Jizera Mountains in the Czech Republic. The main goal of the workshop is to follow the progress of students, discuss problems and experiences and also to get to know each other better. Each participant gave a talk about their work or progress during the previous year. Extended abstracts of these talks are published in the proceedings you are holding now.

Editors

Study of jet shapes in Monte-Carlo generator JEWEL at RHIC

Veronika Agafonova *(Veronika.Agafonova@fjfi.cvut.cz)*

1 Introduction

Nuclear-nuclear collisions at energies attainable at the large accelerators RHIC and LHC are an ideal environment to study nuclear matter under extreme conditions of high temperature and energy density. One of the most important probes of such nuclear matter is the study of jet production. Jets are collimated sprays of hadrons originating from fragmentation of a hard parton created in the initial stage of a nucleus-nucleus collision and can be used for tomography of the nuclear matter. In order to understand the mechanisms of energy loss of partons in the medium and the properties of the medium itself, one should measure the modifications of the jet yield and fragmentation relative to p+p collisions using different jet shape observables. For this analysis the following jet shapes were chosen.

The first observable is the angularity, g. It is defined as

$$g = \sum_{i \in jet} \frac{p_{\mathrm{T}}^{\mathrm{i}}}{p_{\mathrm{T,jet}}} |\Delta R_{\mathrm{i,jet}}|, \tag{1}$$

where $p_{\mathrm{T}}^{\mathrm{i}}$ represents the momentum of the ith constituent and $\Delta R_{\mathrm{i,jet}}$ is the distance in $\eta \times \phi$ plane between the constituent i and the jet axis (η stands for the pseudorapidity and ϕ is the azimuthal angle). This observable probes the radial distribution of radiation inside the jet [1].

Another observable, the momentum dispersion, $p_T D$, measures the second moment of the constituent p_{T} distribution in the jet and is connected to hardness or softness of the jet fragmentation [1]. The momentum diapersion can be calculated as

$$p_T D = \frac{\sqrt{\sum_{i \in jet} p_{\mathrm{T,i}}^2}}{\sum_{i \in jet} p_{\mathrm{T,i}}}. \tag{2}$$

The last observable, that was chosen for the analysis, is the $LeSub$ - the difference of the leading track p_{T} ($p_{\mathrm{T,track}}^{\mathrm{lead}}$) and sub-leading track p_{T} ($p_{\mathrm{T,track}}^{\mathrm{sublead}}$),

$$LeSub = p_{\mathrm{T,track}}^{\mathrm{lead}} - p_{\mathrm{T,track}}^{\mathrm{sublead}}. \tag{3}$$

This jet shape shows toughness against contributions of soft background particles [1].

In this analysis the anti-k_T algorithm and the chosen jet shape observables were applied on the simulated data with/without nuclear medium model at particle level in the Monte-Carlo generator JEWEL at the center of mass energy of 200 GeV per nucleon-nucleon pair. Below, some of the obtained results will be discussed as a function of the transverse momentum of jet and the centrality in vacuum and nuclear medium.

2 Simulation in JEWEL

For this analysis 50 million events were simulated for the interaction in vacuum and 20 million events for the interaction in medium. The simulation was made for 0–10% central and 60–80% peripheral "recoils on/off" collisions. Table 1 contains the parameters used for the vacuum model. Additional parameters for the simulation with the medium can be found in Table 2.

Name of parameter	Name in JEWEL	Value	
Parton Distribution Function set	PDFSET	10100	
Number of events	NEVENT	100000	
The CMS energy of the colliding system	SQRTS, [GeV]	200	
Minimum p_T in matrix element	PTMIN, [GeV]	3	
Maximum p_T in matrix element	PTMAX, [GeV]	-1	
The switch of keeping recoils	KEEPRECOLIS	T	F
The rapidity range	ETAMAX	2.5	

Table 1: Parameters of the JEWEL vacuum simulation for Au+Au central and peripheral "recoils on/off" collisions [2].

Name of parameter	Name in JEWEL	Value	
The initial (mean) temperature	TI, [GeV]	0.28	
The initial time τ_i	TAUI, [fm]	0.6	
An integer mass number of colliding nuclei	A	197	
The lower end of centrality range	CENTRMIN, [%]	0	60
The upper end of centrality range	CENTRMAX, [%]	10	80
The nucleus-nucleus cross-section	SIGMANN, [fm^2]	4.2	

Table 2: Parameters of the JEWEL simulation with medium for Au+Au central and peripheral "recoils on/off" collisions [2].

The resolution parameter R quantifies the size of the jet. For this analysis values of the resolution parameter were chosen to be $R = 0.2$ and $R = 0.4$, respectively. The charged particles were simulated in the pseudorapidity $\eta_{cent} = 2.5$ and full azimuth. All particles were required to have the center-of-mass energy of $\sqrt{s_{\mathrm{NN}}} = 200$ GeV. Jets were reconstructed with the anti-k_T algorithm [3] included in the FastJet software package [4].

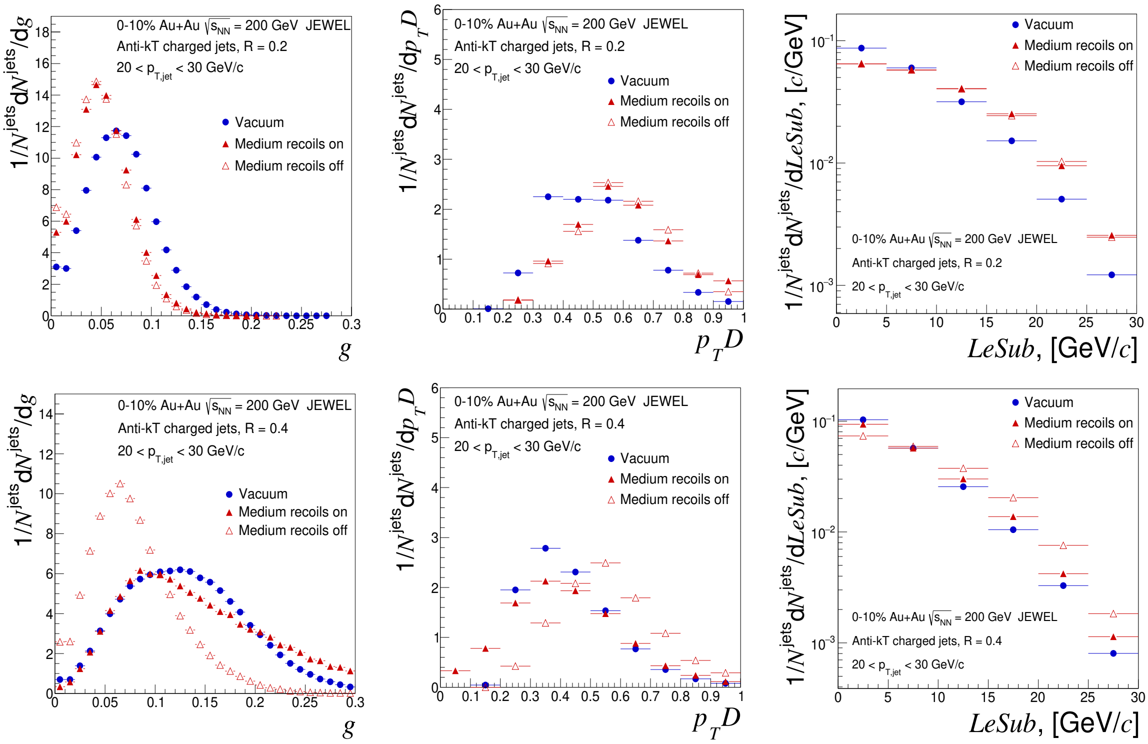

Figure 1: Jet shape distributions for central Au+Au collisions at $\sqrt{s_{\mathrm{NN}}} = 200$ GeV with $R = 0.2$ (top row) and $R = 0.4$ (bottom row) for $p_{\mathrm{T}} = 20 < p_T < 30$ GeV/c.

3 Results

In this section only the results for central Au+Au collisions with the resolution parameter $R = 0.2$ and $R = 0.4$ in the $20 < p_T <30$ GeV/c range will be shown (Figure 1).

All the distributions compare the vacuum and the medium "recoils on/off" model. A better agreement between the models can be observed for the $R = 0.2$ for all jet shapes (Figure 1 top) in comparison to the distributions with the resolution parameter $R = 0.4$ (Figure 1 bottom). It can be seen, that all jet shapes with the $R = 0.4$ have a coincidence only between the interactions in vacuum and interactions in medium with "recoils on" option. It is important to note that all the results were obtained without any background subtraction. For this reason, such a difference in the position of peaks can be observed.

One of the goals of future work is to perform the background subtraction, after which it is expected that the points for medium "recoils on/off" and vacuum models will be closer to each other.

References

[1] S. Acharya et al., *JHEP* 10:139 (2018)

[2] K. C. Zapp, *Eur. Phys. J.*, C74(2):2762 (2014)

[3] M. Cacciari, G. P. Salam, G. Soyez, *JHEP*, 04:063 (2008)

[4] M. Cacciari, G. P. Salam, G. Soyez, [arXiv: 1111.6097] (2012)

On the measurement problem in quantum mechanics

Elisabeth Andriantsarazo*(andrieli@fjfi.cvut.cz)*

There is a puzzling problem that has been keeping physicists wondering about nature of quantum systems since the invention of quantum mechanics. It is called the *measurement problem* and there are several questions that need to be answered, such as:

1. How and why does a wave function reduce?
2. What is the difference between subject and object in quantum mechanics?
3. Can one obtain additional information about a quantum state? In other words, is the description provided by quantum physics really incomplete, as Einstein, Podolsky and Rosen pointed out in their famous paper [3]?
4. Can this problem be solved by another approach?

The last question is the one we shall explore. We will be namely speaking about Bohmian mechanics, a.k.a. the Pilot wave theory created by de Broglie and later by David Bohm.

The quantum mechanical system is represented by a vector in complex linear vector space. Its observables are then represented by Hermitian operators in this space. Measurement of an observable yields an eigenvalue so one can understand the quantum formalism as a “measurement” formalism. But there the problem with reduction of the wave packet – there are no mechanical arguments for this process and no one really understands how or why does it happen.

What can this new approach, called the Pilot wave theory, offer? The first thing that changes is the fundamental understanding of reality. It is no longer considered non-existent until observation, but understood the same way we understand reality in classical physics. The authors introduced something called pilot wave, here denoted as $(\psi, \mathbf{x})$, where ψ is a field propagating in 3N dimensional space and $\mathbf{x}$ is just a particle configuration. Since ψ is a physical entity existing even when unobserved, there are no problems with the subject-object division. This pilot wave drives the particle towards large $|\psi|^2$, which can explain the strange particle-wave behavior we experience.

There is also the problem with non-locality that we see in entangled states, what does the Pilot wave theory offer to solve this problem? It gives us local ”beables” (instead of observables), that are assigned to bounded space-time region with hope to formulate some notion of local causality. Still it looks like due to quantized vacuum non-locality might be unavoidable. Another approach is to let the guiding wave propagate in multidimensional space but nothing really helps to reduce the apparent correlations between entangled states. Which leads us to the last paragraph of this work – there are apparent problems that Bohmian mechanics has.

First, the particle-wave dynamics can not reproduce quantum mechanics in general and it doesn't implement relativity, although there are attempts to create Bohmian version of quantum field theory. It also needs a better mathematical apparatus for the guiding equation, which is given by:

$$\frac{d\mathbf{Q}}{dt}(t) = \frac{\hbar}{m}\mathrm{Im}(\frac{\nabla\psi}{\psi})(\mathbf{Q}, t) \tag{1}$$

where $\mathbf{Q}$ denotes the particle position. The equation describes how particles "ride" the pilot wave. And, obviously, an abstract wave function extending through space is just as mysterious in this framework as it is in the Copenhagen interpretation. So the Bohmian mechanics can give us answers to some of those questions, but it doesn't really help our understanding of quantum world nor does it give better predictions.

References

[1] Anders, et al. Double-slit experiment with single wave-driven particles and its relation to quantum mechanics. Physical Review E, 2015, 92.1: 013006.

[2] John S.; BELL, John Stewart. Speakable and unspeakable in quantum mechanics: Collected papers on quantum philosophy. Cambridge university press, 2004.

[3] Einstein, A., Podolsky, B., Rosen, N. (1935). Can quantum-mechanical description of physical reality be considered complete?. Physical review, 47(10), 777.

Influence of the Galactic Magnetic Field on Arrival Directions of Cosmic Rays

Alena Bakalová *(alena.bakalova@fjfi.cvut.cz)*

Abstract

We present first results of a study of arrival directions of cosmic rays from numerical simulations of cosmic-ray propagation in the Jansson Farrar model of the Galactic magnetic field using regular and turbulent components of the field. Distributions of arrival directions of particles with rigidities from 10^{19} V up to 10^{20} V are studied for two nearby sources - Centaurus A and Messier 82. We demonstrate that the Galactic magnetic field has a significant influence on arrival directions of cosmic rays even at the highest energies and that arrival directions from candidate source should not be approximated by circular regions around it.

1 Introduction

The global understanding of important features of the most energetic cosmic rays grew significantly with the arrival of large area observatories such as the Pierre Auger Observatory [1] or Telescope Array [2]. Recent results of the Pierre Auger Observatory indicate that cosmic rays with energies above 8 EeV are of extragalactic origin [3], however, the sources of ultra-high energy cosmic rays (above 10^{18} eV) remain unknown as well as the principles of cosmic ray acceleration.

The task of connecting particles to their sources according to their arrival directions is made more difficult due to deflections caused by the Galactic magnetic field (GMF). In our research we investigate the influence of the GMF on arrival directions of cosmic rays by studying distributions of arrival directions from single sources, we especially focus on particles with rigidity above 10^{19} V.

2 Simulated data

A library of simulations of cosmic rays propagated in the GMF using CRPropa 3 [4] was created. We simulate particles of different rigidities from $\log(R/\mathrm{V}) = 19.0$ V up to a rigidity $\log(R/\mathrm{V}) = 20$ V with a step of 0.1. Particles are propagated in the Jansson Farrar 2012 model of the GMF [5] using both regular and turbulent component of the

GMF. The turbulent magnetic field is defined as a kolmogorov random field with coherence length $L_{\mathrm{coh}} = 60$ pc. We simulate $2 \cdot 10^7$ particles of each rigidity emitted isotropically from Earth placed at position (-8.5,0,0) kpc and propagated to the edge of our Galaxy which is defined as a sphere with a radius $R = 20$ kpc.

3 Results

In order to find particles originating from a given source we look in our all sky simulations for particles hitting the Galaxy border with angular distance from the chosen source smaller than 1°. Such solid angle area is needed not only for sufficient statistics, but also to account for the effects of deflections in extragalactic magnetic field as well as for finite sizes of astrophysical objects instead of point-like sources.

We show the results for two sources, a radio galaxy Centaurus A and a starburst galaxy Messier 82. Sky plots of arrival directions of particles originating from CenA and M82 with rigidities from $\log(R/\mathrm{V}) = 19.0$ up to $\log(R/\mathrm{V}) = 20.0$ are shown in Figure 1 and Figure 2, respectively.

For the highest rigidities all simulated particles arrive in directions close to the position of the source, however, for lower rigidities, corresponding to lower energy or higher proton number, the events are distributed farther from the source and the spread of events increases as well. We define a centroid of events for given rigidity as an event with the smallest sum of angular distances to all events with the same rigidity. The angular distance between centroid and source increases with decreasing rigidity as expected, nevertheless, the absolute number depends on the position of the source. In the case of Centaurus A, the angular distance is less than 20° for $\log(R/\mathrm{V}) = 19.0$ while for M82 it is almost 30° for the same rigidity. On the other hand, the spread of events is larger for Centaurus A than for M82 for all rigidities. This is probably caused by the location of M82, which is far from the galactic plane, therefore the particles do not travel through the strongest and most turbulent parts of the GMF as in the case of Centaurus A.

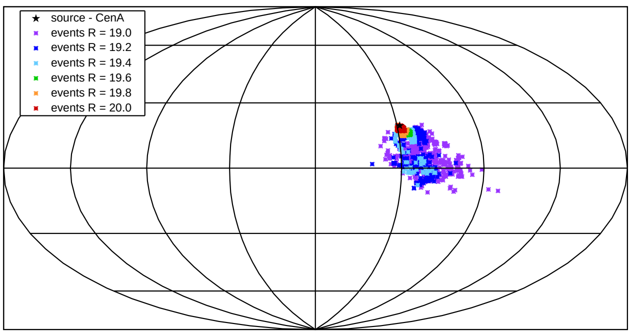

Figure 1: Arrival directions of cosmic rays originating from Centaurus A. The sky plot is in galactic coordinates.

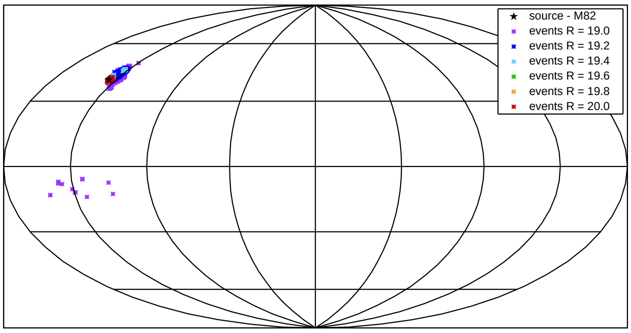

Figure 2: Arrival directions of cosmic rays originating from Messier 82. The sky plot is in galactic coordinates.

4 Conclusions

We performed all sky simulations of cosmic rays with rigidities above 10^{19} V propagated in the JF12 model of the GMF using both regular and turbulent component of the magnetic field in order to study the arrival directions of particles from single sources. We show that cosmic rays are influenced by the GMF even at the highest energies and their deflections from the sources might be as large as tens of degrees.

In the case of iron primary with energy 10^{20} eV the corresponding rigidity is less then $4 \cdot 10^{18}$ V. For such low rigidities the information about the source is completely lost and the arrival directions of such particles originating in single source cover extensive part of the whole sky. Therefore, to find sources of ultra-high energy cosmic rays (UHECR), proton or light nuclei are needed.

For rigidities above 10 EV, the observed UHECR images strongly depend on the source position and particle rigidity. For both studied sources, the images are not well represented by circular areas around given source as the images tend to be of various shapes and a shift of the centroid position from the position of the source is observed.

References

[1] The Pierre Auger Collaboration, The Pierre Auger Cosmic Ray Observatory, Nuclear Instruments and Methods in Physics Research, 798:172-213 (2015)

[2] H. Kawai et al., Telescope Array Experiment, Nuclear Physics B Proceedings Supplements, 175:221-226 (2008)

[3] Pierre Auger Collaboration, Science 357, 1266 (2017)

[4] Alves Batista, R., Dundovic, A., Erdmann, M., et al., Journal of Cosmology and Astroparticle Physics 5, 038 (2016)

[5] Jansson, R., & Farrar, G. R., The Astrophysical Journal 757, 14 (2012)

Production of vector mesons within the energy-dependent hot-spot model

Dagmar Bendová *(Dagmar.Bendova@fjfi.cvut.cz)*

This text is a summary of the talk given at Workshop of Experimental Nuclear and Particle Physics 2019 of FNSPE CTU at 18th January in Bílý Potok.

Within perturbative quantum chromodynamics (pQCD), the partonic structure of hadrons evolves with increasing energy (or equivalently with decreasing Bjorken-x). Measurements of the proton structure at HERA indicate that the gluon density grows linearly with decreasing x [1]. However, this behaviour becomes nonlinear at the point where the proton structure enters a so-called saturated regime [2].

Exclusive vector meson production has been proven to be a very good tool to study the evolution of gluon densities inside the proton. This process has been investigated at HERA and at the LHC and the measurements have been successfully described by various models which include saturation effects. A similar process, in which the interacting proton dissociates into a hadronic system, can be related to fluctuations of the partonic structure of the proton within the energy-dependent hot-spot model approach, as has been investigated in [3]. This model successfully describes all available data on the energy dependence of both exclusive and dissociative ρ, J/ψ and $\Upsilon(1S)$ photoproduction [4] and electroproduction [5] off protons and also exclusive J/ψ photoproduction off nuclear targets [6]. Furthermore, it predicts the steep rise of the dissociative photoproduction cross section with energy up to a maximum value and its subsequent decrease. The positions of these maxima show a linear dependence on scale of the interaction, given by the sum of the squares of the photon virtuality and the mass of the vector meson. It has been shown that this phenomenom can possibly be measured at current (LHC) and planned (EIC) accelarators [5].

The vector meson production process proceeds as follows: The incoming electron radiates a virtual photon which then interacts with the target proton with subsequent production of a vector meson. The photon can be quasi-real (photoproduction) or it can have a large virtuality Q^2 (electroproduction). The interaction is coherent in the exclusive case and incoherent in the dissociative process, in which the target proton is broken into a hadronic system Y.

Production of vector mesons can be well-described within the color dipole picture [7, 8]. In this framework the virtual photon can fluctuate into a $q\bar{q}$ dipole. The dipole interacts with the proton via gluon exchange and after the interaction a vector meson is formed from the dipole. This production of a vector meson with mass M in the final state is given by the scattering amplitude

$$\mathcal{A}_{T,L}(x,Q^2,\vec{\Delta}) = i\int \mathrm{d}\vec{r}\int_0^1 \frac{\mathrm{d}z}{4\pi}\int \mathrm{d}\vec{b}|\Psi^*_{VM}\Psi_{\gamma^*}|_{T,L}\exp\left[-i\left(\vec{b}-(1-z)\vec{r}\right)\vec{\Delta}\right]\frac{\mathrm{d}\sigma_{q\bar{q}}}{\mathrm{d}\vec{b}}, \quad (1)$$

where subscripts T, L denote contribution from the transversally, resp. longitudinally, polarized virtual photon. Ψ_{VM}, Ψ_{γ^*} are the wave functions of the vector meson and virtual photon, respectively, $\vec{r}$ is the transverse size of the color dipole, z is the fraction of the photon's longitudinal momentum carried by the quark, $\vec{b}$ is the impact parameter in the transverse plane, $\vec{\Delta}^2 = -t$ is the squared four-momentum transferred at the proton vertex, Q^2 is the virtuality of the exchanged photon and x denotes the Bjorken-x of the exchanged pomeron.

The key part of the photon-proton scattering amplitude (1) is the cross section of the interaction of the color dipole with the proton target. It is related, via the optical theorem, to the imaginary part of the dipole-proton amplitude $N(x,\vec{r},\vec{b})$:

$$\frac{\mathrm{d}\sigma_{q\bar{q}}}{\mathrm{d}\vec{b}} = 2N(x,\vec{r},\vec{b}). \quad (2)$$

In order to study the effects of fluctuations of the proton structure in the transverse plane a factorized form of the dipole amplitude can be used. This approach results in the following form of the dipole cross section:

$$\frac{\mathrm{d}\sigma_{q\bar{q}}}{\mathrm{d}\vec{b}} = \sigma_0 N(x,\vec{r})T_p(\vec{b}), \quad (3)$$

where $T_p(\vec{b})$ decribes the proton profile in the impact-parameter plane and σ_0 is the normalization parameter given as $\sigma_0 = 4\pi B$, with B being fixed according to data [3]. This approach has already been successfully used in [3, 4, 6].

The dipole amplitude $N(x,\vec{r})$ can be obtained from various parametrizations (for an overview see Ref. [10]) or as the solution of the Balitsky-Kovchegov evolution equation [11, 12].

Since the proton is a quantum object, its structure changes from interaction to interaction. To incorporate these changes, the so-called hot-spot model is applied, which describes the photo- and electroproduction of vector mesons off protons and nuclei [3, 4, 5, 6]. The fluctuations are included in the proton profile function $T_p(\vec{b})$ in this model. Some examples of proton profiles within the hot-spot model can be seen in Fig. 1 for various values of x. The proton profile is defined as a sum of N_{hs} regions of high gluonic density (hot spots) with different configurations in each event

$$T_p(\vec{b}) = \frac{1}{N_{hs}}\sum_{i=1}^{N_{hs}} T_{hs}\left(\vec{b}-\vec{b}_i\right). \quad (4)$$

The hot spot is defined by a Gaussian distribution

$$T_{hs}(\vec{b}-\vec{b}_i) = \frac{1}{2\pi B_{hs}}\exp\left(-\frac{(\vec{b}-\vec{b}_i)^2}{2B_{hs}}\right), \quad (5)$$

with width B_{hs}. The vectors $\vec{b_i}$ define the positions of hot spots inside the proton. They are obtained randomly from a 2D Gaussian distribution with width B and centered at (0,0).

The indirect energy-dependence on the number of hot spots is given by

$$N_{hs} = p_0 x^{p_1} \left(1 + p_2 \sqrt{x}\right), \tag{6}$$

where p_0, p_1 and p_2 are free parameters. Note that the relation 6 represents the mean value of a zero-truncated Poisson distribution from which an integer value of N_{hs} is obtained. This approach ensures the growth of N_{hs} with decreasing Bjorken-x.

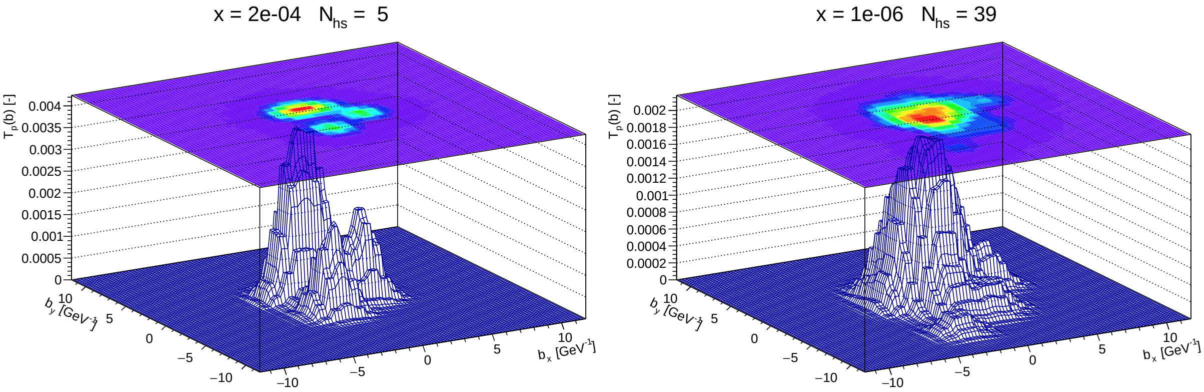

Figure 1: Examples of proton profiles within the hot-spot model for $x = 2 \cdot 10^{-4}$ and $x = 10^{-6}$.

References

[1] H. Abramowicz et al., Eur.Phys.J. C75 (2015) no.12, 580.

[2] F. Gelis, E. Iancu, J. Jalilian-Marian, and R. Venugopalan, Ann. Rev. Nucl.Part.Sci. (2010) no.60, 463–489.

[3] J. Cepila, J. G. Contreras, and J. D. Tapia Takaki, Phys.Lett. B766 (2017), 186–191.

[4] J. Cepila, J. G. Contreras, M. Krelina, and J. D. Tapia Takaki, Nucl.Phys. B934 (2018), 330-340.

[5] D. Bendova, J. Cepila, and J. G. Contreras, arXiv:1811.06479v2.

[6] J. Cepila, J. G. Contreras, and M. Krelina, Phys.Rev. C97 (2018) no.2, 024901.

[7] A. H. Mueller, Nucl.Phys. B415 (1994), 373-385.

[8] A. H. Mueller, and B. Patel, Nucl.Phys. B452 (1994), 471-488.

[9] A. G. Shuvaev, K. J. Golec-Biernat, A. D. Martin, and M. G. Ryskin, Phys.Rev. D60 (1999), 014015.

[10] H. Kowalski, L. Motyka, and G. Watt, Phys.Rev. D74 (2006), 074016.

[11] I. Balitsky, Nucl.Phys. B463 (1996), 99-160.

[12] Y. V. Kovchegov, Phys.Rev. D60 (1999), 034008.

Jets and algorithms for their reconstruction

Josef Bobek *(josef.bobek@post.cz)*

1 Jets

First of all, what is a jet by the definition? Jet can be defined as a collimated spray of stable particles. In the collision, the pair of partons with a very large transverse momentum is created. Those two partons will create the jets and thanks to the conservation laws they will have opposite coordinates in the detector. This phenomenon can be used to prove the existence of quark-gluon plasma. Let us focus on one of the partons. Thanks to the strongly interacting medium it will radiate a gluon. Owing to the kinematics the angle between the trajectory of created gluon and original parton is significantly small. Gluon will either decay on $q\overline{q}$ pair or radiate another gluon. Still considering color confinement of the $a\overline{q}$ pair. Thus, if quarks in pair will get apart more than about 1fm, they will create another $q\overline{q}$ pair. This will continue for a while and when all of our particles will leave the medium they will go into the hadronization phase. In this phase, stable and colorless particles (hadrons) are created and then observed with detectors. Detected stable particles in the shape of a collimated cluster are called jet. This jet carries information about original parton like momentum, energy, spin, etc.

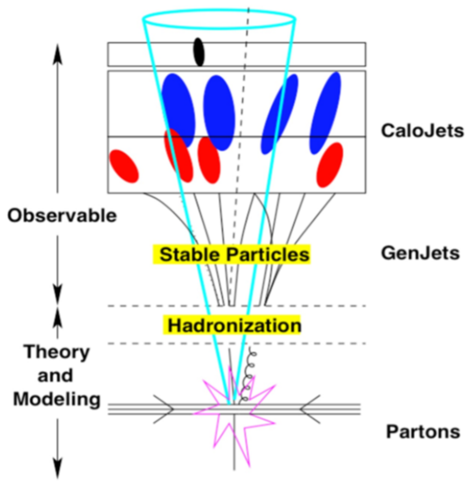

Figure 1: Creation of the jet. [3]

2 Reconstruction algorithms

We have got two important aspects of jet reconstruction algorithms. Those are Jet radius R and IRC safety (infra-red and collinear). In the algorithms, radius R is a imput variable. Alorithms that are not IRC safe causes wrong results in QCD calculations.
There are two types of algorithms and those are Cone and Sequential Clustering algorithms. Cone, like IC-PR, ICSM and SIScone, were liked a lot thanks to the easy implementation. Nowadays only SIScone is useable for data analysis thanks to its IRC safety. k_t, anti-k_t and Cambridge/Aachen (C-A) are sequential clustering algorithms. All of them are very useful and they are used for data analysis most. Since we have fast jet, sequential clustering algorithms are also easy for implementation and also fast.

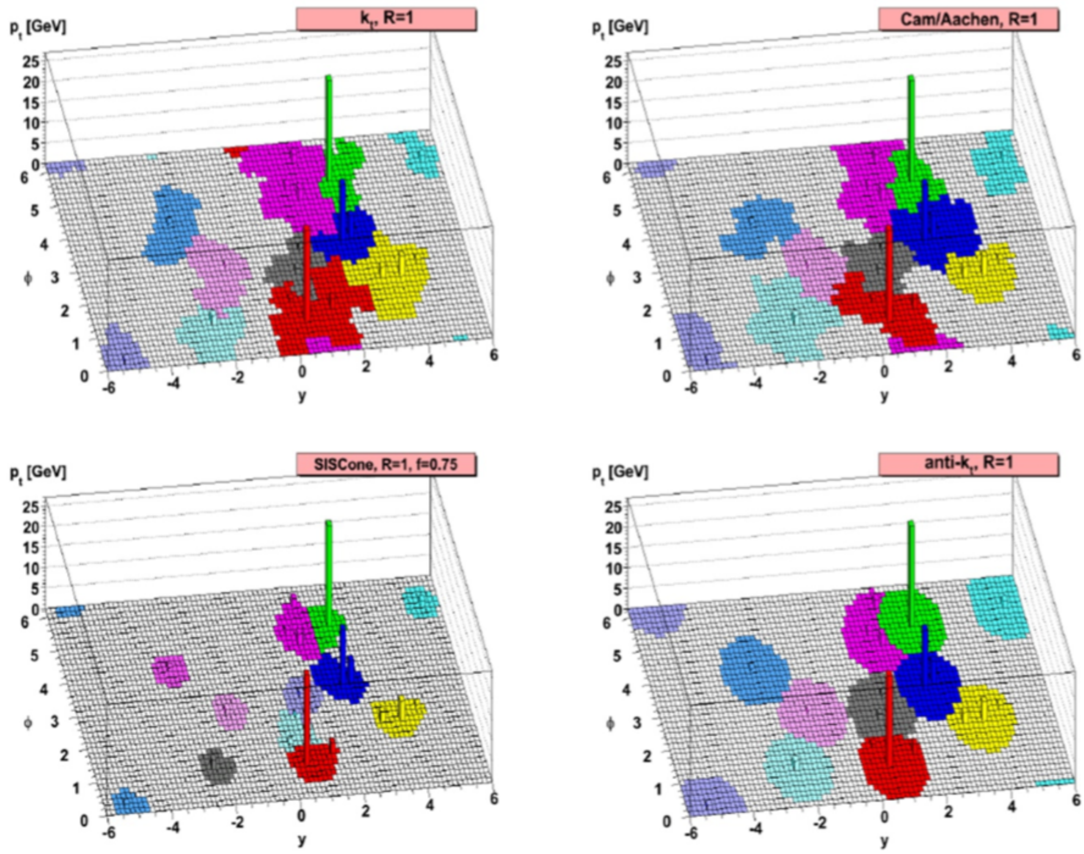

Figure 2: Difference between main jet reconstruction algorithms. [3]

References

[1] M. Cacciari, G. P. Salam, G. Soyez: FastJet user manual, CERN-PH-TH/2011-297

[2] M. Connors, C. Nattrass, R. Reed, and S. Salur, Jet measurements in heavy ion physics, Rev. Mod. Phys. 90, 025005.

[3] Ryan Atkin, Review of jet reconstruction algorithms, J. Phys.: Conf. Ser. 645 012008

Heavy flavor physics in heavy-ion collisions

Jakub Češka*(ceskajak@fjfi.cvut.cz)*

1 Introduction

The main aim of my bachelor thesis is to analyze a state of matter in quantum chromodynamics (QCD) known as quark-gluon plasma (QGP). It occurs under extreme conditions and is a state of matter found at the beginning of the universe. Its study is a way to analyze the fundamental properties of matter, as well as the situation between 10^{-12} and 10^{-6} seconds after the Big Bang.

2 The quark-gluon plasma

The QGP is a state of matter in QCD, occurring at extremely high temperatures and/or densities. It is composed of quasi-free quarks and gluons, which are usually bound in color-neutral hadrons. Color, also known as color charge, is a property of quarks and gluons related to strong nuclear force. Quarks can have one of three colors (red, green or blue) and gluons are found in one of eight states of color-anticolor.

In Earth conditions, the QGP can be made in laboratories during nucleus-nucleus ultrarelativistic collisions (such as the RHIC at the BNL or the LHC at the CERN). It is impossible to observe the QGP directly, due to its short life (around 10^{-22} s). Therefore other methods have to be applied in order to study its properties. Such probes can be divided into different categories depending on momentum transfer Q: soft (flow, fluctuations), electromagnetic (photons, dileptons) and hard (jet quenching, quarkonia suppression).

3 Quarkonia

Quarkonia are bound states of a quark and a corresponding antiquarks ($c\bar{c}$ or $b\bar{b}$). This meson has zero charm or beauty, which is a phenomenon called 'hidden' charm or beauty. Quarkonia composed of the c quark, the so called charmonia, can be found in different states; J/Ψ (ground state), χ_c or Ψ' (excited states). Similarly, beautiful quarkonia, bottomonia, create multiple states, such as Υ, χ_b, Υ' or χ'_b.

An important property of quarkonia is the fact that they do not decay strongly via strong interaction into their corresponding 'open' mesons ($D^0 = c\bar{u}$ and $B^+ = u\bar{b}$. Other

state	J/Ψ	χ_c	Ψ'	Υ	χ_b	Υ'	χ'_b
mass (GeV)	3.10	3.53	3.68	9.46	9.99	10.02	10.36
ΔE (GeV)	0.64	0.20	0.05	1.10	0.67	0.54	0.31
radius (fm)	0.25	0.36	0.45	0.14	0.22	0.28	0.34

Table 1: Overview of masses, binding energies and radii of the lowest $c\bar{c}$ and $b\bar{b}$ states.

strong decays are also strongly suppressed due to the OZI rule. These decays are impossible due to the mass of the quarkonia is lower, than the mass of two corresponding mesons , as illustrated in equations (1) and (2).

$$m_{J/\Psi} \doteq 3.1 \text{ GeV/c}^2 < 2m_{D^0} \doteq 3.74 \text{ GeV/c}^2 \tag{1}$$

$$m_{\Upsilon} \doteq 9.46 \text{ GeV/c}^2 < 2m_{B^+} \doteq 10.56 \text{ GeV/c}^2 \tag{2}$$

4 Charmonium production in hadron collisions

The production of charmonia in hadron-hadron collisions consists of three phases. The first phase is the creation of the $c\bar{c}$ pair itself. Due to the large mass of c ($m_c \sim 1.3$ GeV) can be considered a hard process. It is dominated by gluon fusion ($gg \to c\bar{c}$) for high energies (illustrated in figure 1. This newly created pair is in a color octet state and has to get rid of its color charge, in order to leave the interaction zone as a physical resonance. The second phase therefore consists of color neutralization of the pair by interacting with the surrounding color field. The last, third, phase is the actual physical resonance.

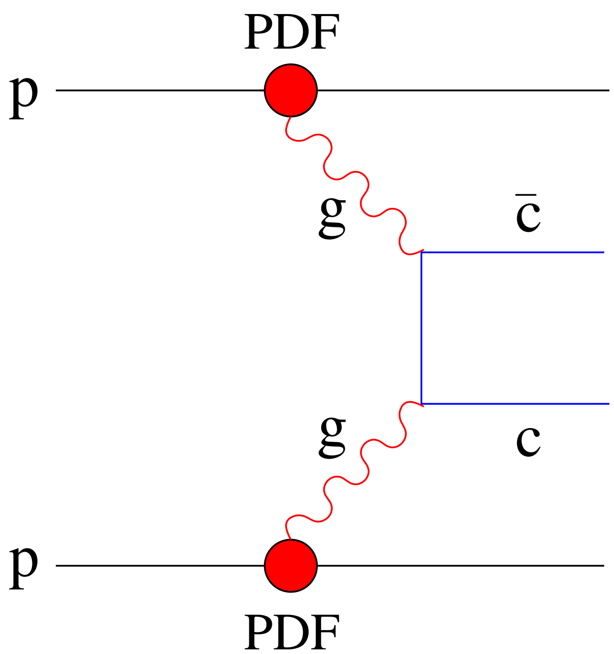

Figure 1: Lowest order Feynman diagram of $c\bar{c}$ production via gluon fusion.

In nucleus-nucleus collisions other processes come into play during the charmonium creation. These effects are called nuclear. For example the presence of other nuclei in the nucleus can lead to decrease (shadowing) or increase (antishadowing) of the production rate. The newly created *cqbarc* pair also has to pass through the nuclear medium, in which the pre-resonance or resonance state can be absorbed by interactiong with other particles.

5 Charmonium suppression

The measurement of quarkonia created in heavy-ion collisions can be used as a means to identify the temperature of the newly created QGP. By comparing the yield of different charmonia it is possible to identify the temperature interval, in which the matters lies. This is possible due to different states having different temperature, at which they dissociate, because the mass of the state is proportional to the radius, thus heavier quarkonia, having a larger radius, dissociate at lower temperatures. In the case of charmonia, the Ψ' state dissociates under the lowest temperature, followed by the χ_c state. The J/Ψ state breaks at the largest temperatures.

The charmonium production suppression in nucleus-nucleus collisions occurs particularly for the mid-rapidity region. The suppression can be quantified by the nuclear modification factor (3).

$$R_{\mathrm{AA}}(p_T) = \frac{\mathrm{d}N^{\mathrm{AA}}/\mathrm{d}p_T}{\langle N_{\mathrm{coll}}\rangle \mathrm{d}N^{\mathrm{pp}}/\mathrm{d}p_T} \tag{3}$$

6 Further work

Following the theoretical research of underlying principles, the next steps in the bachelor thesis are simulation and subsequent analysis of heavy-ion production data. Charmonia are an are of particular interest, as they can be used to measure the properties of the QGP.

7 Conclusion

The QGP is an extreme state of matter, in which the properties of strong force can be studied. Quarkonia are a very potent probe into the properties of the QGP, as they can withstand the extreme conditions of matter present in QGP. The ultimate goal of my thesis is to simulate and analyze heavy flavor production, in order to gain an outlook on heavy flavor physics and to familiarize myself with simulation and data analysis methods used in the field.

References

[1] S. Sarkar et al. *The physics of the Quark-Gluon plasma: introductory lectures.* New York: Springer, c2010. Lecture notes in physics, 785. ISBN 978-364-2022-852

Electron beam isochroneous, achromatic focusing system

Pavel Gajdoš*(gajdopa1@fjfi.cvut.cz)*

1 Introduction

The laser wakefield acceleration produces ultra-short electron bunches. The length is typically in the order of femtoseconds. Nevertheless, these bunches has a large energy spread (10 - 20 %) [1], which means that after propagation in free space the electron beam is stretched. Thus, in order to obtain the initial beam length for applications (eg. further acceleration), the isochronous, achromatic focusing system is needed.

2 Quadrupole magnets and FODO lattice

In conventional accelerators the beam is focused using quadrupole magnets in form of so-called FODO lattice. Quadrupole magnets focusing in one axis and defocusing in the other. Considering the beam propagation in z-axis and entering the quadrupole at z_0, the transformation matrix is

$$\begin{pmatrix} u(z) \\ u'(z) \end{pmatrix} = \begin{pmatrix} \cos\psi & \frac{1}{\sqrt{k}}\sin\psi \\ -\sqrt{k}\sin\psi & \cos\psi \end{pmatrix} \begin{pmatrix} u(z_0) \\ u'(z_0) \end{pmatrix}$$

for quadrupole in focusing plane, where $u(z)$ can be taken as x or y axis in position z. For defocusing quadrupole the tranformation matrix is given by

$$\begin{pmatrix} u(z) \\ u'(z) \end{pmatrix} = \begin{pmatrix} \cosh\psi & \frac{1}{\sqrt{|k|}}\sinh\psi \\ \sqrt{\mid k \mid}\sinh\psi & \cosh\psi \end{pmatrix} \begin{pmatrix} u(z_0) \\ u'(z_0) \end{pmatrix}.$$

The phase is $\psi = \sqrt{\mid k \mid}\,(z - z_0)$ and expression for k is

$$k\left(\mathrm{m}^{-2}\right) = 0.2998\frac{g\,(\mathrm{T/m})}{\beta E\,(\mathrm{GeV})},$$

where g is a magnetic field gradient and E energy of a particle.

The FODO lattice consists of three quadrupoles: focusing, defocusing and focusing in one plane and vice versa in the other plane. The condition for focusation is $2f_1 = 2f_3 = f_2$, whre f_1, f_2 and f_3 are focal lengths of first, second and third quadrupoles, respectively [2].

3 Chromaticity Correction

The simple FODO lattice works only when monochromatic beam is used. For realistic beams the chromaticity corrections have to be provided [3]. This can be done using sextupole magnets. These magnets have different magnetic profiles which allows focusing in one half-plane and defocusing in the other. The chromaticity correction using sextupole magnet is shown in Figure 1. The sextupole focuses particles above the beam axis which have higher energy and defocuses particles under the beam axis with lower energy. By finding the right magnetic field strength of the sextupole magnet, all particles could be focused in the one focal spot.

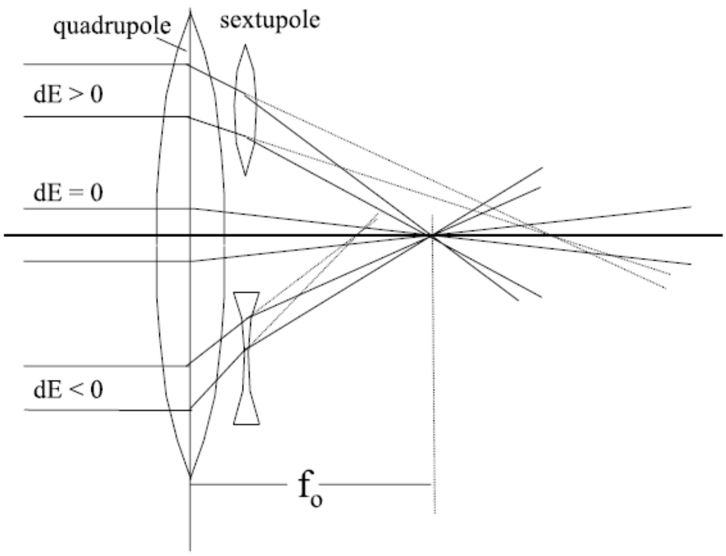

Figure 1: Achromatic correction using sextupole magnet [2].

Using a thin lense approximation (ie. $z - z_0 = l \rightarrow 0$) the magnetic field gradient of sextupole was determined for focusation of electron beam with energies from 60 to 110 MeV. The diameter of the beam was $d = 10$ cm. The focusing system consisted of focusing quadrupole, defocusing quadrupole and sextupole. The magnetic gradient of the first focusing quadrupole was set to $g_1 = 50$ T/m and the gradient of the second defocusing quadrpole was $g_2 = 55$ T/m. The magnetic gradient of sextupole for each energy line is in Table 1, where plus sign of g_3 means sextupole in focusing plane and vice versa.

4 The Focusing System Design

As could be seen in Figure 1 the beam has to be firstly separated by electron energies (spatial energy chirp). Similarly to magnetic chicane, which consists of four dipole magnets and it is used for beam compression, we will use two dipole magnets for the electron beam energy chirp, collimation and optimization of trajectories. The final scheme of electron beam focusing system is shown in Figure 2.

E [MeV]	g_3 [T/m]
110	14.8
105	13.0
100	11.0
95	9.2
90	7.4
85	0
80	-0.2
75	-2.2
70	-6.6
65	-11.6
60	-18.2

Table 1: The magnetic field gradient of sextupole for each energy line (plus sign of g_3 means sextupole in focusing plane and vice versa).

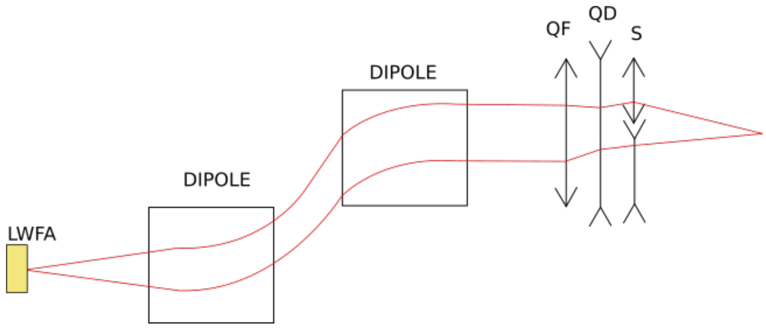

Figure 2: Scheme of focusing system. The electron is spatially chirped using two dipole magnets and focused via focusing quadrupole **QF**, defocusing quadupole **QD** and sextupole **S**.

5 Conclusions

A brief overview of beam focusing with quadrupole magnets and chromaticity correction using sextupole magnets was shown. The scheme of electron beam achromatic, isochronous focusing system was demonstrated in Figure 2. The magnetic field gradient of sextupole magnet was determined for electron beam with energy range 60 - 110 MeV.

References

[1] E. Esarey, C.B. Schroeder, and W. P. Leemans: Physics of laser-driven plasma-based electron accelerators, Rev. Mod. Phys. **81** (2009) 1229

[2] H. Wiedemann: Particle accelerator physics, Springer, 2007, ISBN 3 540 49043 2

[3] N. Toge, et al.: Chromaticity corrections in the SLC final focus system, PAC **4** (1991) 2067

Photon-induced processes in pp collisions in the ATLAS experiment

David Gančarčík*(gancadav@fjfi.cvut.cz)*

Two photon interaction is very rare process predicted by Quantum ElectroDynamics (QED). Cross section for this non-linear interaction could be derived from Heisenberg-Euler Lagrangian. It is very important field of study, because it can help us to understand light-by-light scattering. Also it can show us direction to theories beyond standard model such as axion-like particles, supersymmetry or warped extra dimensions. We focus on the central exclusive production of lepton pair which is pure QED process where the fiducial cross section can be precisely calculated. In our case, interacting protons have to remain intact, while other the possibilities where one or both protons dissociate are considered as background. Significant background is also caused by so-called Drell-Yan process, where quark from the first proton interact with antiquark from the second proton creating Z boson or virtual γ, which then decay into di-lepton pair. We suppress Drell-Yan background by cutting off Z boson mass region. In the presented review we report only the di-muon case.

There are two main setups to measure it on ATLAS. First, one require no charged particle track 1 mm far from di-muon vertex. To put down dissociation processes only events where transverse momentum of di-muon pair is less than 1,5 GeV. It is important to say that $\mu^+\mu^-$ pair is acoplanar. How distribution of acoplanarity looks after signal selection requirements can be seen in Figure 1

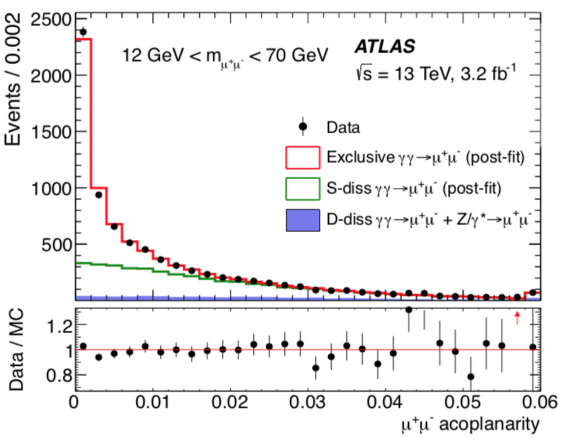

Figure 1: Distribution of acoplanarity after signal cuts [1]

Second, there is also slightly different way how to do it. Since 2017 ATLAS Forward Proton detectors (AFP) have been in operation. This detectors are placed approximately

200 m from interaction point and are capable to measure the outgoing protons, which lose part of their momenta and are bend out of beam envelope. AFPs are composed of silicon detector and time-of-flight detector. Kinematics of these protons is afterwords compared with the di-muon kinematics. This is a brilliant example of an exclusive measurement. Unfortunately there are several problems, which need to be explored. So far, only few events were found in the AFP measurement and only with one proton per collision..

References

[1] ATLAS collaboration, Phys. Lett. B777, Pages 303-323, *Measurement of the exclusive $\gamma\gamma \rightarrow \mu^+\mu^-$ process in proton–proton collisions at $s = \sqrt{13}$ TeV with the ATLAS detector*, `https://www.sciencedirect.com/science/article/pii/S0370269317309887`(2018)

Laser-Plasma Acceleration

David Grund *(grundda1@fjfi.cvut.cz)*

Originally proposed in 1979, the laser-plasma acceleration (LPA) is a promising way to accelerate electrons. The plasma waves, generated by high intensity laser pulses, can support large electric fields (up to the order of 100 GV/m). Nowadays, the concept benefits mainly from the CPA technique which allows to produce sufficiently short ($\lesssim 1$ ps) and intense laser pulses. To reach relativistic electron motion, the laser intensities $\gtrsim 10^{18}$ W/cm^2 at 1 μm wavelength are required.

Firstly, the laser pulse is shot into a gas cell or a gas jet. Then plasma is formed because the intensity of a pulse overcomes the value of so called atomic intensity (of the order 10^{16} W/cm^2). Reaching this intensity, the ionization of any target gas is guaranteed. The atoms of gas are ionized primarily via the multiphoton ionization as well as the tunnelling ionization. The latter starts to play an important role when the intensity of a laser pulse is above 10^{14} W/cm^2. At this time, the Couloumb barrier of the atom is suppressed by the laser field and there is a finite probability for electron to tunnel through and escape.

When considering a single laser pulse, one needs its length L to be comparable with plasma wavelength, i.e. $L \sim \lambda_p$. As the pulse propagates through the plasma, the surrounding electrons are expelled from high-intensity regions due to ponderomotive force. In this case, ions can be considered as stationary thanks to their large inertia in comparison to electrons. Therefore, perturbations in electron density occur, electrons are later attracted back to low-density areas and a wakefield is created behind the propagating pulse. Electrons can be then accelerated in the longitudinal electric field of this wake.

Another way to achieve a plasma wave is a plasma beat wave acceleration concept. It uses two laser pulses with wavelengths ω_1 and ω_2 so that $\omega_1 - \omega_2$ is approximately equal to plasma frequency ω_p. It had been used mainly prior to late 1980' (when the CPA started to be applied) because it does not require such ultrashort pulses as the case of a single pulse. However, the most efficient way of generating a wakefield effect is an optimized pulse train, where the time delay between each of pulses is chosen so that the next one maximizes the increase in wake electric field.

Core part of the LPA is the injection of electrons into the accelerating phase of the wakefield (where it is attracted by the positive charge in the direction of laser pulse propagation). When suitable conditions (pulse length $\leq \lambda_p/2$ and relativistic intensity of pulse) are satisfied, the so called blow-out or bubble regime can be reached. It can be described by a complete expulsion of the plasma electrons from some region, leaving an ion cavity, which is surrounded by an electron sheath. Self-injection (or self-trapping) occurs when electrons from the sheath fall into the acceleration phase and are subsequently trapped and accelerated. It is the most simple mechanism, yet it can be hard to control its progress.

Some other developed techniques of injection can be summarized as follows: the ionization injection, which uses a mixture of gases with different atomic numbers Z (the inner shell electrons can be trapped); the down-ramp in plasma density, which leads to decrease in phase velocity of a plasma wave and subsequent injection of electrons; the optical injection, which uses another laser pulse that supplies the main pump pulse with electrons. Pulses are usually crossed orthogonally or can be collinear. If so, the preceding pulse causes injection.

References

[1] E. Esarey, C. B. Schroeder, W. P. Leemans: Rev. Mod. Phys. 81 (2009)1229

[2] Gibbon, Paul. *Short Pulse Laser Interactions with Matter: An Introduction.* London: Imperial College Press, 2005.

[3] G. Bonnaud, D. Teychenné, J.-L. Bobin: Phys. Rev. E 50 (1994) R36

[4] V. Horný et al.: Plas. Phys, Contr. Fusion 60 (2018) 064009

Photoproduction of muon pairs in Pb-Pb collisions with ALICE

Tomáš Herman *(tomas.herman@cern.ch)*

The effects associated with the behaviour of the gluon distribution of hadrons at small Bjorken x, e.g. gluon saturation and gluon shadowing are not completely understood. They can be studied experimentally by measuring cross sections of processes sensitive to this parton distribution.

One of these processes is the exclusive photoproduction of a J/Ψ vector meson, which can be studied in ultra-peripheral collisions (UPC) where the colliding particles have an impact parameter larger than the sum of their radii. A diagram of such a process can be seen in Fig. 1.

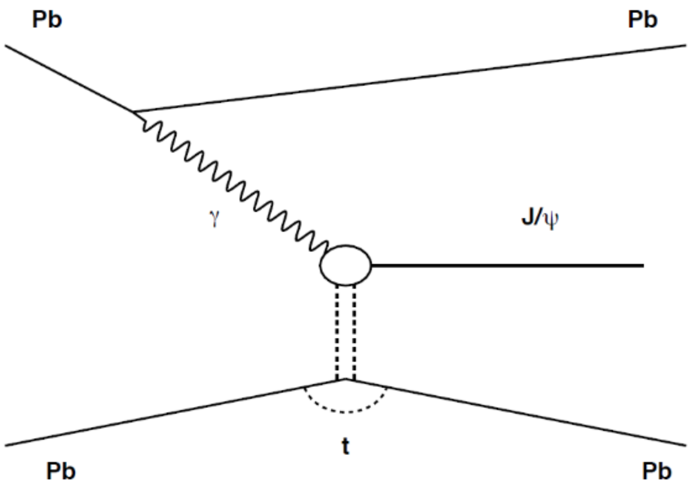

Figure 1: Diagram of coherent J/Ψ photoproduction in Pb-Pb UPC.

UPC of lead ions at the LHC provide an intense flux of photons with energies such that they are capable of probing the gluon distribution in lead nuclei at very low Bjorken x. The ALICE detector is then able to measure these collisions with high efficiency. Central production of J/Ψ is measured with the ITS, TPC, TOF and EMCal, the forward production is measured with the Muon Spectrometer, while the triggering and background suppression is done with V0, AD, ZDC. The schematics of the ALICE detector can bee seen in Fig. 2.

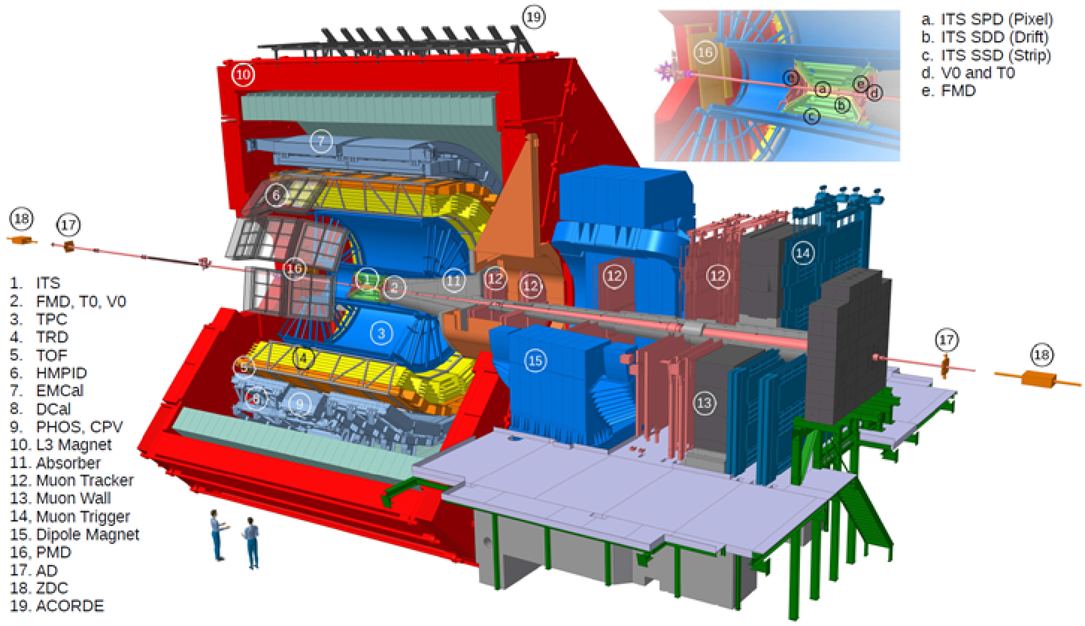

Figure 2: Schema of the ALICE detector [1].

ALICE measurements of the differential cross section for J/Ψ photoproduction in Pb-Pb UPC, from Run 1 and Run 2, are presented in Fig. 3 and Fig. 4, respectively [2, 3]. Fig. 3 shows comparison of central and forward rapidity data compared with theoretical predictions and Fig. 4 shows only the comparison of preliminary forward rapidity data with models.

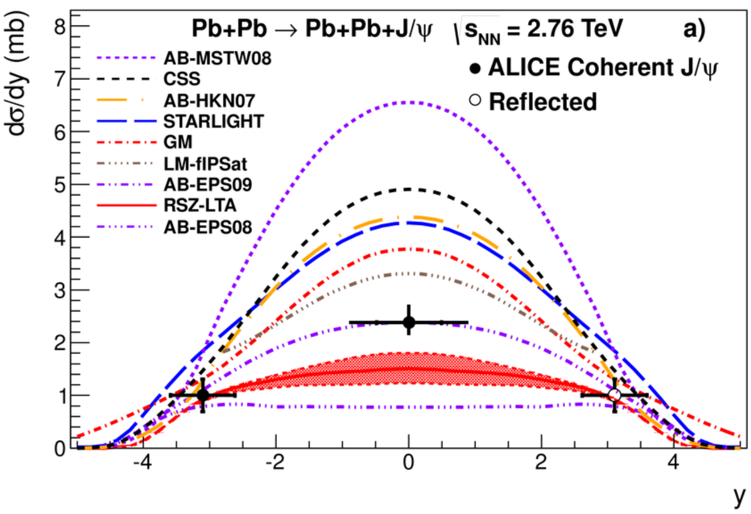

Figure 3: Differential cross section for coherent J/Ψ photoproduction from Run 1 [2].

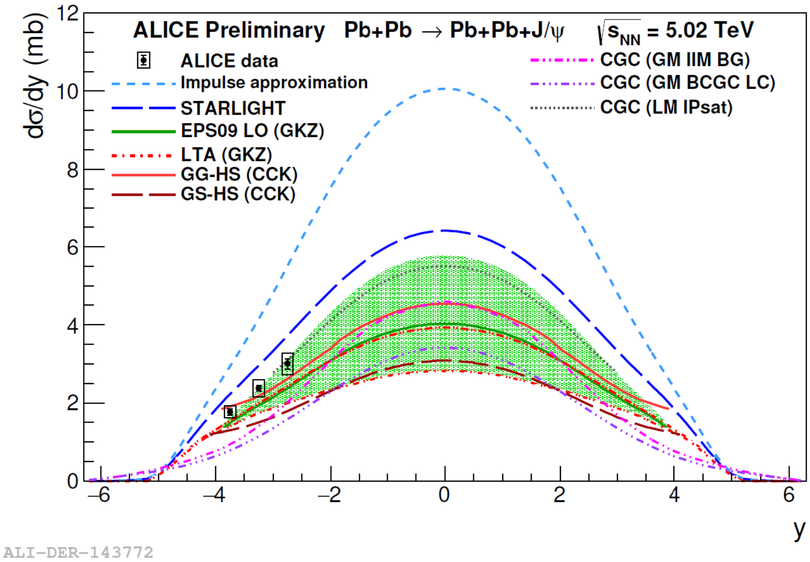

Figure 4: Differential cross section for coherent J/Ψ photoproduction from Run 2 [3].

Both results from Run 1 and Run 2 data favour models with moderate amount of nuclear shadowing. In November 2018 new data have been recorded, producing a large increase in the size of the data sample available for analyses. These data are currently being analysed and new results will be available soon, constraining theoretical models even further.

References

[1] Arturo Tauro. ALICE Schematics. General Photo, [Online; accessed 29-June-2017], Available at: http://cds.cern.ch/record/2263642, May 2017.

[2] E. Abbas *et al.* [ALICE Collaboration], "Charmonium and e^+e^- pair photoproduction at mid-rapidity in ultra-peripheral Pb-Pb collisions at $\sqrt{s_{\rm NN}}$=2.76 TeV," Eur. Phys. J. C **73** (2013) no.11, 2617 doi:10.1140/epjc/s10052-013-2617-1 [arXiv:1305.1467 [nucl-ex]].

[3] E. L. Kryshen [ALICE Collaboration], "Photoproduction of heavy vector mesons in ultra-peripheral Pb-Pb collisions," Nucl. Phys. A **967** (2017) 273 doi:10.1016/j.nuclphysa.2017.05.083 [arXiv:1705.06872 [nucl-ex]].

Betatron radiation and its application

Lenka Hronová*(lenkahronov@seznam.cz)*

Laser plasma accelerator (LPA) is quite a new concept in the field of particle acceleration. First proposed by Tajima and Dawson in 1979, it is still an active field of research nowadays. The principle behind LPAs is the excitation of plasma waves using a high intensity laser pulse. LPAs have several advantages such as compactness and high accelerating gradients (tens of GeV/m). This can be explained by the fact that electrons are accelerated in plasma that is already broken down, therefore there is no breaking limit, compared to conventional accelerators.
Development of LPAs paves the way for particle acceleration on small distances while still being able to achieve high energies of particles. This process of acceleration is useful not only for accelerating but also as a compact source of radiation which can be used in many applications.
Betatron radiation is caused by oscillations of accelerated electrons. Electrons with certain properties are trapped inside the waves of plasma created behind the laser pulse. In these plasma cavities, the electrons oscillate (so called betatron oscillations) and emit radiation. Typical transverse amplitude is about 1 μm and longitudinal period about 150 μm. With its unique properties (ultrashort low divergence pulse with continuous spectrum), betatron radiation is suitable as a backlight for spectroscopic measurements of ultrafast processes.
During my research, I was a member of a group working on the Betatron experiment with DRACO laser in Helmhotz centrum in Dresden. In this experiment, betatron radiation is used to examine the structure of warm dense matter (WDM) and the process of its creation. Warm dense matter is a state of matter between condensed matter and hot plasma. The density of WDM is 10^2-10^7kg/m^{-3} while the temperature is around $1 - 100$eV. In this mode, matter is mostly degenerate, strongly coupled and non ideal. These properties are the reason why the WDM is non trivial to simulate either theoretically, numerically nor experimentally.
In the laboratory, WDM can be produced by femtosecond isochoric heating of a solid foil. This energy is suddenly deposited in the electrons and then homogenized along the thickness, in a femtosecond time scale. This leads to strong out-of-equilibrium situation in which electrons have a high temperature while the lattice is still cold. The electron-ion thermal equilibration follows on a longer time scale (a few picoseconds). This process of solid-to-plasma transformation is a phenomenon that can be studied thanks to the ultrashort pulses of betatron radiation.
My aim was to contribute to the setup of the whole experiment, namely, calculating the sizes of the mirrors and lenses that will be used to create the path for laser pulse, and

also calculating the distances between them. Another part of my work was to setup the delay part of the laser path and laser focus diagnostics that will be used to control the heating of the solid foil.
Using the mirror, the laser beam is split into two parts - the outer ring and the central part. The outer laser ring, used for heating the solid target, is focused. My task was to find out whether it is possible to focus the beam with some lens and to calculate the appropriate lens parameters. The central part of the laser is used for acceleration of the electrons and creation of the radiation. A so-called delay line, comprising of two mirrors, will lengthen the laser path, therefore securing the backlight of the foil in different phases of solid-to-plasma transition.

References

[1] M. Koenig et al, Plasma Phys. Control. Fusion 47 (2005) B441–B449.

[2] B. Mahieu et al, Nature Communications vol 9 (2018) 3276.

[3] S. Shiraishi, Springer International Publishing (2015) 2190-5053.

Characterization of monolithic detectors for space applications

Anežka Kabátová*(kabatane@fjfi.cvut.cz)*

1 Introduction

Monitoring of the space weather near Earth is an important feature of possible predictions of solar events that can be dangerous for electronic systems as well as astronauts on space missions. Our aim is to develop a reliable device for the particle detection with a sufficient energetic range and also the capability to operate in the extreme radiation environment. The latest model of such a device is SpacePix, monolithic silicon detection chip developed at the FNSPE CTU. While the SpacePix chip was still under development, a technology demonstrator, X-CHIP-03, was used to determine response and radiation hardness of the selected technology.

1.1 Detection device X-CHIP-03

A radiation detection device X-CHIP-03 (shown in Figure 1, left) consists of square pixel cells with a 60 μm pitch covering an active area of 3.84×3.84 mm^2. X-CHIP-03 has two operation modes – hit counting mode and ADC mode dedicated to the measurement of deposited energy in pixels [2].
The main application of X-CHIP-03 is radiation imiging, but since it has been designed in the same technology as the SpacePix chip, the radiation hardness testing can provide valuable information for its design. The intended application of the SpacePix requires sufficient radiation tolerance to single event upsets (SEU). For the evaluation of SEU cross-section of X-CHIP-03, data from irradiation by protons and various ions (helium, carbon, xenon, argon, neon) were used.

2 Single event upset evaluation

One of stated goals was to specify bit flip cross-section. Bit flip is an alternation in binary information in digital part of the detection chip [1]. In order to determine the number of SEUs, a measurement was made at the U400M isochronous cyclotron at the Joint Institute for Nuclear Research in Dubna, Russia. U400M started operating in 1991 and specializes in the acceleration of "radioactive beams", very neutron-rich and thus radioactive elements.
X-CHIP-03 was irradiated by neon, argon and xenon ions with energies approximately 3,5 MeV/n with fluence as high as $234 \pm 67 \cdot 10^6$ cm^{-2}. The number of induced bit-flips

differs from 2387 for xenon to 7442 for argon.
Ions with sufficient energy can reach the sensitive area of the chip and create clusters, as is shown in Figure 1 (right). The placement of X-CHIP-03 in the vacuum chamber in JINR can be found in Figure 2.

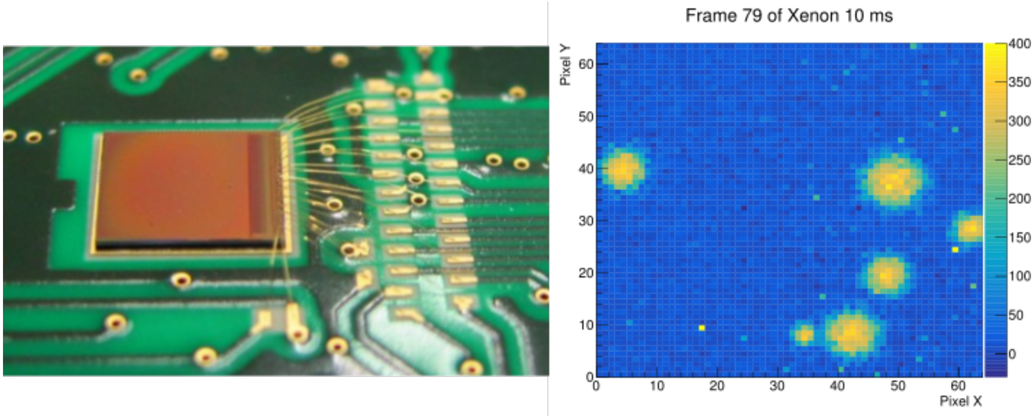

Figure 1: X-CHIP-03 ASIC and its response to irradiation with neon ions.

Another measurement was performed at Tandetron, a tandem accelerator at the Nuclear Physics Institute of the Czech Academy of Sciences (NPI CAS), Řež, Czech Republic. X-CHIP-03 was irradiated by ions with lower LET, namely carbon and oxygen. X-CHIP-03 was placed in a vacuum chamber. Energies of used ions were determined by the Monte Carlo simulations made in Geant4, as well as SRIM simulations provided by the NPI CAS.

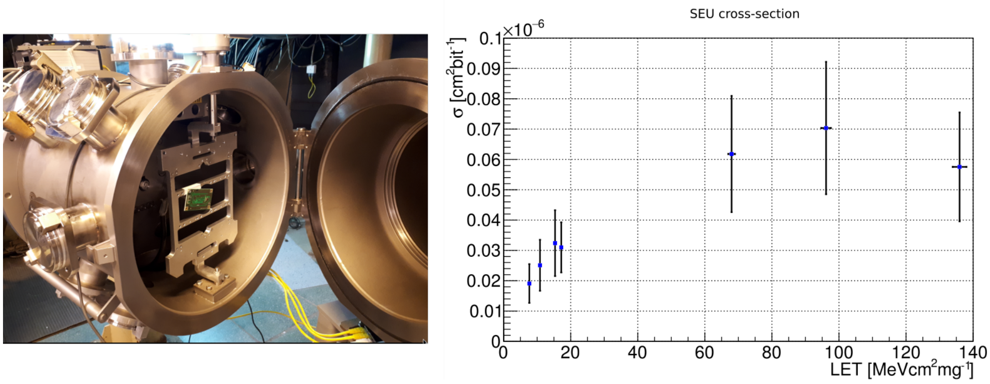

Figure 2: The placement of X-CHIP-03 in the vacuum chamber in JINR on accelerator complex U400M and SEU cross-section as a function of LET of ion.

Based on measurement results from JINR and NPI CAS, LET dependence of SEE cross-section was evaluated. Figure 2 shows the measured data points of bit flip cross-section. The desired radiation tolerance was not confirmed because of specific components used in the detector design, D flip flops, which compose shift registers of the ASIC and are susceptible to SEUs. Therefore, this part of the digital design was replaced in the SpacePix ASIC.
Moreover, the homogeneity of number of SEUs among shift registers was analyzed to prove that even though the radiation tolerance was not proven sufficient, the behavior of registers does not differ from one to another.

3 Calibration of response of individual pixels

X-CHIP-03 can also be used for the spectroscopy. In the Centre of Applied Physics and Advanced Detection Systems (CAPADS), X-CHIP-03 was engaged in the measurement of spectra of radiation sources iron ^{55}Fe and plutonium ^{238}Pu. The resulting response clearly shows the main photon energy peaks and the pedestal, as can be seen in Figure 3. To get the information about the initial energy of the impinging ion, each pixel has to be calibrated. Known spectra can be used for this purpose. Each peak with a value in ADC units corresponds to the known peak of measured spectra. The resulting calibration curve is pixel-specific, as can be seen in Figure 3.

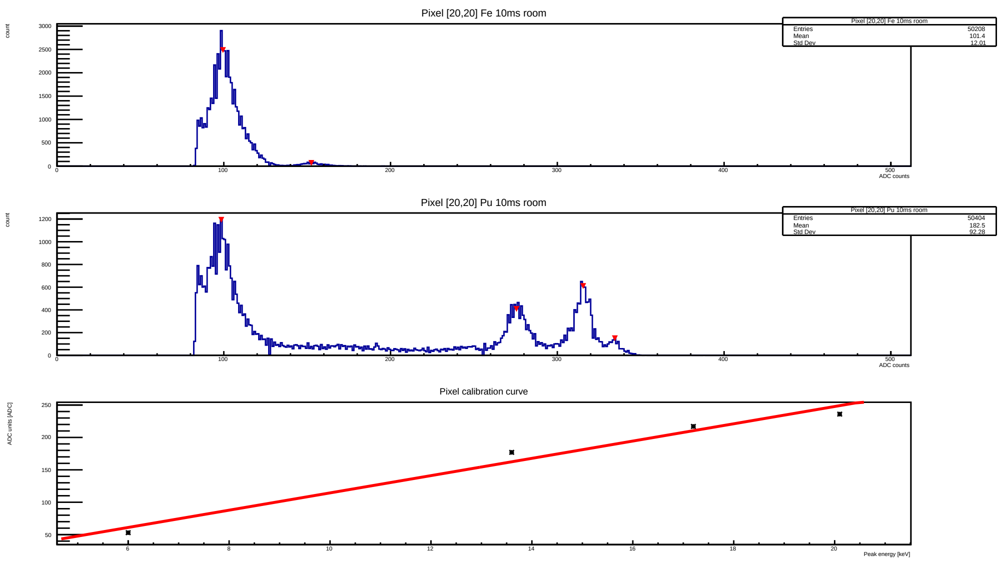

Figure 3: Peaks found in chosen known spectra and calibration curve of pixel (20, 20) of X-CHIP-03.

4 Conclusion

Multiple measurement were performed using X-CHIP-03 to tests its capabilities to operate in extreme environments and to demonstrate several of its possible applications. Based on these results, next generation of detection devices (SpacePix) was designed to be more suitable for space weather monitoring. To prove this, similar experiments will be run using SpacePix ASICs in the near future.

References

[1] E. De Donder, Space Radiation Effects, https://www.spenvis.oma.be

[2] M. Havranek et al., MAPS sensor for radiation imaging designed in 180 nm SOI CMOS technology, JINST 13, 06 (2018) C06004.

Overview of quarkonium production and suppression

Leszek Kosarzewski *(kosarles@fjfi.cvut.cz)*

1 Introduction

Quarkonium production is a tool for studying properties of Quark-gluon Plasma. It is made of quarks and gluons, which are moving freely in the plasma instead of being confined in hadrons. Such plasma requires high temperature or density and can be experimentally recreated in relativistic heavy-ion collisions. Quarkonium states like J/ψ or Υ interact with the plasma and dissociate if the temperature is high enough. This is expected to be due to the Debye-like screening of color charges [1]. In fact a sequential pattern of quarkonium suppression is expected [2]. It has been observed for Υ production at LHC [3].

Here, I would like to focus on recent results of quarkonium production from the STAR experiment.

2 Quarkonium production in p+p collisions

By measuring the quarkonium production in p+p collisions an important information can be gained about quarkonium production mechanism. They also serve as a reference for heavy-ion collisions. STAR has measured both J/ψ [4] and Υ production in p+p collisions at 200 and 500 GeV. Fig. 1 shows J/ψ(left) and Υ (right) invariant cross sections in p+p collisions at 200 and 500 GeV respectively. The Color Evaporation Model [5] can describe the results reasonably well. The NRQCD calculation coupled with CGC framework is above the data points however.

Production of J/ψ and Υ has also been studied as a function of charged particle multiplicity. Fig. 2(left) shows a self normalized quarkonium yield plotted vs. self normalized charged particle multiplicity N_{ch}. Such a dependence provides information about the behavior of hard vs. soft QCD processes. The data are qualitatively consistent with a strong increase with N_{ch} and show a similar trend both at RHIC and LHC. The data are compared to the models, which suggest quarkonium production happens in multiple parton interactions(PYTHIA) or that there are interactions between strings of color field(Percolation), which suppress the N_{ch} yield.

3 Quarkonium production in Au+Au collisions

Quarkonium production has been measured in STAR in Au+Au collisions both in e^+e^- and $\mu^+\mu^-$ channels at 200 GeV. Nuclear modification factor R_{AA} has been measured for

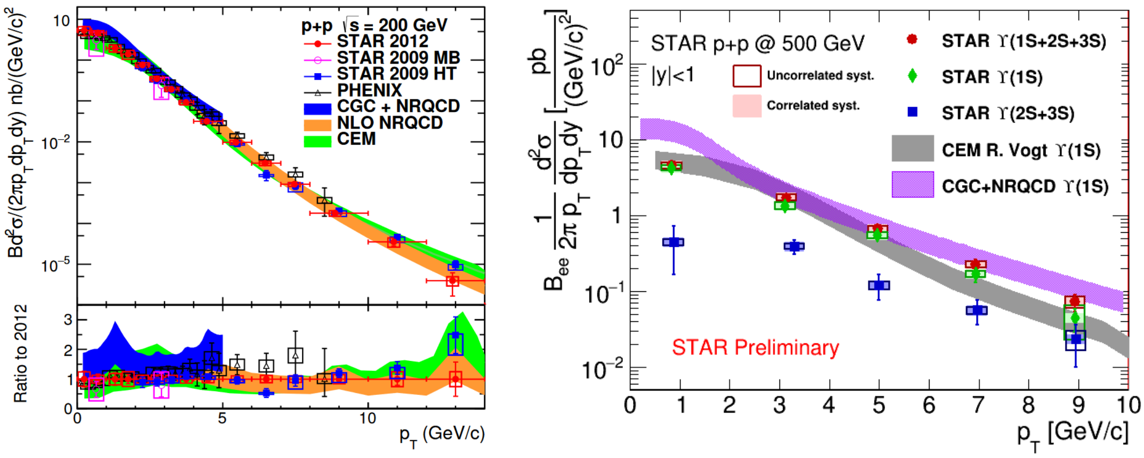

Figure 1: Invariant cross section vs. p_T for J/ψ [4] (left) and different Υ states (right) production compared to different models [5, 6, 7].

J/ψ and Υ and shows suppression for both mesons. The R_{AA} vs. number of nucleons participating in a collision N_{part} is presented in Fig. 3. STAR results are compared to CMS results and show a similar level of suppression for $\Upsilon(1S)$. This is surprising, given a higher medium temperature at LHC than at RHIC. A possible explanation may be a stronger regeneration at LHC. There is, however and indication of smaller suppression of $\Upsilon(2S + 3S)$ at RHIC than at LHC.

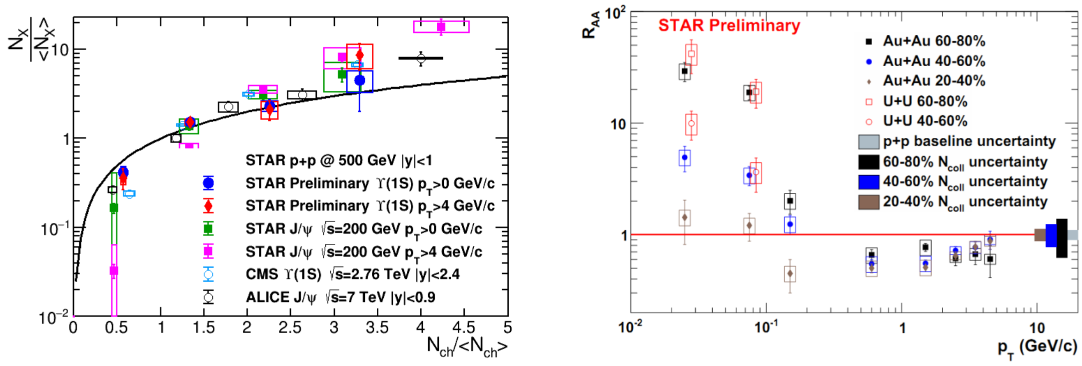

Figure 2: Left: Normalized Υ production vs. normalized charged particle multiplicity. Right: Nuclear modification factor R_{AA} vs. p_T for J/ψ for different centralities in Au+Au and U+U collisions.

4 Summary

STAR has so far measured quarkonium production in different collision systems: p+p(200 and 500 GeV), p+A, d+Au and Au+Au. This amounts to a comprehensive study of quarkonium production and provides information about production mechanism and QGP properties.

Acknowledgements

Supported by the Ministry of Education, Youth and Sports of the Czech Republic under grant CZ.02.2.69/0.0/0.0/16_027/0008465

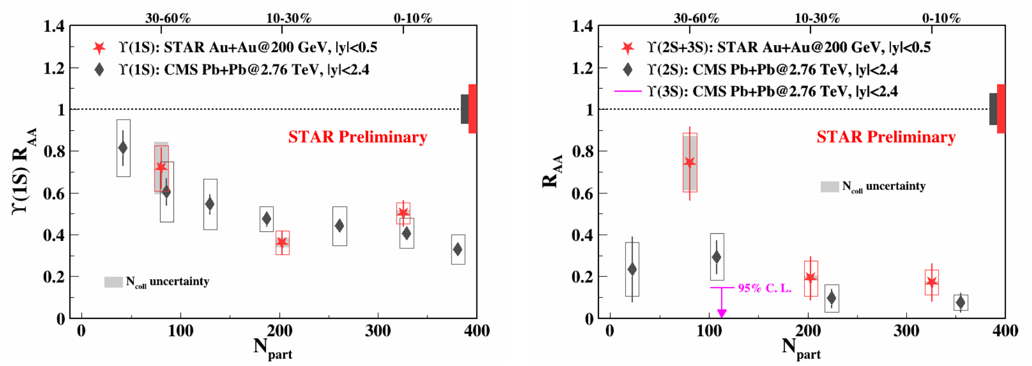

Figure 3: Nuclear modification factor R_{AA} vs. N_{part} for $\Upsilon(1S)$(left) and $\Upsilon(2S), \Upsilon(3S)$(right). STAR results are compared with CMS [8].

References

[1] Matsui, T., Satz, H. (1986). Physics Letters B, 178(4), 416–422. https://doi.org/10.1016/0370-2693(86)91404-8

[2] Karsch, F., Kharzeev, D., Satz, H. (2006). Physics Letters B, 637(1–2), 75–80. https://doi.org/10.1016/j.physletb.2006.03.078

[3] Chatrchyan, S., Khachatryan, et al. (2012). Physical Review Letters, 109(22), 222301. https://doi.org/10.1103/PhysRevLett.109.222301

[4] Adam, J., Adamczyk, L., et al. (2018). Physics Letters B, 786, 87–93. https://doi.org/10.1016/j.physletb.2018.09.029

[5] Vogt, R. (2015). Physical Review C, 92(3), 034909. https://doi.org/10.1103/PhysRevD.94.114029

[6] Han, H., Ma, Y.-Q., et al. (2016). Physical Review D, 94(1), 014028. https://doi.org/10.1103/PhysRevD.94.014028

[7] Ma, Y.-Q., Wang, K., Chao, K.-T. (2011). Physical Review D, 84(11), 114001. https://doi.org/10.1103/PhysRevD.84.114001

[8] Khachatryan, V., Sirunyan, A. M., et al. (2017). Physics Letters B, 770, 357–379. https://doi.org/10.1016/j.physletb.2017.04.031

A guide to understand collectivity in small systems

Katarína Křížková Gajdošová*(katarina.gajdosova@fjfi.cvut.cz)*

1 Introduction

Collisions of heavy ions at ultrarelativistic energies serve to recreate a deconfined state of, the Quark-Gluon Plasma (QGP). In a hydrodynamic picture, the collective evolution of this medium translates the initial spatial anisotropies in the overlap region of the colliding heavy nuclei into an anisotropy of fi

nal state particles. To characterise this anisotropy, the azimuthal distribution of emitted particles can be decomposed into a Fourier expansion with respect to a common symmetry plane Ψ_n with anisotropic flow coefficients $v_n = \langle \cos n(\varphi - \Psi_n) \rangle$:

$$\frac{dN}{d\varphi} \propto 1 + 2\sum_{n=1}^{\infty} v_n \cos[n(\varphi - \Psi_n)]. \tag{1}$$

The flow harmonics v_n quantify the preferred direction of emitted particles, and represent a collective response of the QGP to the initial spatial anisotropies. This collective behaviour manifests itself in the form of long-range multi-particle correlations between the final state particles.

2 How to measure flow

2.1 Di-hadron correlations

By correlating two particles (hadrons) with (φ_1, η_1) and (φ_2, η_2), one can obtain a two-particle correlation function $C(\Delta\varphi, \Delta\eta)$. A typical picture from a di-hadron correlation is shown in Fig. 1 (left).

In the region of near-side ($\Delta\varphi \approx 0$) short-range ($\Delta\eta \approx 0$) correlations there is a *jet peak*, mainly resulting from correlations between particles within a jet cone, or high-p_{T} resonance decays. At $\Delta\varphi \approx \pi$, there is a visible *away-side ridge* structure spanning long-range in pseudorapidity ($\Delta\eta \gg 0$), usually originating from low-p_{T} resonances or correlations between particles from the two opposite cones of a di-jet. Finally, a *near-side ridge* can be observed, which is attributed to the collective expansion of the system. This is a feature specific to heavy-ion collisions, indicating the presence of long-range correlations.

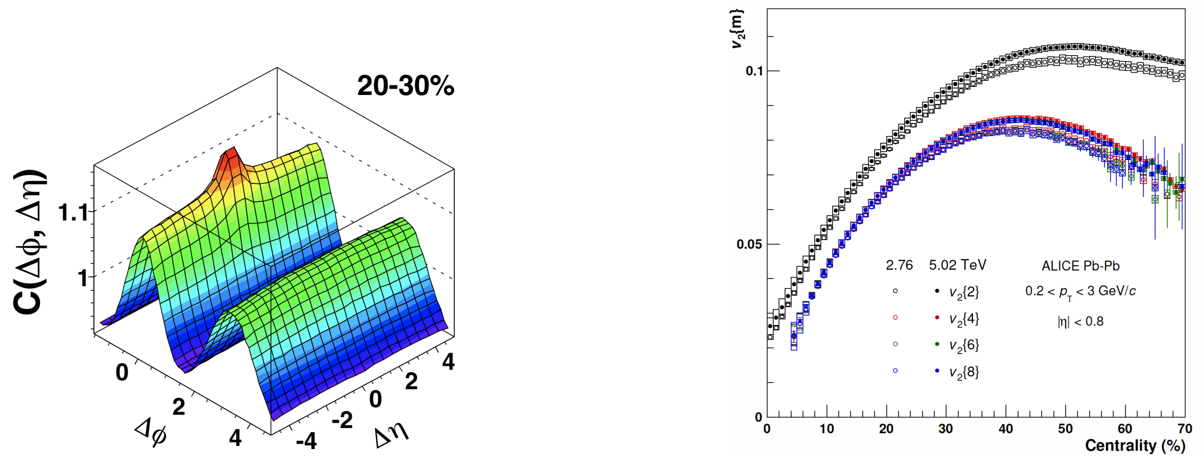

Figure 1: Left: Di-hadron correlation as a function of $\Delta\varphi$ and $\Delta\eta$ in Pb–Pb collisions at $\sqrt{s_{\mathrm{NN}}} = 2.76$ TeV [1]. Right: Measurements of flow coefficient v_2 using multi-particle cumulants in Pb–Pb collisions at $\sqrt{s_{\mathrm{NN}}} = 5.02$ TeV [2]

2.2 m-particle cumulants

Because the flow coefficients cannot be directly measured using their definition above, m-particle correlations are employed instead. These are then used to compose the cumulants of the v_n distribution, from which one can estimate the v_n coefficients [3, 4]. The justification to use m-particle correlations is depicted in the following:

$$\langle\langle 2\rangle\rangle = \langle\langle \cos n(\varphi_1 - \varphi_2)\rangle\rangle = \langle v_n^2\rangle, \tag{2}$$

where the $\langle\langle\cdot\rangle\rangle$ represents the average over particle m-tuplets in an event, and an average over the event sample (with similar characteristics). However, the four-particle correlation (and higher orders) also contains contributions from two-particle correlations. By subtracting these contributions from the four-particle correlation, we get the *genuine* four-particle correlations, which we call the four-particle cumulant $c_n\{4\} = \langle\langle 4\rangle\rangle - 2\cdot\langle\langle 2\rangle\rangle^2$. In case of two-particle correlations, the $\langle\langle 2\rangle\rangle$ is directly equal the two-particle cumulant $c_n\{2\}$. Higher order cumulants can be derived in a similar way.

Eventually, having the multi-particle cumulants in hand, one can get the flow coefficients:

$$\begin{aligned} v_n\{2\} &= \sqrt{c_n\{2\}} \qquad & v_n\{4\} &= \sqrt[4]{-c_n\{4\}} \\ v_n\{6\} &= \sqrt[6]{1/4\cdot c_n\{6\}} \qquad & v_n\{8\} &= \sqrt[8]{-1/33\cdot c_n\{8\}}, \end{aligned} \tag{3}$$

where the $\{\cdot\}$ represents the order of the cumulant. An example of measurements of the elliptic flow using m-particle cumulants is shown in Fig.1 (b). The fact that a real valued $v_n\{4\} \sim v_n\{6\} \sim v_n\{8\}$ could be obtained indicates a presence of multi-particle correlations.

3 Collectivity in small systems

Over the past few years, striking similarities with heavy-ion collisions were also observed in small collision systems. A near-side ridge was revealed in high multiplicity pp and p–Pb collisions [5], triggering a question of whether QGP is also present in small systems.

At first, a negative $c_2\{4\}$ was only observed in p–Pb collisions [6] indicating collectivity, while in pp collisions the $c_2\{4\}$ remained positive. However, small collision systems are contaminated by non-flow effects, mostly originating from jets or resonance decays. Recently developed subevent method [7] is able to reduce such contributions. It consists of dividing the detector into two or more subevents and correlating particles only from different subevents. With the use of this method, a negative $c_2\{4\}$ was recently revealed even in pp collisions [8], also shown in Fig. 2.

The above mentioned observations suggest that collectivity is indeed present in small collision systems. Further comparison to theoretical models, and measurements of observables more sensitive to different aspects of these models will help to study the origin of the collectivity in small systems.

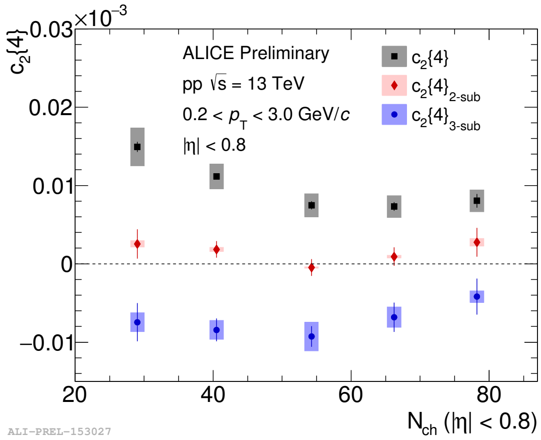

Figure 2: Multiplicity dependence of four-particle cumulant $c_2\{4\}$ in pp collisions at $\sqrt{s} = 13$ TeV, calculated with the standard, 2-subevent and 3-subevent method [9]. The suppression of non-flow contamination is apparent.

References

[1] G. Aad *et al.* (ATLAS Collaboration), Phys.Rev.C86, 014907 (2012)

[2] S.Acharya *et al.* (ALICE Collaboration) JHEP 1807 (2018) 103

[3] N. Borghini, P.M.Dinh and J.Y.Ollitrault, Phys.Rev.C63, 054906 (2001)

[4] A. Bilandzic, R. Snellings and S. Voloshin, Phys.Rev.C83, 044913 (2011)

[5] M. Aaboud *et al.* (ATLAS Collaboration) Phys.Rev.C96, 024908 (2017)

[6] B. Abelev *et al.* (ALICE Collaboration) Phys.Rev.C90, 054901 (2014)

[7] J. Jia, M. Zhou and A. Trzupek, Phys.Rev.C96, 034906 (2017)

[8] M. Aaboud *et al.* (ATLAS Collaboration), Phys.Rev.C97, 024904 (2018)

[9] K. Gajdošová (for the ALICE Collaboration), Nucl.Phys.A982 (2019) 487

Measurement of top quark pair differential cross section

Diana Mária Krupová*(krupodia@fjfi.cvut.cz)*

1 Top quark production and decay in LHC

Top quark with the mass of 172,5 GeV is the heaviest of all SM quarks, the typical time scale of top quark event is given by fast electroweak decay ($t \to Wb$) - 10^{-25} s. It is shorter than typical hadronization time scale ($\sim 1/\Lambda_{QCD}$) and leads to preservation of properties of the quark itself in the final states. Therefore, the top quark is a perfect candidate to study any changes in behaviour as point-like particle. This behaviour would point to beyond standard model (BSM) physics.

By the end of its Run 3, with an integrated luminosity 300 fb^{-1}, LHC should have produced approximately 2.10^8 $t\bar{t}$ pairs - behaving like the top quark factory, thus providing the opportunity to explore the intrinsic properties of top with unprecedented accuracy.

In the LHC, top quark can be produced as a single top or a top quark pair. Measuring the differential cross section of $t\bar{t}$ is more appropriate for our needs: it can be used to set the boundaries for existence of new physics..

The signature of $t\bar{t}$ final state is given by W boson decay. ATLAS and CMS published measurements of $t\bar{t}$ differential cross section with centre-of-mass energy 7, 8 and 13 TeV in proton collisions using final states containing leptons. Our analysis will use all-hadronic $t\bar{t}$ decays and we will select only top quark candidates with high transverse momentum.

2 Effective field theory

We require the effective field theory model to satisfy the $SU(3)_C \times SU(2)_L \times U(1)_\gamma$ symmetry of SM. With this requirement, the only operator of dimension 5 violates the lepton number conservation. The main effects are generated by dimension 6 operators $\mathcal{O}_i$:

$$\mathcal{L}_{\text{eff}} = \mathcal{L}_{\text{SM}} + \frac{1}{\Lambda^2}\sum_i (C_i\mathcal{O}_i + h.c.)$$

where C_i are dimensionless coefficients. These interactions are suppressed by a factor of inverse Λ, which gives us the scale where the new physics happens. From the list of all parameters, only 59 are independent. Initially, we just added two effective operators $\mathcal{O}_1$ and $\mathcal{O}_2$ and studied their impact on the differential cross section. The shapes of normalized $1/\sigma\ \mathrm{d}\sigma/\mathrm{d}m_{t\bar{t}}$ and $1/\sigma\ \mathrm{d}\sigma/\mathrm{d}p_t$ distributions are not affected by the presence of $\mathcal{O}_2$ operator in any way. All of this was so far done at parton level. Next plan is to include hadronization, add all the parameters, compare them to kinematic distributions using only SM and also to the measured data from ATLAS.

References

[1] ATLAS Collaboration. *Measurements of $t\bar{t}$ differential cross-sections of highly boosted top quarks decaying to all-hadronic final states in pp collisions at $\sqrt{s} = 13$ TeV using the ATLAS detector*, `arXiv:1801.02052[hep-ex]`

[2] D. Barducci, M. Fabbrichesi, A. Tonero. *Constraints on top quark non-standard interactions from Higgs and $t\bar{t}$ production cross sections*, `arXiv:1704.05478v2[hep-ph]`

[3] F. Fabbri. *Top pair and single top production in ATLAS*, `https://cds.cern.ch/record/2281546`

[4] P. Ferreira Da Silva. *Top quark production at the LHC*, `arXiv:1605.05343v1[hep-ex]`

Reconstruction of Λ particle in Au+Au collisions at 27 GeV with KF Particle Finder

Jakub Kubát *(kubatja8@fjfi.cvut.cz)*

KF Particle is a package of C++ libraries developed by the FIAS group initially for experiments CBM and ALICE. It is based on Kalman filter (KF), which is a recursive algorithm for analysis of linear discrete systems described by a vector of parameters. KF Particle exploits this algorithm for estimation of parameters of particle trajectories in collision events and also for reconstruction of short-lived particles. KF Particle Finder is an interface which makes use of the KF Particle package in order to give its user opportunity to study wide range of particle decays [1].

Benefits of the KF Particle package include independence of the experiment geometry, which has lead to a succesful implementation of KF Particle in analyses at STAR. Another advantage is KF Particles's complete vectorization which enables it to run on computers with Single Instruction Multiple Data (SIMD) architectures. This is a crucial atribute for future application of KF Particle in online reconstruction of particles at CBM experiment [2].

KF Particle describes particle trajectories with state vector and covariance matrix

$$\mathbf{r} = (x, y, z, p_x, p_y, p_z, E)\,, \qquad C = \left\langle \mathbf{r} \cdot \mathbf{r}^T \right\rangle. \tag{1}$$

The knowledge of the covariance matrix is important for the reconstruction of short-lived particles. KF Particle Finder defines probability criteria based on χ^2 statistics which characterize the probability of particles being primary (coming from primary vertex) or particle trajectories intersecting within their errors and so on. This serves as an interesting alternative to the standard analysis procedure, in which one makes cuts on topological variables like DCA or pointing angle regardless of the goodness of fit of trajectories. Using KF Particle Finder trajectories are studied one by one and cuts are being made on probabilties, which can lead to an improvement in the yields of reconstructed particles. One can also use the χ^2 values as variables for multivariate analysis and further enhance the yields or significance of the signal for example with ROOT integrated Toolkit for Multivariate Analysis (TMVA).

In this work KF Particle was applied on data from Au+Au collisions at 27 GeV measured at STAR experiment at Brookhaven National Laboratory as a part of Beam Energy

Scan I program. The aim was to compare the yields of Λ particles obtained using KF Particle with results from standard analysis that employs cuts on geometrical variables. The decay channel under study was $\Lambda \rightarrow p + \pi^-$. The analysis used for comaprison was done by Xianglei Zhu, Tsinghua University. However, these results were not published yet.

The comparison can be seen in Tab.1. It shows that in lower- to mid-p_T bins KF Particle seems to be more effective. However, at higher p_T the standard analysis exceeds KF Particle. It is important to point out that for $0.2 < p_T < 0.4$ GeV no signal of Λ was presented in the standard analysis, but with KF Particle it was possible to reconstruct the particle with decent signal significance. The Fig.1 shows invariant mass spectrum for this p_T range. The yield of Λ was calculated using sideband method and significance was calculated as $SG = S/\sqrt{S+B}$.

p_T [GeV]	S$\times 10^6$	S/B	SG$\times 10^3$	S'$\times 10^6$	**S/S'**
$0.2 - 0.4$	0.167 187	0.68	0.260	-	-
$0.4 - 0.6$	1.359 380	3.52	1.029	0.974 110	**1.40**
$0.6 - 0.8$	3.054 310	6.66	1.630	2.440 170	**1.25**
$0.8 - 1.0$	3.996 500	8.06	1.885	3.141 470	**1.27**
$1.0 - 1.2$	3.936 860	8.74	1.879	3.023 950	**1.30**
$1.2 - 1.4$	3.227 950	9.44	1.708	2.400 580	**1.34**
$1.4 - 1.6$	2.324 770	9.67	1.451	1.745 920	**1.33**
$1.6 - 1.8$	1.529 170	9.60	1.177	1.135 030	**1.35**
$1.8 - 2.0$	0.945 039	9.40	0.924	0.720 610	**1.31**
$2.0 - 2.3$	0.732 525	8.92	0.812	0.555 128	**1.32**
$2.3 - 2.6$	0.299 153	8.28	0.517	0.242 896	**1.23**
$2.6 - 3.0$	0.134 677	7.43	0.345	0.119 532	**1.13**
$3.0 - 3.4$	0.035 907	6.60	0.177	0.035 799	**1.00**
$3.4 - 3.9$	0.010 574	5.91	0.095	0.021 758	**0.49**
$3.9 - 4.4$	0.001 726	3.50	0.037	0.004 570	**0.38**
$4.4 - 5.0$	0.000 314	2.47	0.015	0.001 184	**0.27**
$5.0 - 6.0$	0.000 123	5.35	0.010	0.001 184	**0.10**

Table 1: The comparison of raw Λ yield S obtained with KF Particle with yield S' obtained from standard analysis in different transverse momentum bins. Signal to background ratio S/B and significance SG are also shown.

KF Particle Finder shows to be promising alternative to standard analysis using topological cuts due to its consideration of uncertainties of particle trajectories. Although it was initially designed to help with fast online reconstruction of particles at CBM experiment and in this manner it was tested as a part of High Level Trigger at STAR, it is also applicable in in-depth offline analyses of high energy physics data. Especially in combination with TMVA methods.

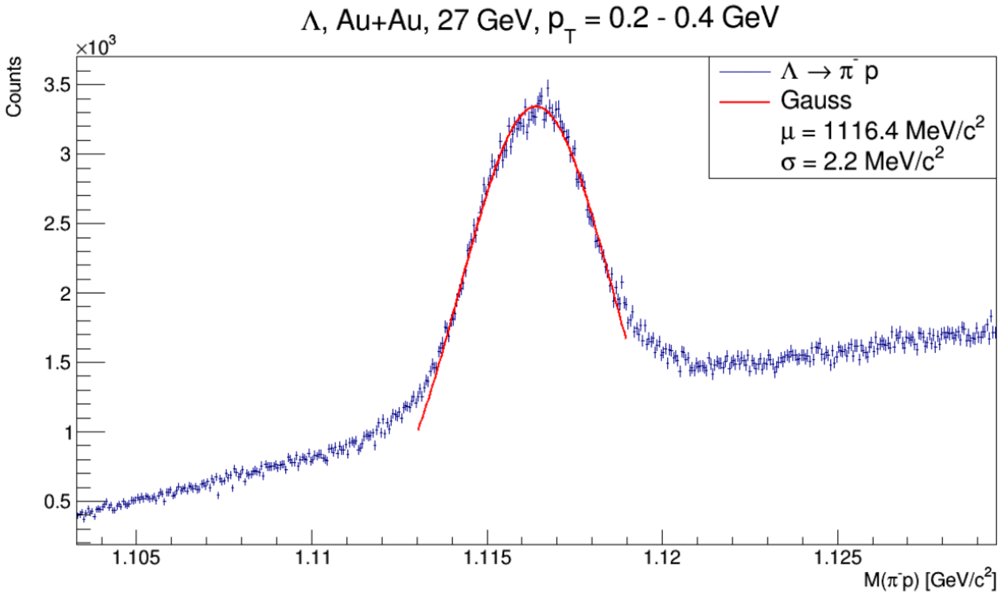

Figure 1: Invariant mass spectrum of p and π^-. The signal of Λ is fitted with Gaussian to estimate the width of the peak. The yield is than calculated using the sideband method.

References

[1] M. Zyzak, *Online selection of short-lived particles on many-core computer architectures in the CBM experiment at FAIR*, Dissertation thesis, Goethe University of Frankfurt [online]. 2016 [cit. 2019-01-13]. Dostupné z: `http://publikationen.ub.uni-frankfurt.de/frontdoor/index/index/docId/41428`

[2] I. Kisel, Gh. Adam, J. Buša a M. Hnatič. *New Approaches for Data Reconstruction and Analysis in the CBM Experiment*. EPJ Web of Conferences [online]. 2016, 108 [cit. 2019-01-13]. Dostupné z: `http://www.epj-conferences.org/10.1051/epjconf/201610801006`

$D^{\pm}$ Meson Production in Au+Au Collisions at $\sqrt{s_{\mathrm{NN}}} = 200$ GeV at STAR

Robert Líčeník *(licenrob@fjfi.cvut.cz)*

1 Introduction

The strong interaction, which is the dominant force at the femtometer scale, can be successfully described by Quantum Chromodynamics (QCD). Calculations within this framework predict a phase transition of hadronic matter to the Quark-Gluon Plasma (QGP) state at high temperatures ($\sim$ 170 MeV [1]). The main difference is that in the QGP the quarks and gluons behave as if they were free in sharp contrast with the ordinary hadron gas phase, where we observe a confinement of color charges inside color-neutral objects - hadrons. The Universe is thought to have existed as a QGP drop about 1 microsecond after the Big Bang. Today, the QGP can only be studied when created in heavy-ion collisions at high energies available at the Relativistic Heavy-Ion Collider (RHIC) and the Large Hadron Collider (LHC). However, the QGP can exists only for tiny fractions of a second ($\sim 10^{-22}$ s) and is very extreme in all aspects. For this reason we need to use probes to study interactions within the strongly-coupled medium. There are three principal kinds of probes - soft, electromagnetic and hard. Soft probes utilize the collective behavior of particles inside the medium. The measurements of elliptic flow coefficient v_2 imply that a thermal equilibrium is achieved shortly after the collision. The electromagnetic probes include leptons and hard gamma rays, neither of which should be affected by the medium. The hard probes include jet quenching and heavy flavor (c, b quark) production, and are distinguished by the large momentum transfers involved. This work focuses on the study of the c quark interaction with the QGP via a hadronic reconstruction of $D^{\pm}$ mesons. At the STAR experiment (see Fig. 1), the daughter particles are tracked and detected by detectors, such as the Time Projection Chamber (TPC), which serves as the main tool for tracking and also for particle identification (PID) via measuring their ionization energy loss (dE/dx), the Time-of-Flight Detector (TOF), which helps the identification at higher momentum by measuring the inverse velocity ($1/\beta$) of the particles and mainly the Heavy-Flavor Tracker (HFT), a silicon detector, which is located very close to the beam line and offers excellent pointing resolution, which is necessary if we want to discriminate between the primary vertex and the secondary vertices resulting from heavy-flavor particle decays.

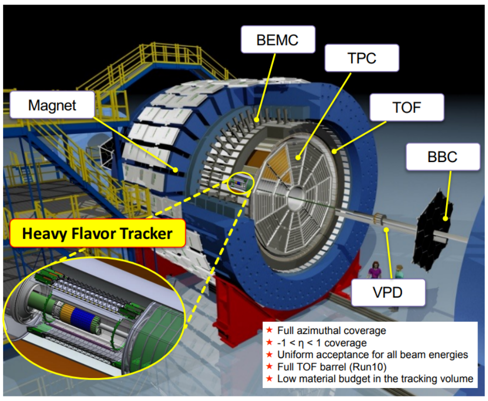

Figure 1: The STAR experiment schematic view. Main parts, including magnet, TPC, TOF, BEMC, VPD and HFT are highlighted. Taken from Ref. [2].

2 Analysis Method and Results

The charm quarks can hadronize into many different hadrons via not-yet-well-understood process of hadronization. If the charm quark binds with an anti-down quark, they form a D^+ meson and vice versa for corresponding antiparticles. Other common possibilities include the D^0 $(c\bar{u})$, D_s^+ $(c\bar{s})$ mesons and the Λ_c^+ (cdu) baryon. The $D^\pm$ meson decays exclusively via the weak interaction and the decay channel chosen for this analysis was the $D^\pm \to K^\mp\pi^\pm\pi^\pm$, since it is a channel with the highest branching ratio which is fully hadronic. The reconstruction consists of combining $K\pi\pi$ triplets that pass some selection criteria (cuts). There are 4 levels of cuts: good event selection, high-quality track selection, PID cuts and topological cuts based on the knowledge of the $D^\pm$ decay (see Fig. 2).

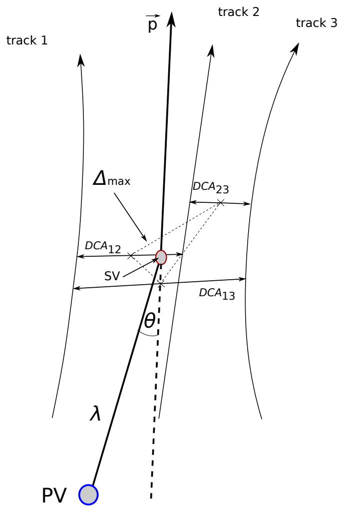

Figure 2: An illustration of the $D^\pm$ three-body decay with important topological features highlighted.

The combinatorial background can be estimated from the wrong-sign $K\pi\pi$ combinations and then subtracted to enable raw-yield extraction in various p_T and centrality bins.

The raw yield is then normalized by various factors including the detector acceptance and efficiency and compared to the results from p+p collisions to produce the nuclear modification factor

$$R_{\mathrm{AA}} = \frac{\frac{\mathrm{d}^2 N_{\mathrm{AA}}}{\mathrm{d}p_{\mathrm{T}}\mathrm{d}y}}{\langle N_{\mathrm{coll}} \rangle \times \frac{\mathrm{d}^2 N_{\mathrm{pp}}}{\mathrm{d}p_{\mathrm{T}}\mathrm{d}y}}. \tag{1}$$

The results from STAR $\mathrm{D}^{\pm}$ R_{AA} in central Au+Au collisions at 200 GeV can be seen in Fig. 3. The results are consistent with the STAR D^0 results [4] throughout the measured range with the data showing increasing suppression towards higher p_{T} and a hint of a maximal $R_{\mathrm{AA}} \sim 0.7$ around $p_{\mathrm{T}} = 3$ GeV/c.

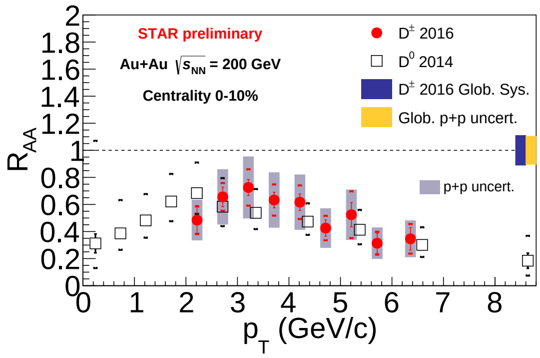

Figure 3: Preliminary results of $\mathrm{D}^{\pm}$ R_{AA} in 2016 Au+Au collisions at $\sqrt{s_{\mathrm{NN}}} = 200$ GeV for centralities 0-10 % along with the results from D^0 measurements conducted by the STAR collaboration. Taken from Ref. [3].

The results - especially in the low-p_{T} region - can be significantly improved by the application of machine-learning techniques, such as the TMVA:BDT method [5], which has great ability to discriminate between signal and background.

References

[1] Z. Fodor, S.D. Katz, "The Phase Diagram of Quantum Chromodynamics", 8/23/2009, Landolt-Boernstein Vol. 1-23A.

[2] K. Oh (STAR Collaboration), "Measurements of Charm and Bottom Productions in Semi-leptonic Channels at STAR", Quark Matter 2015, Kobe, 9/29/2015.

[3] J. Vanek (STAR Collaboration), "Production of $\mathrm{D}^{\pm}$ Mesons in Au+Au Collisions at $\sqrt{s_{\mathrm{NN}}} = 200$ GeV Measured by the STAR Experiment", Quark Matter 2018, Venice, 5/15/2018.

[4] J. Adam *et al.* (STAR Collaboration), "Centrality and transverse momentum dependence of D^0-meson production at mid-rapidity in Au+Au collisions at $\sqrt{s_{\mathrm{NN}}} = 200$ GeV", Phys. Rev. C 99, 034908 (2019).

[5] A. Hoecker *et al.*, "TMVA - Toolkit for Multivariate Data Analysis", 3/4/2007, CERN-OPEN-2007-007.

Performance of the upgraded electronics for Cherenkov and scintillator detectors of the Pierre Auger Observatory

Margita Majerčáková*(majerma3@fjfi.cvut.cz)*

1 Cosmic rays

Cosmic rays are mostly composed of nuclei of atoms, protons being the most abundant, and then from other particles like electrons, positrons, antiprotons etc. Some of these are undoubtedly the most energetic particles we can observe in nature since the big bang (up to 10^{20} eV). They may have many orders of magnitude more energy than particles artificially accelerated in big accelerators like the LHC. They may gain their energy through a diffusive shock acceleration process associated with supernova explosions, where large magnetized turbulent clouds are created, which can deflect charged particles and accelerate them in repeated shock encounters, but this effect is still not capable of achieving energies much above 10^{15} eV. We expect that the more energetic particles can originate even outside of our galaxy. At the Pierre Auger Observatory, we are measuring the extensive air showers of particles which are caused by primary particles interacting with the atmosphere.
Cosmic rays were observed for the first time by Victor Hess in 1912 on balloon flights, who used simple electroscopes with two chambers. He refuted the expectation that the atmospheric radiation originated in the ground and thus would decrease with higher altitude.

2 Pierre Auger Observatory

Pierre Auger Observatory is currently the largest astroparticle experiment operating. It is situated in Argentina, Mendoza province and it is spread over 3000 km^2. It was proposed to observe and study cosmic rays with energies above 10^{17} eV. This observatory is a hybrid detector, because it uses two types of detectors, the SD (surface detector) and the FD (fluorescence detector), which work differently but sometimes simultaneously (on dark clear nights) to provide better and more accurate measurements.

2.1 Surface detector

The SD array of surface stations is composed of 1660 water-Cherenkov detectors, which are sensitive to charged particles in the air shower front when it reaches the ground, through the Cherenkov effect in the water radiation material. These detectors are made of plastic tanks filled with clean, deionized, distilled water, and are completely dark inside. Charged particles travelling through emit light, diffusively reflected off liner walls, and then recorded by photomultipliers placed at the top of the tank looking down. There the light signal is converted into fast electronic pulses and the energy of the primary particle is derived from the signal detected by several stations, according to a well understood profile of decreasing particle activity as a function of distance from the core of the air shower. Further details of an Auger water-Cherenkov detector are given in figure 1.

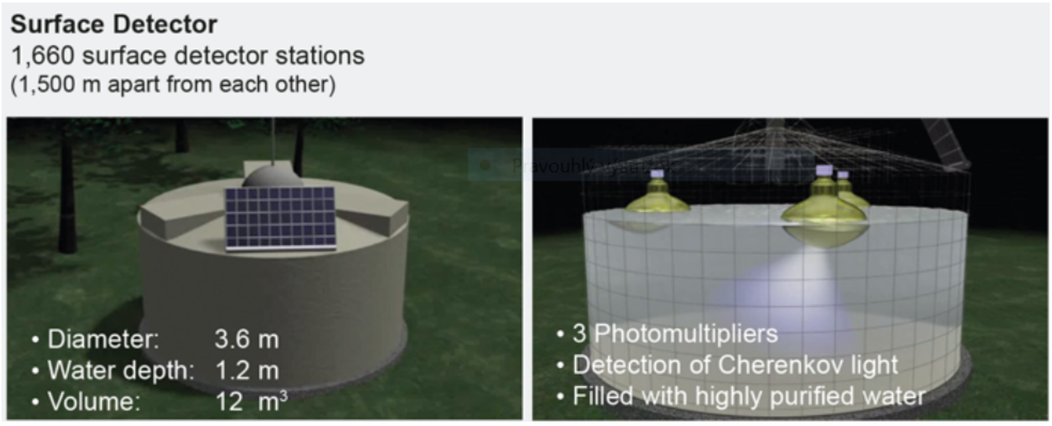

Figure 1: Surface detector station of the Pierre Auger Observatory. [1]

2.2 Fluorescence detector

The FD is a collection of fluorescence telescopes, 27 in total, arrayed at four different sites. It was designed to ensure that every event above 10^{18} eV reaching the SD should be recorded by at least one telescope on dark, clear, moonless nights. Over a more limited area, 3 of the 27 FD telescopes are tilted higher, allowing a threshold reduction down to 10^{17} eV. The FD is sensitive to nitrogen fluorescence to track the shower development, where the particle count in the developing shower is proportional to the amount of fluorescence light emitted. Excited molecules of nitrogen radiate light in the near UV part of the spectrum (mainly 300-400 mm), therefore, these telescopes can operate only during dark and moonless night, with a duty cycle of about 12%. From the integrated longitudinal profile of nitrogen fluorescence generated in the shower, the primary cosmic ray energy can be determined. Further details of the FD are given in figure 2.

3 AugerPrime

AugerPrime is upgrade of an Pierre Auger Observatory currently under deployment. As part of this upgrade, thin scintillators are being placed on top of each water-Cherenkov

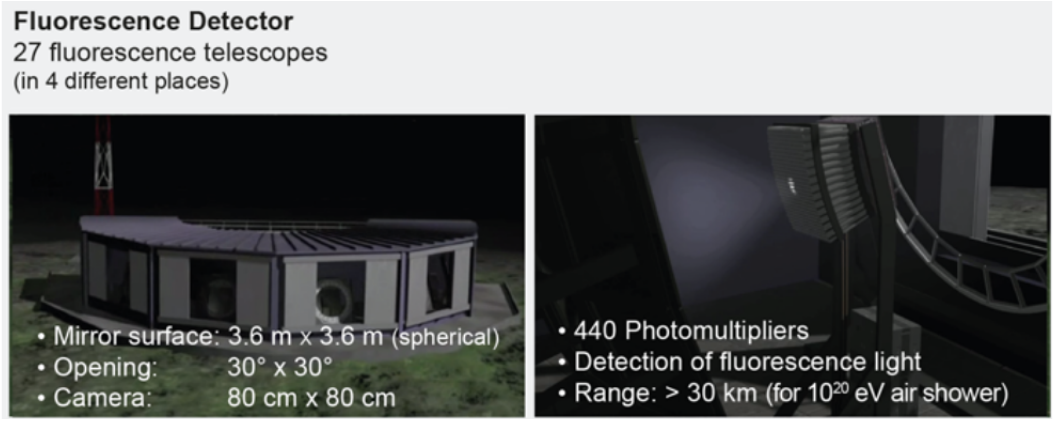

Figure 2: Fluorescence detector building of the Pierre Auger Observatory and fluorescence telescope detail. [1]

station. These scintillators are made of two plastic panels, with wavelength shifting fibres read out by one photodetector. This improvement is focused on observing both the electromagnetic and muon components of the shower, where the relative signals of the scintillation and water-Cherenkov detectors allow for disentangling these shower components on a statistical basis. A small photomultiplier tube is also being added to each water-Cherenkov station in order to increase the dynamic range of the SD. The upgrade also includes 61 muon detectors buried under the SD stations in a small region of the Observatory to detect bundles of muons and their time development a depth of 1.3m beneath the ground. Finally, the electronics are being upgraded with a new unified SD readout board, on which all functionalities required by the old and new detectors are jointly implemented.
The goal is to improve the event-by-event shower information available to refine our understanding of cosmic rays and their origin. At present, indications are that, at energies near the end of the cosmic ray spectrum (¿5.10^{19} eV) the particle flux may comprise a substantial component of nuclei heavier than protons. The AugerPrime upgrade will provide enhanced sensitivity to the details of the primary cosmic ray mass composition, which in turn will constrain models of production and propagation of these particles.

References

[1] Auger hybrid detector https://www.auger.org then click on "Hybrid Detector"

[2] Pierre Auger Collaboration. The Pierre Auger cosmic ray observatory, Nuclear Instruments and Methods in Physics Research Section A: Accelerators, Spectrometers, Detectors and Associated Equipment 798 (2015): 172-213.

[3] Aab, Alexander, et al. The Pierre Auger Observatory upgrade-preliminary design report. arXiv preprint arXiv:1604.03637 (2016).

Electron-ion collisions and their applications in particle physics

Marek Matas*(matas.marek1@gmail.com)*

Abstract

Electron-ion collisions are an important tool for verifying our current picture of how high-energy Quantum Chromodynamics (QCD) works. In this talk, I have addressed some of their key features as well as the plans for construction of future facilities that would allow us to carry out such experiments.

Summary of the lecture

The structure of the proton is one of the most interesting puzzles of these days because even though it is one of the most abundant particles in the universe, it exhibits complexity and behavior that keeps surprising even the most educated among us. Attempting to answer the question of the internal dynamics of protons with the use of Quantum Chromodynamics (QCD) proves to be a hard task since we are able to approximate it with a perturbative expansion only in a limited kinematic region and we are unable to carry out the calculations without the use of the perturbation theory.

Even in the perturbative region, the task is not easy and usually requires phenomenological models to deduce some observables that can be compared to an experiment. In the past, deeply inelastic scattering (DIS) has proven to be an invaluable tool for understanding the dynamics of the QCD processes governing hadrons (see Fig. 1).

In DIS, non-trivial QCD objects with internal structure (hadrons) are investigated with electrons, which are much simpler to detect and describe. Such experiments have been carried out with great success, for example at HERA experiment facility at DESY [1]. Nowadays, there is an interest in building a facility, where it would be possible to collide electrons with nuclei to probe effects known as "nuclear shadowing", "anti-shadowing","EMC" and many more.

Implementing polarization to both the electron and the target hadron beam would furthermore enable us to probe the spin puzzle of the proton. That means, to help us understand better where the spin of the proton comes from; how much of it comes from quark and gluon orbital momentum and how much from the spin of the constituent particles.

Such a facility would also allow us to probe the internal structure and serve as a "3D imaging" tool, which could give us information about the impact parameter profile of the

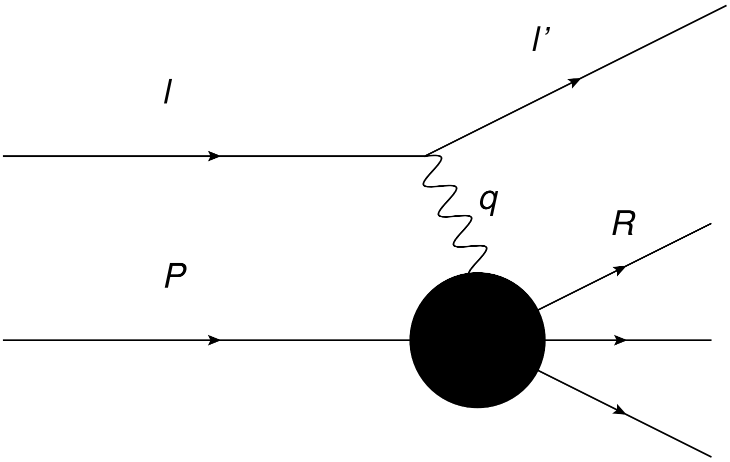

Figure 1: Schematics of DIS of an electron with momentum l of a proton with momentum P. The electron transfers the momentum q to the proton which breaks up.

proton as well as about the internal transverse momentum dynamics of the constituent partons.

There are plans for to construct such a machine in multiple countries, but my talk focused especially on those planned in the USA [2].

References

[1] Aaron, F. D. and others, JHEP 01, 109 (2010)

[2] Accardi, A. and others, Eur. Phys. J., 9 (2016)

Measurement of elliptic flow of D^0 meson in d+Au collisions at 200 GeV with the STAR experiment

Zuzana Moravcová*(zuzana.moravcova@fjfi.cvut.cz)*

Abstract

An azimuthal anisotropy of produced particles (v_2) has been observed in small-system collisions of high multiplicities. To better understand its origin, it is important to study charm quark azimuthal anisotropy in these systems. The analysis of v_2 of open charm meson D^0 in d+Au collisions at $\sqrt{s_{\mathrm{NN}}} = 200$ GeV recorded with the STAR experiment will be presented.

1 Open charm hadrons

Heavy quarks are produced at the initial stages of heavy-ion collisions. Therefore, they experience the whole evolution of the medium and can serve as probes of quark-gluon plasma, hot and dense matter of deconfined quarks and gluons. Such probe can be used to study the modification of particle production or the collective behavior of the expanding system studied via the anisotropic flow. For this reasons, open charm hadrons (D^0, $\mathrm{D}^{\pm}$, Λ_c) are extensively studied in heavy-ion collisions at the STAR experiment.

2 Anisotropic flow

After high-energy heavy-ion non-central collision, particles are pushed out of the system in a preferred direction as the overlap of colliding nuclei is anisotropic (as shown in Fig. 1). This spatial initial anisotropy is converted into momentum-space one, which is measurable. Anisotropic flow is defined by coefficients v_n in the Fourier expansion of the azimuthal dependence of the invariant yield with respect to the reaction plane:

$$E\frac{\mathrm{d}^3N}{\mathrm{d}^3p} = \frac{1}{2\pi}\frac{\mathrm{d}^2N}{p_{\mathrm{T}}\mathrm{d}p_{\mathrm{T}}\mathrm{d}y}\left(1 + \sum_{n=1}^{\infty} 2v_n \cos(n(\phi - \Psi_R))\right), \tag{1}$$

where E, p_{T}, y and ϕ are energy, transverse momentum, rapidity and azimuthal angle of particle, respectively, and Ψ_R the reaction plane defined by the impact vector and initial movement of nuclei (xz plane in Fig. 1). If the initial overlap geometry is elliptic, one can observe a significant elliptic flow v_2, and analogically for higher harmonics.

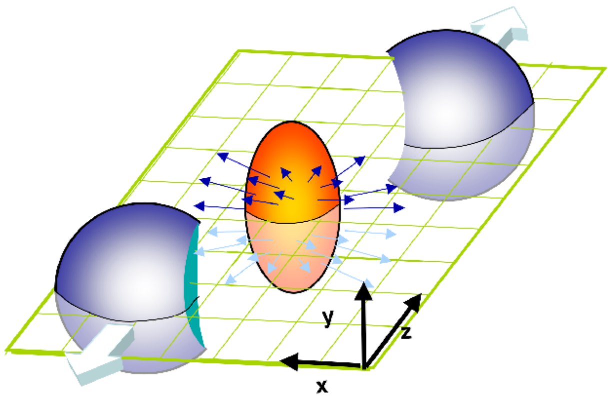

Figure 1: Heavy-ion non-central collision. Taken from [1].

One way to calculate the anisotropic flow of a particle is with the multiparticle correlation method [2]. The flow is calculated using azimuthal correlations between observed particles without the estimation of the reaction plane. A great advantage of such a method is the reduction of non-flow effects δ_n by their subtraction order by order. These effects come from correlations unrelated to the initial geometry. For instance, two-particle correlation (single-event average) can be expressed as

$$\langle \cos(n(\phi_1 - \phi_2)) \rangle = \langle e^{in(\phi_1-\phi_2)} \rangle = \langle v_n^2 \rangle + \delta_n. \tag{2}$$

After averaging over all events, one gets

$$\langle\langle 2 \rangle\rangle = \langle\langle e^{in(\phi_1-\phi_2)} \rangle\rangle := c_n\{2\}, \tag{3}$$

$$\langle\langle 4 \rangle\rangle = \langle\langle e^{in(\phi_1+\phi_2-\phi_3-\phi_4)} \rangle\rangle \tag{4}$$

for 2- and 4-particle correlation, respectively. While the second order cumulant $c_n\{2\}$ is identified to 2-particle correlation (Eq. 3), 4-particle cumulant is given by

$$c_n\{4\} := \langle\langle 4 \rangle\rangle - 2 \cdot \langle\langle 2 \rangle\rangle^2. \tag{5}$$

For the non-uniform detector acceptance, 2-particle cumulant is defined as

$$c_n\{2\} := \langle\langle 2 \rangle\rangle - \left[\langle\langle \cos n\phi_1 \rangle\rangle^2 + \langle\langle \sin n\phi_1 \rangle\rangle^2 \right]. \tag{6}$$

The independent estimation of the same order of harmonic can be obtained as

$$v_n\{2\} := \sqrt{c_n\{2\}}, \quad v_n\{4\} := \sqrt[4]{-c_n\{4\}}. \tag{7}$$

Eq. 7 characterizes the reference flow calculated from all charged hadrons that are not expected to come from decays of D^0 meson.

Additionally, one needs a differential flow of particle of interest (D^0 meson) with respect to the reference flow. Differential second order cumulant is defined as

$$d_n\{2\} := \langle\langle 2' \rangle\rangle = \langle\langle e^{in(\psi-\phi_1)} \rangle\rangle, \tag{8}$$

where ψ is the azimuthal angle of D^0 meson. We decided to do our analysis D^0 meson by D^0 meson, not event by event. For non-uniform detector acceptance, corrections analogical to Eg. 6 are applied. Finally, is is possible to estimate the differential flow of D^0 meson as

$$v'_n\{2\} = \frac{d_n\{2\}}{\sqrt{c_n\{2\}}}. \tag{9}$$

Correction on the background presence has to be applied as well.

3 D^0 meson reconstruction

The reconstruction of open charm D^0 meson was done using its hadronic decay channel ($K^{\mp}\pi^{\pm}$) using cuts on 6 different topological variables. The set of cuts was optimized with ROOT TMVA package separately for 3 different transverse momentum p_T bins. The D^0 meson was successfully reconstructed in all selected p_T bins within the hadronic decay channel in d+Au collisions at $\sqrt{s_{\mathrm{NN}}} = 200$ GeV with the STAR experiment.

The ultimate goal of this analysis is to obtain the elliptic flow of D^0 meson in d+Au collisions and compare it to results in Au+Au collisions (Fig. 2). The multiparticle correlation method will be used to fulfill this aim.

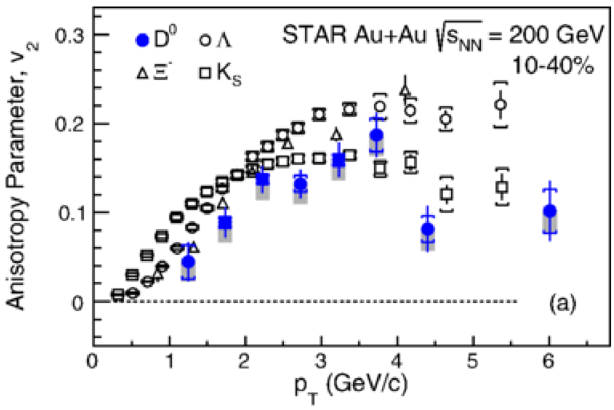

Figure 2: Elliptic flow v_2 of D^0 meson compared to other hadrons as a function of transverse momentum p_T in Au+Au collisions. Taken from [3].

References

[1] U. W. Heinz, J.Phys. A42 (2009)

[2] A. Bilandzic et al., Phys.Rev. C83 (2011)

[3] L. Adamczyk et al. (STAR collaboration), Phys. Rev. Lett. 118 (2017)

Quark-gluon plasma

Anna Mouková*(moukoann@fjfi.cvut.cz)*

1 Basic terms

At first the basic terms from the topic *Quark-gluon plasma* are defined. These terms are quark, gluon, plasma and quark-gluon plasma.

Word *quark* comes from the *Finnegans Wake* book written by James Joyce. In this book *quark* stands for a diary product. When Gell-Mann proposed the existence of up, down and strange quark, he wanted to name this fundamental partical *kwork* at first. He found this word used in sentence *Three quarks for Muster Mark!* and he has been fascinated by this analogy so much that he decided for the word *quark* using Joyce's spelling.

In 1964 Gell-Mann proposed three quarks. Later, in 1965 charm quark has been proposed and in 1975 Haim Harari added top and bottom quarks. This mean, nowadays, we have a model of 6 quarks and 6 antiquarks.

Quarks are fundamental constituents of matter and they can be found in one of 3 colour state. They formed baryons and mesons.

Gluons represent the glue that holds quarks together. They are responsible for strong interactions and have eight options of colour state.

Plasma is a one of four fundamental states of matter. The analogy with term QGP has been explained.

Quark-gluon plasma is a state of deconfined quarks and gluons which is created in central ultrarelativistic collisions and is colour-conductive.

2 Quark-gluon plasma (QGP)

2.1 Phase diagram for nuclear matter

Phase diagram for nuclear matter (Figure1) has been described with terms of hadronic matter, quark-gluon plasma and critical temperature. Hadronic matter changes into the quark-gluon plasma with high temperatures and/or densities. T_c is a critical temperature. Behind this temperature there is no hadronic matter. Until these days it has been determined as temperature somewhere between the values 0,15 and 0,20 GeV.

2.2 Probing QGP

The four ways of probing quark-gluon plasma were depicted - hadronic radiation, electromagnetic radiation, dissociation of a passing quarkonium beam and energy loss of a passing hard jet.

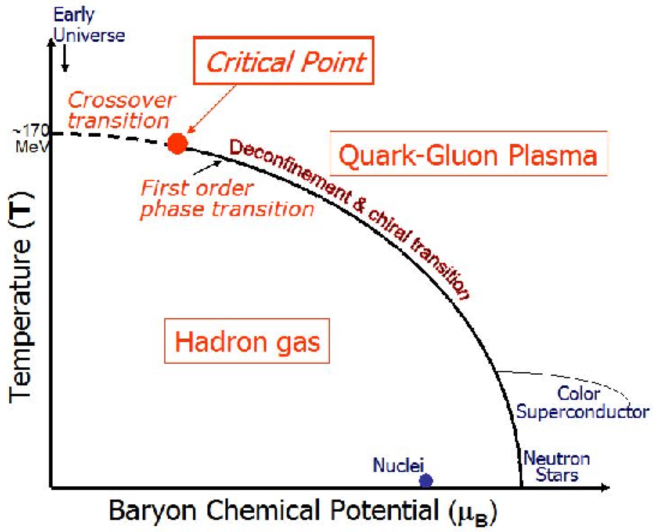

Figure 1: Phase diagram for nuclear matter.
[source: Nayak, Tapan: Search and study of Quark Gluon Plasma at the CERN-LHC (2009)]

Hadronic radiation studies the emissions of hadrons from light quarks. For early medium with very high density, the matter expands freely and flow is created. For spherical unsymmetrical initial conditions we can get through studies of hadron spectra information about earlier stages.

Electromagnetic radiation means emitting photons and dileptons. This happens in interactions of quarks and/or gluons and in anihilation of quark and antiquark pair. Because photons and dileptons interact only electromagnetically, their spectra can provide us information from early stages of matter.

Dissociation of a passing quarkonium beam can be used as a thermometer for quark-gluon plasma.

Energy loss of a passing hard jet give us some information about the density of matter it passes through.

2.3 Quantities used for describing QGP

For describing quark-gluon plasma we use mainly three important quantities which are four-momentum, rapidity and pseudorapidity. Rapidity is defined as

$$y = \frac{1}{2} \ln \left(\frac{E + p_z}{E - p_z} \right),$$

where E is energy and p_z is part of four-momentum $p = (p_0, \vec{p}_T, p_z)$.

It represents the ratio of forward and backward momentum of light-cone.

Pseudorapidity is defined as

$$\eta = \frac{1}{2} \ln \left[\frac{|\mathbf{p}| + p_z}{|\mathbf{p}| - p_z} \right]$$

and represents the emitting angle.

2.4 Geometry of a collision

Centrality of a collision is defined using impact parameter b. This b parameter can reach the values from 0 to $R_1 + R_2$, where R_1, R_2 are the diameters of collided nuclei.

For impact parameter b close to 0 we say that the collision is central. In the opposite case we call it peripheral.

2.5 Eliptic flow

Eliptic flow is something which give us an opportunity to fill the gap between statical description of quark-gluon plasma and dynamical heavy-ion collisions. The model of situation where two energetic nuclei come along the light-cone and collide is shown in Figure2. For collective flow the azimutal momentum distribution can be expanded into a

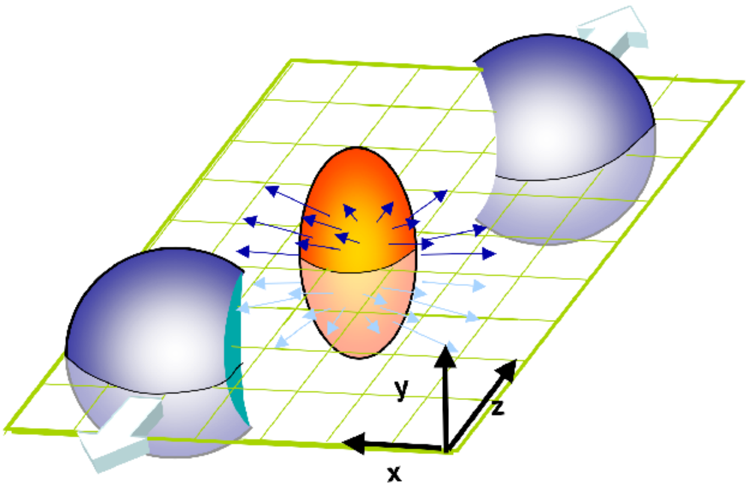

Figure 2: Collision of two energetic nuclei.
[source: Heinz, Ulrich: The Strongly coupled quark-gluon plasma created at RHIC (2009)]

Fourier series

$$\frac{dN}{d\phi} = \frac{N}{2\pi}\left[1 + 2v_1\cos(\phi) + 2v_2\cos(2\phi) + \cdots\right]$$
$$v_n = \frac{\int d\phi \cos(n\phi)\frac{dN}{d\phi}}{\int d\phi\frac{dN}{d\phi}} = \langle\cos(n\phi)\rangle ,$$

where Fourier's coeficients v_1, v_2 are called directed and eliptic flow parameters.

References

[1] Satz, H.: The Thermodynamics of Quarks and Gluons. Lect. Notes Phys. 785, 1–21 (2010)

[2] Kliemant, M. et al.: Global Properties of Nucleus–Nucleus Collisions. Lect. Notes Phys. 785, 23–103 (2010)

[3] Hirano, T. et al.: Hydrodynamics and Flow. Lect. Notes Phys. 785, 139–178 (2010)

Nonlinear time series analysis

Tomáš Novák*(novakt36@fjfi.cvut.cz)*

Nonlinear time series analysis is suited for analysis of time series obtained from deterministic dynamical system through some measurement function of phase variables. Those series have also stochastic component of different types in correlations and magnitudes. Those components are present due to noise in measurement apparatus or quantum fluctuations in more precise measurements. There are also purely stochastic time series, which have to be treated with different methods, than the ones presented here.

1 Dynamical systems

We call dynamical system the collection of phase variables $\xi_1(t), \xi_2(t), \ldots, \xi_n(t)$, which depend on external parameter t (usually time), initial conditions $\xi_1(0), \xi_2(0), \ldots, \xi_n(0)$ and evolution laws. Difference between stochastic and deterministic dynamical system is in the form of their evolution laws. Deterministic dynamical system has unambiguous evolution in contrast to stochastic one. Evolution laws for mechanical deterministic dynamical system can be identified with Hamilton's equations:

$$\begin{aligned}\dot{\xi}_1 &= f_1(t, \xi_1, \xi_2, \ldots, \xi_n),\\ \dot{\xi}_2 &= f_2(t, \xi_1, \xi_2, \ldots, \xi_n),\\ &\vdots\\ \dot{\xi}_n &= f_n(t, \xi_1, \xi_2, \ldots, \xi_n),\end{aligned} \tag{1}$$

where $\xi_k = \xi_k(\boldsymbol{x}, \boldsymbol{p})$ and $k = 1, 2, \ldots, n$, $\boldsymbol{x}$ is generalized position and $\boldsymbol{p}$ is generalized momentum.

We can distinguish between two types of deterministic dynamical systems the linear and nonlinear one. Classification is determined by the complexity of the functions $f_1, f_2, \ldots, f_n$. If all the functions f_i can be written as a linear combination of phase variables, so as $f_i = \sum_{j=1}^{n} a_{ij}\xi_j$ for $i \in \hat{n}$, we call the system linear and is easily solveable. If the functions f_i have more complicated structure, then we call those systems nonlinear. Solution $\boldsymbol{\xi}(t)$ of the system of diferential equations (1) is called phase trajectory.

2 Time series

Time series can be obtained from repeated measurements of some quantity of deterministic dynamical system. The quantity $q = q(\boldsymbol{\xi})$ is a scalar function of the phase variables and so the time series $s_1, \ldots, s_k \in \mathbb{R}$ can be generated as

$$s_l = q(\boldsymbol{\xi}(t + l\Delta t)), \tag{2}$$

where $l \in \hat{k}$ and Δt is constant time difference between consecutive elements of the time series. Function q can be also called measurement function.

2.1 Time delay vector and Taken's embedding theorem

From time series $s_1, \ldots, s_k$ we can form *time delay vector*

$$\boldsymbol{s}_n = (s_{n-(m-1)\tau}, s_{n-(m-2)\tau}, \ldots, s_{n-\tau}, s_n), \tag{3}$$

where parameters m and τ have to be choosen appropriately and are called *embedding dimension* and *time lag*, viz [1].

Floris Taken presented in 1981 embedding theorem, which states, that delay vector form as (3) is equivalent to the state vector of the deterministic dynamical system, if embedding dimension m is equal or greater than the dimension of phase space of dynamical system and measurement function q from (2) is smooth function. Proof of this theorem can be seen in [3].

2.2 Predictions

Usually we want to predict next element s_{k+1} of the time series $s_1, \ldots, s_k$ or elements further into the future $s_{k+\Delta n}$. First we need to form delay vectors $\boldsymbol{s}_1, \ldots, \boldsymbol{s}_N \in \mathbb{R}^m$. Vector $\boldsymbol{s}_N = (s_{k-(m-1)\tau}, \ldots, s_{k-\tau}, s_k)$ is last vector constructed from the time series, in $\mathbb{R}^m$ we can create epsilon neighbourhood $U_\varepsilon(\boldsymbol{s}_N)$, where ε is free parameter. Vectors from that neighbourhood are relatively similar and so we could now assume, that evolution of the time series afterwards is also similar. With this assumption we can predict element Δn into the future as

$$\hat{s}_{N+\Delta n} = \frac{1}{|U_\varepsilon(\boldsymbol{s}_N)|} \sum_{\boldsymbol{s}_l \in U_\varepsilon(\boldsymbol{s}_N)} s_{l+\Delta n}, \tag{4}$$

hat over the variable mean, that we are making an estimate, $|U_\varepsilon(\boldsymbol{s}_N)|$ is the number of vectors in neighbourhood of vector $\boldsymbol{s}_N$ and $s_{l+\Delta n}$ is the element of time series Δn steps into the future following element s_l from vector $\boldsymbol{s}_l = (s_{l-(m-1)\tau}, \ldots, s_{l-\tau}, s_l)$. So we are only averaging elements of the time series following similar delay vectors. Back to the assumption, if we remember that delay vectors are equivalent to the state vectors, then from chaos theory we know, that evolution of two state vectors from some small phase volume can diverge at maximum exponentially with af positive *Lyapunov exponent*. It is convenient to use this fact to predict elements of the time series through this method of delay vectors.

2.3 Testing stationarity

Now we have a time series as a whole and we want to test its stationarity, that means to test if the statistical properties of any two parts of the series are the same, in this manner e.g. mean, variance, autocorrelation. More or less we are testing if underlying system generating the time series is behaving the same all the time, systems parameters should not drift during generation of the time series. In our application it means, that geometrical structure of *attractor*, which is set of all possible non-ecaping trajectories of the system, does not change in time.

We can split time series $s_1, \ldots, s_k$ into sufficiently sampled segments $S_1, \ldots, S_l$. On each of the segments S_i, $i \in \hat{k}$ we form delay vectors (3) and use formula (4) to estimate $\hat{s}_p$ for each one of the element $s_p \in S_i$, the difference

$$\sigma_p = |\hat{s}_p - s_p| \tag{5}$$

called *prediction error* shows how much our prediction differs from real element. In this situation we used data from S_i to help us to predict values from S_i and we talk about *inter-sample predictions*, we *trained* our prediction (4) on data S_i. But we can use data from S_j, $j \neq i$ to predict values from S_i and look how much the difference (5) have changed, now we talk about *out-of-sample predictions.* Of course lowest prediction error is with use of inter-sample predictions, but if we are considering stationary time series than out-of-sample predictions should have not been much worse. We form *mutual prediction error graph*, one is for example on Fig. 1, where are three segments of time series each containing 10 000 values and on the x-axis we are labeling, which segments are used to train formula (4) to predict values of time series with index on y-axis and finally on x-y plate we are plotting the prediction error (5). As we would expect inter-sample predictions are as always smallest, but in this case out-of-sample predictions are significantly higher, this indicates the non-stationarity of the time series. If the out-of-sample and inter-sample predictions would be comparable, then the time series is stationary.

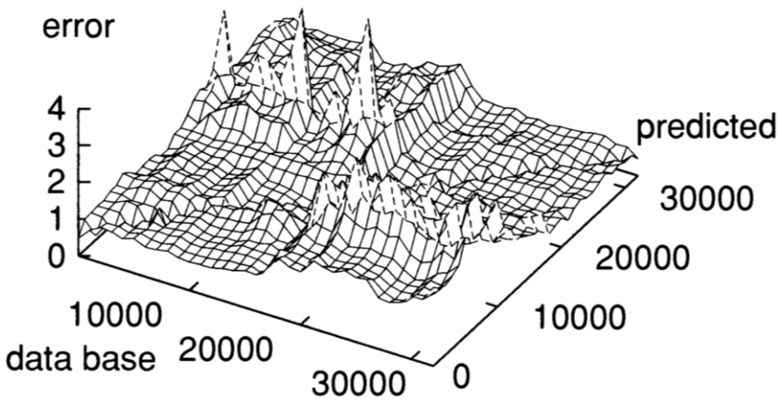

Figure 1: Mutual prediction error graph, on x-axis is data base used to train prediction (4) for components with index on y-axis, on x-y plate is the prediction error (5). [1]

References

[1] Holger Kantz, Thomas Schreiber. Nonlinear time series analysis. Cambridge University press, 359 pgs.

[2] Petr Kulhánek. Vybrané kapitoly z teoretické fyziky. 417 pgs.

[3] J.P. Huke [online]. Embedding nonlinear dynamical system: A guide to Taken's theorem. The University of Manchester, 28 pgs. [cited 27.2.2019] ¡http://barclayphysics.wikia.com/wiki/The_Electron_Gun¿

Spectroscopy and exotica of heavy flavor states in ATLAS

Radek Novotny *(novotr14@fjfi.cvut.cz)*

1 Search for the state X(5568)$\rightarrow B_s^0\pi^\pm$

The search for $X(5568) \rightarrow B_s^0\pi^\pm$ resonance, reported by the D∅ collaboration [1], was performed with the ATLAS detector [2]. The studies were made on a data sample recorded with the ATLAS detector [3] at Large Hadron Collider corresponding to the 4.9 fb^{-1} of pp collision data at $\sqrt{s} = 7$ TeV and 19.5 fb^{-1} at $\sqrt{s} = 8$ TeV.

In order to select $B_s^0\pi^\pm$ candidate, events collected with di-muon triggers were used, which are based on $J/\psi \rightarrow \mu^+\mu^-$ identification with p_{T} threshold of either 4 or 6 GeV. To reduce the background from the events with a J/ψ produced directly in pp collision, the $t > 0.2$ ps cut is applied. To form the $B_s^0\pi^\pm$ candidate, only B_s^0 events with a reconstructed mass in the signal region of $5346.6 - 5386.6$ MeV are included and combined with pion tracks forming a common PV. The detailed description of the selection cuts can be found in [2].

In order to extract physics parameters the unbinned maximum-likelihood fit with a per-candidate error was used. The signal PDF $F_{sig}(m(B_s^0\pi^\pm))$ is defined as a convolution of an S-wave Breit-Wigner(BW) distribution with a detector resolution function which is represented by a Gaussian function with a width that is calculated individually for each $B_s^0\pi^\pm$ candidate. The signal mass and width are fixed to the central values reported by the D∅ collaboration. The complex background model shape is described in [2].

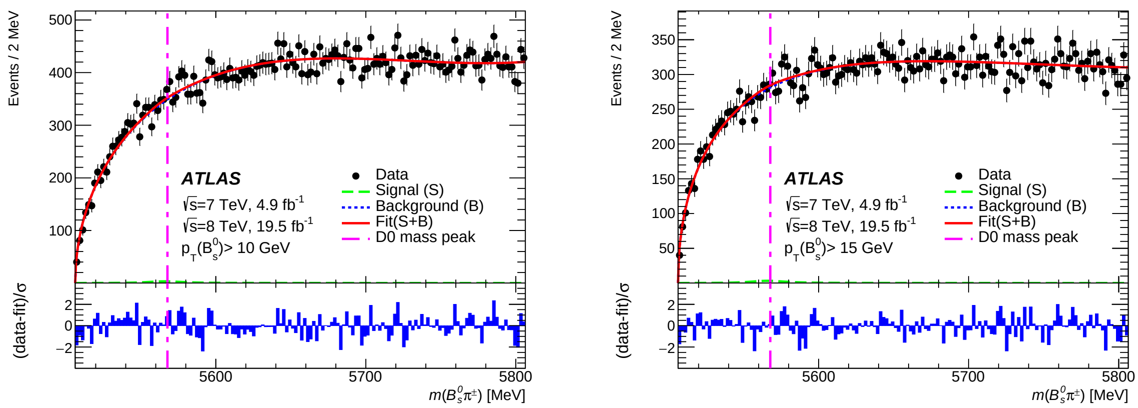

Figure 1: Results of the fit to the $B_s^0\pi^\pm$ mass distribution for candidates with $p_{\mathrm{T}}(B_s^0) > 10$ GeV (left) $p_{\mathrm{T}}(B_s^0) > 15$ GeV and (right). The bottom panels show the difference between each data point and the fit divided by the statistical uncertainty of that point [2].

The extracted values for the number of $B_s^0\pi^\pm$ candidates is $N(X) = 60 \pm 140$ for ($p_{\mathrm{T}} > 10$ GeV) and $N(X) = -30 \pm 150$ for ($p_{\mathrm{T}} > 15$ GeV) and since no significant X(5568) signal was observed, upper limits are determined for the number of $B_s^0\pi^\pm$ signal events, N(X), and for the relative production rate of the $B_s^0\pi^\pm$ and B_s^0, ρ_X.

The upper limit including systematic uncertainties is calculated using the asymptotic approximation from the profile likelihood formalism based on the $\mathrm{CL_s}$ frequentist method. The extracted upper limits at 95% C.L. are $N(X) < 382$ and $\rho_X < 0.015$ for $p_{\mathrm{T}}(B_s^0) > 10$ GeV and $N(X) < 356$ and $\rho_X < 0.016$ for $p_{\mathrm{T}}(B_s^0) > 15$ GeV, respectively.

A hypothesis test is performed for the presence of a $B_s^0\pi^\pm$ peak for every 5 MeV step in its mass from 5550 to 5700 MeV, with assumption of resonant state described by S-wave BW distribution with BW width of 21.9 MeV and $p_{\mathrm{T}}(B_s^0) > 10$ GeV. The mass dependence of resolution and ϵ^{rel} function is included as well as all systematics effects except X(5568) mass uncertainty. The results are within $\pm1\sigma$ of the background only model.

2 Excited $B_c^\pm$ Meson

The search for excited states of the $B_c^\pm$ with the ATLAS detector was performed through its hadronic transition to the ground state, with the latter detected in the decay $B_c^\pm \to J/\psi\pi^\pm$ [4]. The second S-wave state, $B_c^\pm(2S)$, is predicted to have a mass in the range of $6835 - 6917$ MeV and to have pseudoscalar (0^-) and vector (1^-) spin states that are predicted to differ in mass by about $20 - 50$ MeV.

This study uses pp collision data with $\sqrt{s} = 7$ TeV collected in 2011 and $\sqrt{s} = 8$ TeV collected in 2012 with integral luminosity of 4.9 fb^{-1} and 19.2 fb^{-1}, respectively. The performed analysis is using variable $Q = m(B_c^\pm\pi\pi) - m(B_c^\pm) - 2m(\pi^\pm)$, where $m(B_c^\pm)$ and $m(B_c^\pm\pi\pi)$ are the offline reconstructed invariant masses of selected candidates and the $m(\pi^\pm)$ is the mass of charged pion.

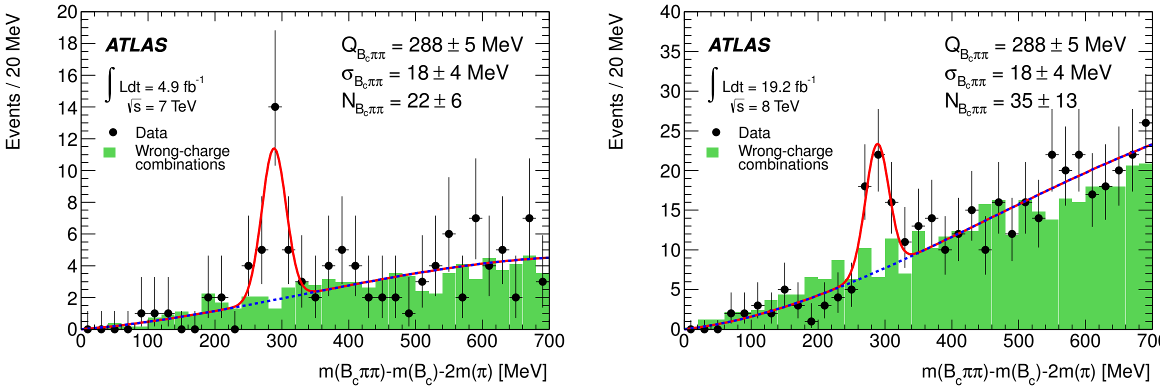

Figure 2: The distribution for the right-charge combinations (points with error bars) and for the same (wrong) pion charge combinations (shaded histogram) in 7 TeV data (left) and in 8 TeV data (right). The wrong-charge combinations are normalized to the same yield as the right-charge background. The solid line is the projection of the results of the unbinned maximum likelihood fit to all candidates in the range $0 - 700$ MeV. The dashed line is the projection of the background component of the same fit [4].

For the selected candidates, the mass difference distribution was fit using maximum likelihood fit and right-charge combinations. The wrong-charge combination were kept for the comparison with the combinatorial background shape in the right-charge combinations. The signal shape is modelled by a Gaussian function and for the background the third-order polynomial was used. The background shape resulting from the fit is verified to be consistent with the wrong-charge combinations (which are not used to constrain the model in the right-charge fit). The resulting mass difference distribution is shown in Fig. 2. The extracted parameters with statistical uncertainty only are $Q = 288.2 \pm 5.1$ MeV, yield 22 ± 6 and Gaussian width 18.2 ± 3.8 MeV for the 7 TeV data and $Q = 288.4 \pm 4.8$ MeV, yield 35 ± 13 and Gaussian width 17.0 ± 4.0 MeV for the 8 TeV data.

The significicance of the observation, acounting for "look-elsewhere effect", was established based on background only toy Monce Carlo samples. Measured significance is 3.7σ for the 7 TeV data and 4.5σ for the 8 TeV data. The significance of the combined 7 and 8 TeV dataset is 5.2σ. The local significance of the observation, obtained by fixing the mean value of the signal component, is 5.4σ.

3 Conclusion

A search for a new state $X(5568)$ decaying to $B_s^0\pi^\pm$, as reported by the D∅ collaboration, was performed by ATLAS, using 4.9 fb^{-1} of pp collision data at 7 TeV and 19.5 fb^{-1} at 8 TeV. No significant signal was found, within the analysis acceptance. The upper limits on the number of signal events $N(X)$ and on its production rate relative to B_s^0 mesons were measured. The published upper limits at 95% C.L. are $N(X) < 382$ and $\rho_X < 0.015$ for $p_{\mathrm{T}}(B_s^0) > 10$ GeV and $N(X) < 356$ and $\rho_X < 0.016$ for $p_{\mathrm{T}}(B_s^0) > 15$ GeV. The hypothesis test for X(5568) state was performed and across the full range is consistent with background only model.

A search for an excited state of the $B_c^\pm$ resonance was performed in $B_c^\pm(2S) \to B_c^\pm(1S)\pi^\pm\pi^\mp$ channel using pp collision data with 4.9 fb^{-1} at 7 TeV and 19.5 fb^{-1} at 8 TeV at the ATLAS detector. A new resonant state is observed at a mass difference of $Q = 288.3 \pm 3.5(\text{stat.}) \pm 4.1(\text{syst.})$ MeV corresponding to an invariant mass of $6842 \pm 4(\text{stat.}) \pm 5(\text{syst.})$ MeV. The significance of the observation is 5.2σ with the look elsewhere effect taken into account, and the local significance is 5.4σ. The mass of observed structure is consistent with the predicted mass of the $B_c^\pm(2S)$ with no $B_c^*(2S)$ hypothesis.

References

[1] V. M. Abazov *et al.*, "Evidence for a $B_s^0\pi^\pm$ state," *Phys. Rev. Lett.*, vol. 117, no. 2, p. 022003, 2016.

[2] ATLAS Collaboration, "Search for a Structure in the $B_s^0\pi^\pm$ Invariant Mass Spectrum with the ATLAS Experiment," *Phys. Rev. Lett.*, vol. 120, no. 20, p. 202007, 2018.

[3] ATLAS Collaboration, "The ATLAS Experiment at the CERN Large Hadron Collider," *JINST*, vol. 3, p. S08003, 2008.

[4] ATLAS Collaboration, "Observation of an Excited $B_c^\pm$ Meson State with the ATLAS Detector," *Phys. Rev. Lett.*, vol. 113, no. 21, p. 212004, 2014.

Coupling of Λ with One-Phonon Excitation of Nuclear Core

Jan Pokorný *(pokorny@ujf.cas.cz)*

1 Introduction

Hypernuclei are nuclear systems consisting of protons, neutrons and one or more hyperons – baryons with at least one s quark. Hyperons decay predominantly through weak interaction which results in their rather long lifetime ($\tau \approx 10^{-10}$ s) compared to the time scale of the strong interaction ($\approx 10^{-23}$ s). This allows for experimental study of hypernuclei, their spectra and structure. Moreover, hyperon bound in the hypernucleus is not affected by the Pauli exclusion principle of nucleons and therefore serves as a unique probe of the nuclear interior. The study of hypernuclei contributes to our better understanding of nuclear forces, as well as nuclear structure and dynamics.

Hypernuclei were discovered in 1952 by Jerzy Pniewski and Maryan Danysz who studied interactions of high-energy cosmic rays with a nucleus in nuclear emulsion [1]. Numerous hypernuclear species have been later observed in experiments with nuclear emulsion exposed to proton, pion, or kaon beams. The data from these types of experiments were rather limited. The developement of the counter experiments has lead to major breakthrough in hypernuclear physics. The number of observed species has doubled and the precision of their measured spectra has improved. Hypernuclei have been studied by many collaborations around the world (CERN, BNL, KEK, FINUDA, JLab, JPARC, GSI, MAMI-C [2, 3, 4, 5, 6]).

2 Mean-Field Model of Hypernuclei

The strucutre of medium-mass and heavy hypernuclei has been studied within several models, based mostly on phenomenological potentials. We mention the Skyrme Hartree-Fock model [7, 8, 9] and the relativistic mean-field (RMF) model [10, 11].

We work on a project whose goal is to provide an *ab initio* description of medium-mass and heavy hypernuclei starting from most modern realistic nucleon-nucleon and baryon-baryon potentials and to study complex many-body configurations. This goal will be achieved by adopting the Equation of Motion Phonon Method (EMPM). This method has been developed for studies of nuclear structure [12] and it has been used for light and heavy even-even [13, 14, 15, 16] and medium-mass odd-even nuclei [17, 18, 19].

The first step of our approach is to develop the Hartree-Fock (HF) method in the proton-neutron-Λ (p-n-Λ) formalism and the nucleon-Λ Tamm-Dancoff Approximation (NΛ TDA). The HF works well for description of hypernuclei with one Λ particle bound to an even-even nuclear core, while the NΛ TDA allows for study of hypernuclear systems with one Λ coupled to an odd-even core [20].

3 Theoretical Formalism

We start with the hypernuclear Hamiltonian

$$\widehat{H} = \widehat{T}^N + \widehat{T}^\Lambda + \widehat{V}^{NN} + \widehat{V}^{NNN} + \widehat{V}^{N\Lambda} - \widehat{T}_{CM}, \tag{1}$$

where $\widehat{T}^N$ and $\widehat{T}^\Lambda$ is the kinetic energy operator of nucleons and Λ, respectively, $\widehat{T}_{CM}$ is the centre-of-mass kinetic operator, and $\widehat{V}^{NN}$, $\widehat{V}^{N\Lambda}$, and $\widehat{V}^{NNN}$ stand for the 2-body NN, the $N\Lambda$, and the 3-body NNN potentials, respectively.

The HF equations are

$$\begin{aligned} t^{\mathrm{p}}_{ij} + \sum_{kl} V^{\mathrm{pp}}_{ikjl}\rho^{\mathrm{p}}_{lk} + \sum_{kl} V^{\mathrm{pn}}_{ikjl}\rho^{\mathrm{n}}_{lk} + \sum_{kl} V^{\mathrm{p}\Lambda}_{ikjl}\rho^{\Lambda}_{lk} + \frac{1}{2}\sum_{klmn} V^{\mathrm{ppp}}_{ikljmn}\rho^{\mathrm{p}}_{mk}\rho^{\mathrm{p}}_{nl} \\ + \frac{1}{2}\sum_{klmn} V^{\mathrm{pnn}}_{ikljmn}\rho^{\mathrm{n}}_{mk}\rho^{\mathrm{n}}_{nl} + \sum_{klmn} V^{\mathrm{ppn}}_{ikljmn}\rho^{\mathrm{p}}_{mk}\rho^{\mathrm{n}}_{nl} = \varepsilon^{\mathrm{p}}_i \delta_{ij}, \end{aligned} \tag{2}$$

$$\begin{aligned} t^{\mathrm{n}}_{ij} + \sum_{kl} V^{\mathrm{nn}}_{ikjl}\rho^{\mathrm{n}}_{lk} + \sum_{kl} V^{\mathrm{pn}}_{kilj}\rho^{\mathrm{p}}_{lk} + \sum_{kl} V^{\mathrm{n}\Lambda}_{ikjl}\rho^{\Lambda}_{lk} + \frac{1}{2}\sum_{klmn} V^{\mathrm{nnn}}_{ikljmn}\rho^{\mathrm{n}}_{mk}\rho^{\mathrm{n}}_{nl} \\ + \frac{1}{2}\sum_{klmn} V^{\mathrm{ppn}}_{klimnj}\rho^{\mathrm{p}}_{mk}\rho^{\mathrm{p}}_{nl} + \sum_{klmn} V^{\mathrm{pnn}}_{klimnj}\rho^{\mathrm{p}}_{mk}\rho^{\mathrm{n}}_{nl} = \varepsilon^{\mathrm{n}}_i \delta_{ij}, \end{aligned} \tag{3}$$

$$t^{\Lambda}_{ij} + \sum_{kl} V^{\mathrm{p}\Lambda}_{kilj}\rho^{\mathrm{p}}_{lk} + \sum_{kl} V^{\mathrm{n}\Lambda}_{kilj}\rho^{\mathrm{n}}_{lk} = \varepsilon^{\Lambda}_i \delta_{ij}, \tag{4}$$

where ρ^{p}_{nm}, ρ^{n}_{nm} and ρ^{Λ}_{nm} are the density matrices for protons, neutrons and Λ, respectively.

The solution of the HF equations gives the single-particle energies $\varepsilon^{\mathrm{p}}_i$, $\varepsilon^{\mathrm{n}}_i$ of the nucleons and yields the energies ε^{Λ}_i of the Λ hyperon bound to the even-even nuclear core [20].

The energy spectra of hypernuclei consisting of one Λ coupled to an odd-even nuclear cores are determined by solving the NΛ TDA eigenvalue equations. To this purpose we solve separately the HF Eqs. (2-3) for the nucleons of the core and the Eq. (4) for Λ. The energies and basis states so obtained enter the NΛ TDA eigenvalue equations

$$\sum_{ph} \left((\varepsilon^{\Lambda}_p - \varepsilon^{\mathrm{p}}_h)\delta_{pp'}\delta_{hh'} - V^{\mathrm{p}\Lambda}_{\bar{h}p'\bar{h}'p} \right) r^{\mu,\mathrm{p}\Lambda}_{ph} = (E^{\mathrm{p}\Lambda}_{\nu} - E_{\mathrm{HF}}) r^{\mu,\mathrm{p}\Lambda}_{p'h'}, \tag{5}$$

$$\sum_{ph} \left((\varepsilon^{\Lambda}_p - \varepsilon^{\mathrm{n}}_h)\delta_{pp'}\delta_{hh'} - V^{\mathrm{n}\Lambda}_{\bar{h}p'\bar{h}'p} \right) r^{\mu,\mathrm{n}\Lambda}_{ph} = (E^{\mathrm{n}\Lambda}_{\nu} - E_{\mathrm{HF}}) r^{\mu,\mathrm{n}\Lambda}_{p'h'}. \tag{6}$$

4 Conclusions

We developed the HF method and the NΛ TDA method to study the properties of medium-mass and heavy hypernuclei. The HF method is suitable for studying systems with even-even core and one bound Λ particle. The NΛ TDA method is used for calculating energy spectra of hypernuclei with even-odd core and one Λ particle.

In order to obtain better results of nuclear binding energies, it is necessary to include more complex nuclear configurations. This will be achieved by implementing the EMPM.

The method derives and solves iteratively a set of equations of motion to generate an orthonormal basis of multiphonon states built of TDA phonons. Such a basis simplifies the structure of the Hamiltonian matrix and makes feasible its diagonalization in large configuration and phonon spaces. The diagonalization of the Hamiltonian in the multiphonon space so constructed produces highly correlated states, including the ground state. It takes into full account the Pauli principle, and holds for any Hamiltonian.

We extend the method to hypernuclei with even-even and odd-even cores. In these two cases we couple, respectively, the Λ states and the NΛ TDA phonons to the many particle-hole excitations of the nuclear cores.

Another important issue is the inclusion of the $\Lambda - \Sigma$ mixing in the YN LO interaction. We plan to include the $N\Lambda - N\Sigma$ part of the chiral LO YN interaction into the $N\Lambda - N\Lambda$ channel through the SRG transformation. Such a transformation has the effect of suppressing the $\Lambda - \Sigma$ mixing terms and generating thereby a 3-body YNN force to be added to the SRG transformed 2-body YN potential [21].

References

[1] M. Danysz, J. Pniewski, Phil. Mag. **44**, 348 (1953).

[2] O. Hashimoto, H. Tamura, Prog. in Part. and Nucl. Phys. **57**, 564 (2006).

[3] H. Tamura, M. Ukai, T. O. Yamamoto, T. Koike, Nucl. Phys. A **881**, 310 (2012).

[4] M. Agnello et al. (The FINUDA Collaboration), Phys. Lett. B **622**, 35 (2005).

[5] T. R. Saito et al., Nucl. Phys. A **754**, 3c (2004).

[6] P. Achenbach et al. (A1 Collaboration), Int. J. Mod. Phys. E **19**, 2624 (2004).

[7] H.-J. Schulze, E. Hiyama, Phys. Rev. C **90**, 047301 (2014).

[8] M. Rayet, Nucl. Phys. A **367**, 381 (1981).

[9] D. E. Lanskoy, Y. Yamamoto, Phys. Rev. C **55**, 2330 (1997).

[10] J. Mareš, B. K. Jennings, Nucl. Phys. A **585**, 347 (1995).

[11] B.-N. Lu, E. Hiyama, H. Sagawa, S.-G. Zhou, Phys. Rev. C **89**, 044307 (2014).

[12] D. Bianco, F. Knapp, N. Lo Iudice, F. Andreozzi, A. Porrino, Phys. Rev. C **85**, 014313 (2012).

[13] F. Knapp, N. Lo Iudice, P. Veselý, F. Andreozzi, G. De Gregorio, A. Porrino, Phys. Rev. C **90**, 014310 (2014).

[14] F. Knapp, N. Lo Iudice, P. Veselý, F. Andreozzi, G. De Gregorio, A. Porrino, Phys. Rev. C **92**, 054315 (2015).

[15] G. De Gregorio, F. Knapp, N. Lo Iudice, P. Veselý, Phys. Rev. C **93**, 044314 (2016).

[16] G. De Gregorio, F. Knapp, N. Lo Iudice, P. Veselý, Physica Scripta **92**, 074003 (2017).

[17] G. De Gregorio, F. Knapp, N. Lo Iudice, P. Veselý, Phys. Rev. C **94**, 061301(R) (2016).

[18] G. De Gregorio, F. Knapp, N. Lo Iudice, P. Veselý, Phys. Rev. C **95**, 034327 (2017).

[19] G. De Gregorio, F. Knapp, N. Lo Iudice, P. Veselý, Phys. Rev. C **97**, 034311 (2018).

[20] P. Veselý, G. De Gregorio, J. Pokorný, Phys. Scr. **94**, 014006 (2019).

[21] R. Wirth, R. Roth, *Phys. Rev. Lett.* **117**, 182501 (2016).

Object Detection for Jet Physics

Georgij Ponimatkin*(ponimgeo@fjfi.cvut.cz)*

1 Introduction

In recent years we've seen a significant progress in the computer vision, mainly powered by the recent surge of deep learning [1], large datasets [2] and easy access to fast computational resources. In order to use those advancements for physics a paradigm of "jet images" was created [3, 4]. This technique was shown to be highly successful for the task of boosted object tagging [3, 4], quark vs. gluon jet discrimination [5], etc. Usually, those techniques rely on classification, taking single image as an input (usually a jet) and providing its class in the output (type of a jet). But working with one image may be limiting for some applications. In computer vision there are more advanced techniques, namely object detection and instance segmentation methods, that allow to extract much more information from the single image, by finding location of an object in an image (via bounding boxes), its class and in the case of instance segmentation also exact pixel mask around this image. One well known example of such algorithm is the Mask R-CNN [6]. Thus it is of particular interest, whether object detection methods can be of use for jet physics. In this paper we will investigate first efforts towards application of the Mask R-CNN for the task of jet identification in calorimeter read-out.

2 Data Sample

We use Pythia8 [7, 8] Monte-Carlo (MC) generator in order to generate training dataset for the center of mass energy $\sqrt{s} = 200$ GeV pp system, simulating calorimeter-like read-out of collision in (η, ϕ, p_T) space, where η is pseudo-rapidity, φ azimuthal angle and p_T is a transverse momentum of a particle. Pythia8 was set with `HardQCD:all = on`, `SoftQCD:nonDiffractive = on` flags in order to simulate hard physics in presence of soft background. The `PhaseSpace:pTHatMin` and `PhaseSpace:pTHatMax` flags were set such that the total jet p_T spectrum is flat for training and validation datasets, for test dataset we use `PhaseSpace:pTHatMin = 3`. Jets were clustered using the anti-k_t algorithm [9] implemented in `FastJet` [10] package. We've generated $1,000,000/250,000/250,000$ training/test/validation events in total.

3 Model training and evaluation

In our experiments we've used the Mask R-CNN implementation by Matterport [11], which was trained from scratch. After training, we've evaluated the model using a sim-

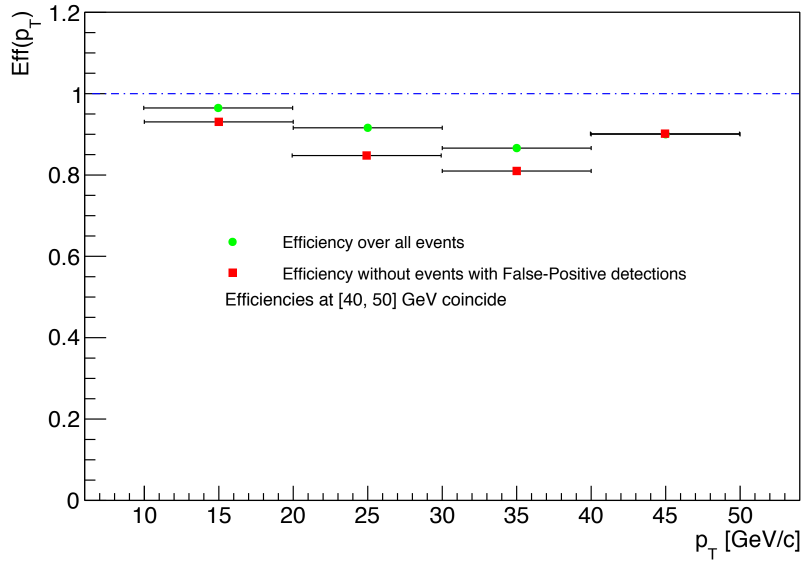

Figure 1: Efficiency of the Mask R-CNN calculated over all events (circles), over events without false-positive detections (squares). Efficiencies at $[40, 50]$ GeV/c coincide.

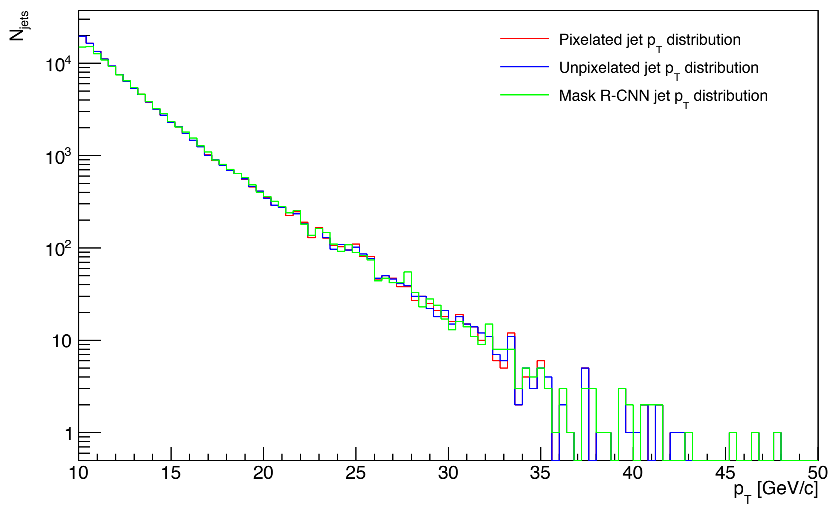

Figure 2: Jet p_T distributions from simulations with pixelization (red), without pixelization (blue) and as reconstructed by Mask R-CNN (green).

plified jet-matching technique:

- We take predicted jet and find the closest ground-truth jet.
- We require at least 25% overlap between bounding boxes of the ground-truth jet and the predicted jet.

During evaluation we've found out that the model is plagued by false-positive detection rate of $\sim 5\%$, hence we provide two evaluations - one where we calculate efficiency over all events, another one where we consider events with false-positive detection to be completely wrong. Those efficiencies as a function of p_T can be seen in Fig. 1. In Fig. 2 we can see jet p_T spectrum as it is reconstructed by Mask R-CNN in comparison to ground-truth distributions.

4 Conclusion

In this paper we present the first results concerning applications of the Mask R-CNN towards detection of jets in calorimeter read-outs. Our results indicate that this approach has relatively high efficiency in jet identification as well as high precision in jet p_T spectrum reconstruction. Further on we would like to add complexity into the system in order to explore how the algorithm would work in ultrarelativistic heavy-ion collision regime, where strong backgrounds are expected.

5 Acknowledgments

Author would like to acknowledge Jana Bielčíková and Josef Šivic for their mentoring during the course of this project.

References

[1] A. Krizhevsky, I. Sutskever, and G. E. Hinton *Commun. ACM*, vol. 60, pp. 84–90, May 2017.

[2] O. Russakovsky, J. Deng, H. Su, J. Krause, S. Satheesh, S. Ma, Z. Huang, A. Karpathy, A. Khosla, M. Bernstein, A. C. Berg, and L. Fei-Fei *International Journal of Computer Vision*, vol. 115, pp. 211–252, Dec 2015.

[3] J. Cogan, M. Kagan, E. Strauss, and A. Schwarztman *Journal of High Energy Physics*, vol. 2015, p. 118, Feb 2015.

[4] L. de Oliveira, M. Kagan, L. Mackey, B. Nachman, and A. Schwartzman *Journal of High Energy Physics*, vol. 2016, p. 69, Jul 2016.

[5] P. T. Komiske, E. M. Metodiev, and M. D. Schwartz *Journal of High Energy Physics*, vol. 2017, p. 110, Jan 2017.

[6] K. He, G. Gkioxari, P. Dollár, and R. Girshick in *2017 IEEE International Conference on Computer Vision (ICCV)*, pp. 2980–2988, Oct 2017.

[7] T. Sjöstrand, S. Mrenna, and P. Skands *Journal of High Energy Physics*, vol. 2006, pp. 026–026, may 2006.

[8] T. Sjostrand, S. Mrenna, and P. Z. Skands *Comput. Phys. Commun.*, vol. 178, pp. 852–867, 2008.

[9] M. Cacciari, G. P. Salam, and G. Soyez *Journal of High Energy Physics*, vol. 2008, pp. 063–063, apr 2008.

[10] M. Cacciari, G. P. Salam, and G. Soyez *The European Physical Journal C*, vol. 72, p. 1896, Mar 2012.

[11] W. Abdulla. `https://github.com/matterport/Mask_RCNN`, 2017.

Performance characterisation of ALPIDE after 2.7 Mrad proton irradiation at NPI

Valentina Raskina*(raskival@fjfi.cvut.cz)*

1 Introduction

ALICE (A Large Ion Collider Experiment)[1] is a high–energy physics detector at the CERN Large Hadron Collider (LHC). Run 3 is a new period of data taking in which ALICE aims to perform detailed measurements of Quark Gluon Plasma (QGP). ALICE also expects that in Run 3, the LHC will deliver 100 times higher luminosity with respect to previous data taking periods. To be able to accomplish the physics program planned for Run 3, ALICE will undergo an upgrade during the Second Long LHC shutdown (LS2) in 2019–2020. The ALICE upgrade program includes many sub-projects, one of the most important is the upgrade of the ALICE Inner Tracking System (ITS). The main goals of the ITS upgrade are: to improve impact parameter resolution of reconstructed tracks, to improve tracking efficiency and p_{T} resolution at low p_{T}, to increase readout rate and to allow fast insertion and removal of the detector during the end of year technical stops. Comparing to the old ITS which has 6 cylindrical layers of of silicon pixel, drift and strip detectors, the new ITS will have 7 layers of pixel sensors ALPIDE.

2 The ALPIDE

The basic unit of the new ITS is ALPIDE, which stands for ALice PIxel DEtector. This is a silicon sensor with a size of 1.5 cm $\times$ 3 cm, which is divided into 512 rows and 1024 columns of pixels with a pitch of 29.24 μm $\times$ 26.88 μm. The ALPIDE is a MAPS which uses the 180 nm CMOS technology of TowerJazz. This technology allows to use high-resistivity epitaxial layer and deep p-well, see Fig. 1. The thickness of sensitive layer is 18 – 30 μm. Since ALPIDE is a MAPS each pixel thus contains both the sensitive layer and the front-end electronics. There are several 8-bit DACs on the periphery of the chip, which regulate currents and voltages in the front-end circuits of pixels. The most important DACs are I_{THR} and V_{CASN}, which control Threshold. The ALPIDE performance fulfils all the project design requirements such as thickness, spatial resolution, detection efficiency, fake–hit rate, TID, NIEL radiation tolerance and etc.

In Run 3 the expected total ionising dose for the chip in the Inner Barrel is 270 krad and the non-ionising energy loss is 1.3×10^{12} 1MeV $\mathrm{n_{eq}cm^{-2}}$. However the project requires

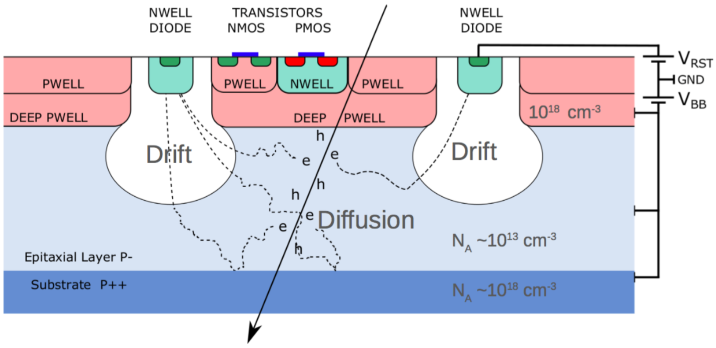

Figure 1: Schematic drawing of a pixel of ALPIDE MAPS sensor with TowerJazz technology, taken from [2]

the safety factor of 10 for radiation loads for the innermost layers of ITS. That is why it is needed to study whether the chip will sustain the project limits on radiation hardness.

3 Radiation Hardness Tests

Radiation hardness of the ALPIDE was tested by ALICE group in the Nuclear Physics Institute (NPI) of the Czech Academy of Sciences (CAS). For this purpose we used proton beam with an energy of 35 MeV provided U-120M cyclotron of the NPI of CAS in Řež, which was monitored during the whole irradiation by the ionisation chamber. The irradiation process goes in the following way: we periodically interrupt the beam using the beam stop plate. When the beam stop is opened the chip is irradiated. When the beam stop is in the beam, the irradiation is interrupted and we perform the Threshold and DACs' scans.

The dependence of the absorbed total ionisation dose and fluence on time for different irradiation campaigns is in the Figure 2, left. Irradiation campaigns took place every month since September of 2016. The growing trend in the curves corresponds to the irradiation and the flat trend corresponds to the period when the ALPIDE is not irradiated.

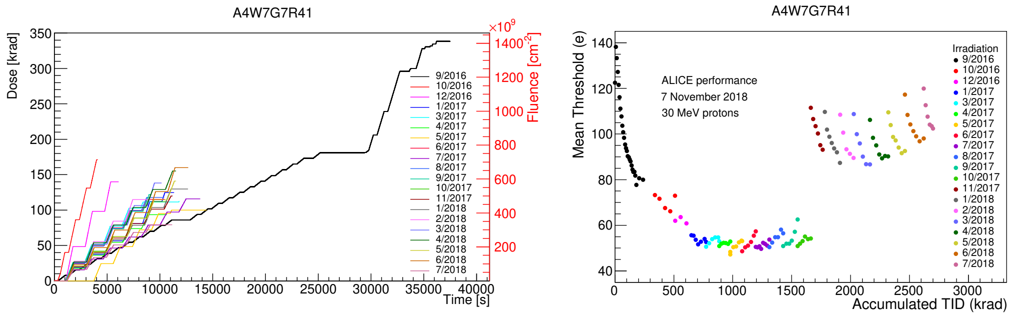

Figure 2: To the left: Total ionisation dose and accumulated fluence for different irradiation campaigns. To the right: Mean threshold vs. accumulated dose.

In case of ALPIDE, the charge threshold is the quantity of deposited charge, which is registered by pixels with 50 % probability. In ALPIDE sensor charge threshold is depend mainly on 2 DACs: I_{THR} and V_{CASN}. In Figure 2 to the right, the dependence of the mean threshold on the accumulated dose for different irradiation campaigns marked by different colours is presented.

Initially we run the default ALPIDE threshold settings. So the mean threshold was decreasing with the accumulated dose without any sign of annealing, which is the ability of silicon sensors to auto recover. In October 2017, the chip was already too noisy so we have increased the threshold by changing DAC settings. Since then we observe the annealing of the chip from campaign to campaign.

4 Results

After obtaining the total ionizing dose of 2700 krad, the chip was sent for characterisation to CERN Proton Synchrotron. There the ALPIDE was tested using the 6 GeV pion beam.

Figure 3 shows the detection efficiency and the fake hit rate versus threshold for our irradiated chip and for a non-irradiated sensor. As it is seen from plot, the irradiated sensor still fulfils the requirements of the upgrade project in terms of detection efficiency and fake hit rate.

In the range of thresholds between 150–200 electrons, we see that red data are below the project limit and black data are above the limit.

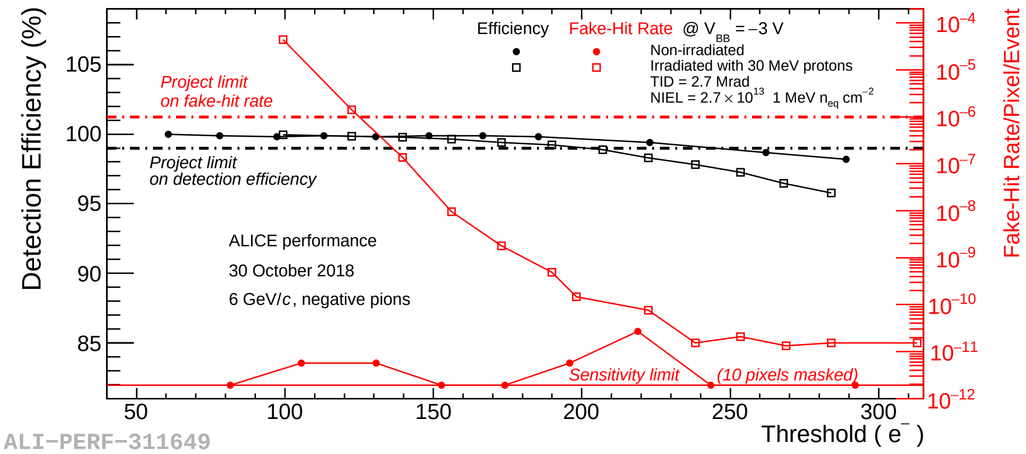

Figure 3: Detection efficiency and fake-hit rate vs. threshold.

References

[1] ALICE Collaboration, K. Aamodt et al., *The ALICE experiment at the CERN LHC*, JINST 3 (2008) S08002.

[2] Mónika Varga-Kőfaragó, *Anomalous Broadening of Jet-Peak Shapes in Pb–Pb Collisions and Characterization of Monolithic Active Pixel Sensors for the ALICE Inner Tracking System Upgrade*, CERN-Thesis, 2018.

[3] ALICE, *Letter of intent*, J.Phys. G41 (2014) 087001.

Study of jet substructure in heavy-ion collisions

Monika Robotková*(robotmon@fjfi.cvut.cz)*

1 Introduction

Jets are a good probe to study a hot and dense matter of partons called quark-gluon plasma (QGP). Up to now, jets have been viewed primarily in terms of their inclusive properties, but in recent years the study has also shifted to differential properties that focus on the substructure of the jets. The jet substructure modification can be investigated with several observables, but this study deals in detail mainly with z_g - *the jet splitting function.*

The jet is a collimated spray of hadrons, created during hadronization of a quark or gluon after hard scattering. During the QGP formation a phenomenon called "jet quenching" can occur, when constituents of the parton shower can lose energy due to medium-induced gluon radiation or elastic scattering which leads to the formation of lower-energy jets. Jets are defined via algorithms. Currently used are sequential recombination algorithms - k_T, anti-k_T and Cambridge/Aachen (C/A) [1].

2 Study of jet substructure

The study of jet substructure can provide new insight into medium induced effects during the parton shower evolution in the QGP. We use clustering history to select some parts of the particle shower using jet clustering techniques [2], for example SoftDrop [3].

SoftDrop is a grooming technique used to remove wide-angle soft radiation from a clustered jet. The soft drop declustering considers a jet defined with the anti-k_t algorithm, which is then reclustered using the C/A algorithm. From this reclustering we obtain an angular-ordered clustering tree. Then we get two subjets (j_1 and j_2) from the jet j by undoing the last stage of the C/A clustering. If these subjets pass the condition

$$\frac{\min(p_{T,1}, p_{T,2})}{p_{T,1} + p_{T,2}} > z_{cut} \left(\frac{\Delta R_{12}}{R_0} \right)^{\beta}, \tag{1}$$

where z_{cut} is a soft threshold, β an angular exponent, $p_{T,i}$ transverse momenta of the constituents, ΔR_{12} their distance and R_0 the jet radius, the jet j is the final soft-drop jet. Otherwise, we take the subjet with a higher p_T and iterate the procedure. *The jet splitting function* or *shared momentum fraction* is an observable characterizing the parton splitting. It is defined as the ratio between transverse momenta of the less energetic subjet

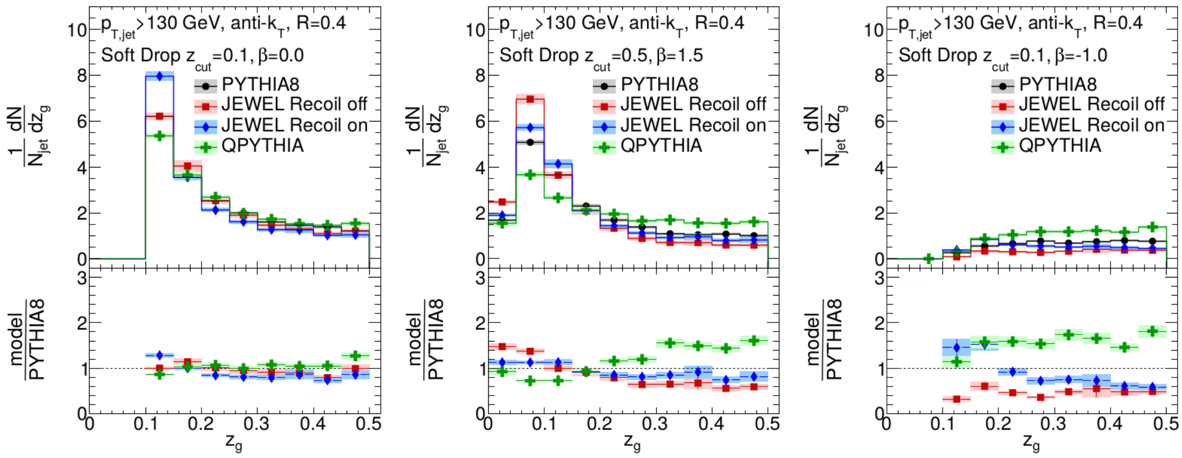

Figure 1: Groomed shared momentum fraction, z_g, for three different grooming settings in simulations with and without jet quenching at $\sqrt{s_{NN}} = 5.02$ TeV [4].

and sum of the two subjets from the soft drop condition (Eq. 1). Then we obtain an equation

$$z_g \equiv \frac{\min(p_{T,1}, p_{T,2})}{p_{T,1} + p_{T,2}}. \tag{2}$$

The measurement of the z_g reflects the role of color coherence of the jet in the QGP. If the partons produced in the first splitting act as a single coherent emitter, z_g will be unaffected. The z_g will be modified only if the partons act as decoherent emitters.

Fig. 1 shows the z_g distribution for different event generators and different values of the parameters β and z_{cut}. We note that JEWEL [5] jets are collimated and therefore less jets are surviving the grooming, in contrast to QPYTHIA [6], which makes the jets broader, more jets survive. We can also see changes for different values of the parameter β, especially for $\beta < 0$, where a large deviation from unity is observed.

3 Results

Recent results of the z_g measurement from STAR [7] are plotted in Fig. 2. The ratios of z_g between Au+Au data and p+p for trigger and recoil jets do not display any significant modification. A possible reason may be that the hardest split occurs mostly outside of the medium or the selection is dominated by unmodified jets.

The CMS collaboration published results from 2015, where the modification of z_g in the region $140 < p_{T,Jet} < 160$ GeV/c is observed. The ratio of the z_g distribution in Pb+Pb and p+p collisions at $\sqrt{s_{NN}} = 5.02$ TeV for different $p_{T,Jet}$ is plotted in Fig. 3.

References

[1] M. Cacciari, G. P. Salam, G. Soyez, Eur. Phys. J. C72 (2012) 1896.

[2] A. M. Sirunyan et al. [CMS Collaboration], Phys. Rev. Lett. 120, no. 14, 142302 (2018).

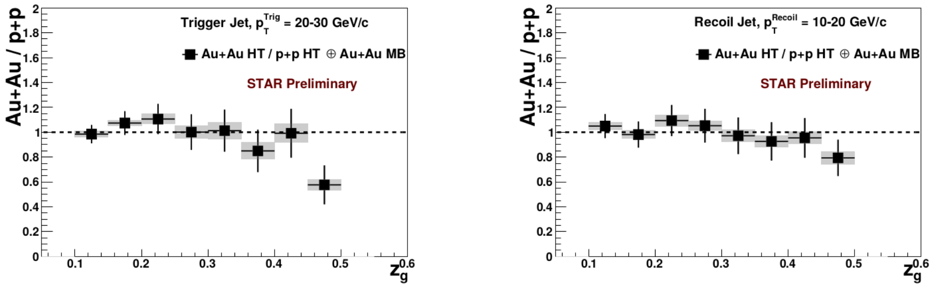

Figure 2: The ratio of the z_g distribution between Au+Au data and p+p data at $\sqrt{s_{NN}} =$ 200 GeV for trigger and recoil jets [7].

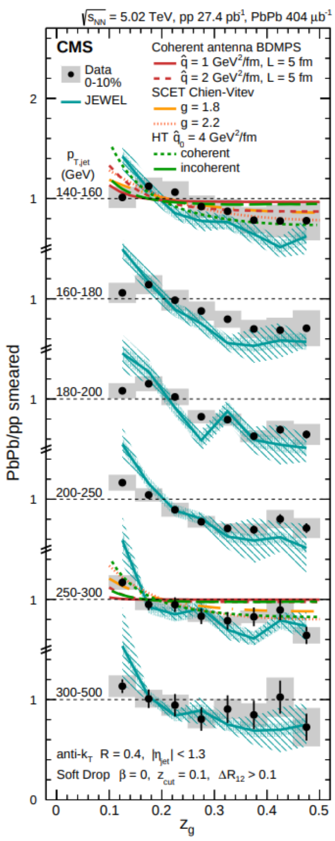

Figure 3: Ratios of z_g distributions in Pb+Pb and smeared p+p collisions in most central events at $\sqrt{s_{NN}} = 5.02$ TeV, for several $p_{T,jet}$ ranges [2].

[3] A. J. Larkoski, S. Marzani, G. Soyez and J. Thaler, JHEP 1405, 146 (2014).

[4] H. A. Andrews et al., CERN-TH-2018-186.

[5] K. C. Zapp, Eur. Phys. J. C74 (2) (2014) 2762.

[6] N. Armesto, L. Cunqueiro, C. A. Salgado, Eur. Phys. J. C63 (2009) 679–690.

[7] K. Kauder [STAR Collaboration], Nucl. Part. Phys. Proc. 289-290, 137 (2017).

Bunch by bunch intensity measurements

Sedláček Ondřej *(Ondrej.Sedlacek@fjfi.cvut.cz)*

1 Intensity measurements

Intensity measurements are very important as they measure number of particles in each bunch. There exist several types of intensity measurements, namely Integral intensity measurements are often used [3]. However integral intensity measurements integrate the intensity of the beam and then average it. Therefore the outcome of such a measurement has no information about the variation of intensity of each bunch[1].

Per Bunch intensity measurements are sensitive to the variation of intensity of each bunch as each bunch is measured separately.

2 Bunch by bunch intensity measurements at CERN

2.1 Signal deconvolution

The bunch intensity measurements for LHC and SPS was designed to fulfill 1% and 5% precision, respectively [1]. To achieve better measurement precision the signal needs to be deconvoluted since the signal overlaps between the adjacent bunches. Simulation shown in 1.

The correcting algorithm was created based on an analysis and simulation of the signal leakage and implemented into the data processing FPGA of the measurement system. Thanks to this deconvolution the errors should be well below the designed precision.

2.2 Single shot bunch by bunch intensity measurements for Transfer lines

The generalization of the bunch by bunch intensity measurements for the single shot bunch by bunch intensity measurements for the transfer lines is considered.

The proposed measurements suffer from error of different sampling phase because the beam travel trough the transfer lines (and the measurement spot) only once. Therefore the analysis of the precision of such measurements for different ADCs was carried out, to study feasibility and sustainable precision.

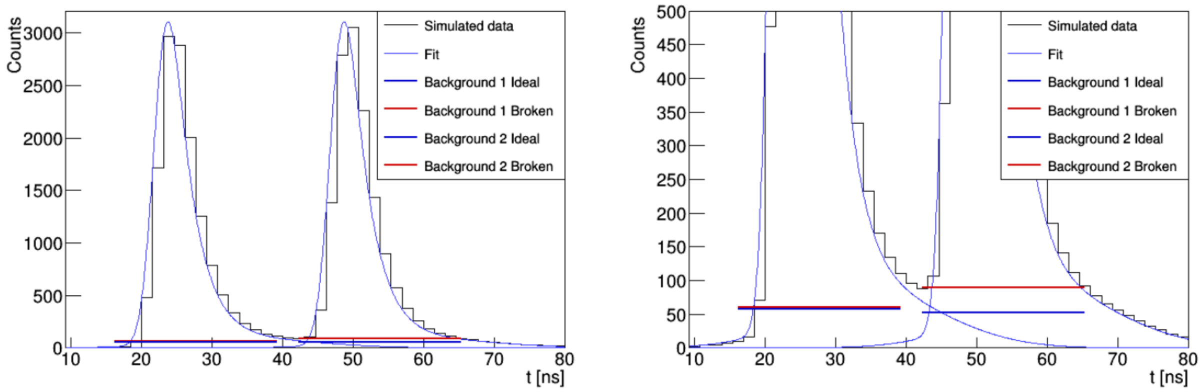

Figure 1: Both figures represent two simulated signals with 25 ns spacing, the right figure shows the magnified tail region where the differences are important. Ideal (dark blue) and broken (red) baseline is presented and calculated as the average of the first and the last sample used of ideal and broken signal respectively.

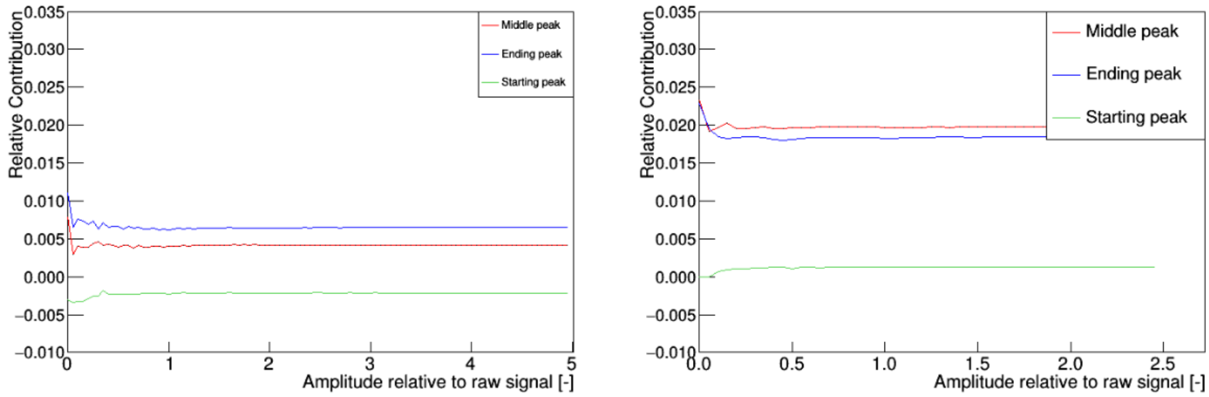

Figure 2: Comparison of amplitude dependence of relative contribution with (left) and without (right) correcting algorithm use. The relative contribution is an integral of a broken signal divided by ideal signal minus one.

2.3 Wrong bucket injection

The injection scheme of LHC beam is 1/10, meaning that every 10th bucket is filled with the bunch [2]. Therefore there is ≈25ns between every bunch. It is essential to abide this scheme as many measurements count on the distance to be ≈25ns. In the past wrong bucket injection happened twice and cost at least 6 hours of operational time.

By analyzing the distribution of distance between asynchronous (of beam) equidistant markers and bunch peaks it is possible to detect the wrong injection. Therefore an algorithm to notify operators of such wrong injection was developed and implemented into Per bunch intensity measurement system.

References

[1] Belohrad, D., et al. The LHC fast BCT system: a comparison of design parameters with initial performance. No. CERN-BE-2010-010. 2010.

[2] R. Bailey and P. Collier, “Standard filling schemes for various LHC operation modes,” CERN-LHC-Project-Note-323, Tech. Rep., 2003.

[3] Evans, Lyndon, and Philip Bryant. "LHC machine." Journal of instrumentation 3.08 (2008): S08001.

Upsilon suppression studies in Au+Au collisions at $\sqrt{s_{NN}} = 200$ GeV in the STAR experiment

Jaroslav Štorek*(storejar@fjfi.cvut.cz)*

1 Introduction

Quark-gluon plasma (QGP) is a special state of matter where quarks and gluons behave as a quasi-free particles. They can move freely within the QGP and are no longer bound within hadrons. It is believed that shortly after the Bing Bang all matter in the Universe existed in this kind of state. Therefore knowing properties of QGP is important for modelling of the evolution of the Universe.

The deconfined state of strongly interacting matter, QGP, is result of color screening. Sufficiently dense or sufficiently hot medium screens the color charges and causes dissociation of mostly light quark bound states. QGP can be created in heavy-ion collisions.

Quarkonia (bound states of heavy quark and anti-quark) are used to study the properties of QGP. They are usually created before QGP and interact with the dense QGP medium. Upsilons Υ ($b\bar{b}$) are used in this study because of less recombination.

2 Quarkonium production

Production of quarkonia is explained by several effects. Some of them cause suppression, while other cause enhancement. The focus of this study is the effect of anomalous suppression arisen from color screening in the QGP. However, other effects contribute and they have to be also understood.

The limit of the anomalous quarkonium dissociation can be expressed by Debye screening length r_D which is inversely proportional to temperature T, $r_D \sim 1/T$. When radius of a quarkonium state is bigger than r_D, state dissociates. Different excited quarkonium states have different radii, therefore they melt at different temperatures and can serve as thermometer of the collision.

The total production of a quarkonium state is the sum of directly produced quarkonia and feed-down quakonia. Decays of excited states (feed-down) contribute to observed quarkonia by 30% and 50% for J/Ψ and Υ recpectively [1]. On the other hand, coalescence of randomly encountered quark and anti-quark in QGP may lead to enhancement of quarkonium production (recombination).

Suppression and enhancement is evaluated by nuclear modification factor R_{AB} [2]. It is a ratio of chosen observable from A+B collisions to the same observable from p+p collisions scaled by the number of binary collisions. If $R_{AB} < 1$, there is suppression in A+B with respect to p+p.

There are other modifications of quarkonium production such as cold nuclear matter (CNM) effects. They also contribute to measured suppression of quarkonia but do not originate in QGP. These effects are studied in p+A collisions where colliding system is considered to be too small to create QGP. For instance, shadowing considers different parton distribution in a bound nucleon compared to a free nucleon. Or break-up in interactions with co-moving hadrons can lead to quarkonium suppression.

3 Recent STAR results

Solenoidal Tracker at Relativistic Heavy Ion Collider (STAR) is a detector located in Brookhaven National Laboratory which has detectors for particle identification and tracking with a large acceptance in $|\eta| < 1$ and $0 < \phi < 2\pi$. Advantage of STAR is that, due to rare production of b quark, recombination can be neglected [3]. Also co-mover absorption is generally expected to be negligible for Upsilon [4].

The dependance of nuclear modification factor $R_{\mathrm{pA,AA}}$ on number of participants N_{part} is shown in Fig. 1. QGP causes in Au+Au collisions substantial suppression of Υ(1S) and Υ(2S+3S) especially in high N_{part}. Indication of suppression due to CNM effects in p+Au is also observed.

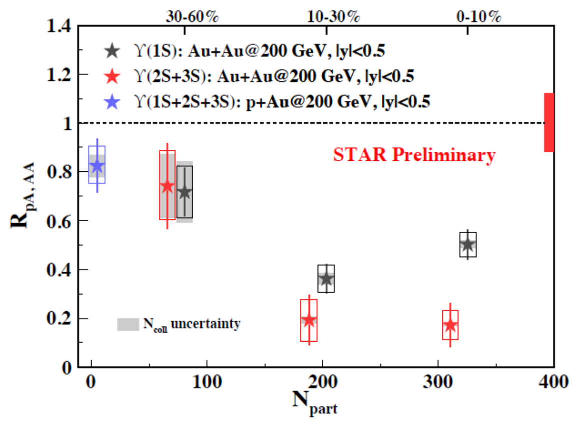

Figure 1: Dependance of nuclear modification factor $R_{\mathrm{pA,AA}}$ on number of partitipants N_{part} [5].

4 Υ production in Au+Au collisions at $\sqrt{s_{NN}} = 200$

The aim of author's work is Υ suppression study in Au+Au collisions at $\sqrt{s_{NN}} = 200$ GeV via dielectron channel. Data sample was recorded by STAR during run 2014 and comprises four times higher integrated luminosity (4nb^{-1}) than previous studies which implies high precision results.

This study serves as a continuation of previous study made by Oliver Matonoha. Currently analyzed new data sample was reconstructed without Heavy Flavour Tracker tracking because it is not needed for Υ studies.

Upsilons are reconstructed from e^+e^- pairs. Particles are identified from energy loss in Time Projection Chamber (TPC) and Barrel Electromagnetic Calorimeter. Electron's momentum is also determined from TPC. High Tower trigger selects only highly energetic electrons that likely originate from Υ. Only those pairs that come from the same interaction point with sufficient energy are chosen.

Fig. 2 shows Υ yield obtained only from low and mid luminosity dataset, which is 46% of the whole sample. Around 64 Υ(1S) and 21 Υ(2S+3S) was reconstructed.

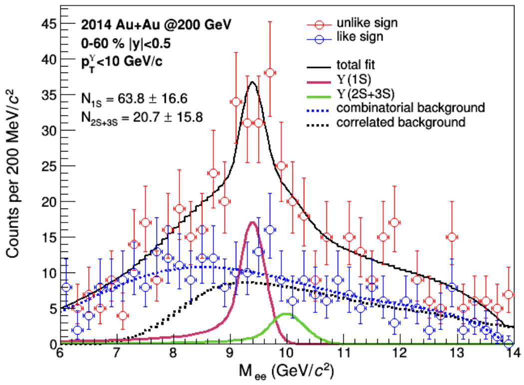

Figure 2: Dependance of number of pairs per 200 MeV/c^2 on pair mass. Total fit to unlike sign is composed of three parts: third-order Chebychev polynomial fit to like sign, the correlated background shape and 3 Crystal Ball functions, which are taken from Mont Carlo simulations. Drell-Yan process is not considered.

5 Summary and conclusion

To summarise, quarkonia can be used to study properties of the QGP created in heavy-ion collisions. Observed suppression of quarkonia production can be explained by dissociation in QGP and by other effects.

Obtained yield from low and mid luminosity dataset is slightly under 50% of what Oliver observed. Next, results will be combined with high luminosity dataset and compared to Oliver's yield with the same set of cuts.

References

[1] A. Andronic, F. Arleo, R. Arnaldi, EPJ C [online]. 2016, 76(3) [cit. 2019-02-25].

[2] V. Khachatryan. JHEP [online] 3 (2017) [cit. 25. 3. 2018]

[3] A. Emerick, X. Zhao, R. Rapp, EPJ A48 (2012) 72

[4] Z. Lin, C. Ko, PLB 503 (2001) 104

[5] P. Wang, Talk session presented at the Quark Matter 2018. [online] (2018)

A study of radiation tolerance of the monolithic silicon detectors

Václav Trličík*(vaclav.trlicik@gmail.com)*

1 Van Allen radiation belts

Van Allen belts are toroidal-shaped radiation belts around the Earth. Although there are consistently two of them, other can be observed in special conditions. They consist of the energetic charged particles predominantly originating from the solar winds captured in Earth's magnetic field and from cosmic rays.
Inner radiation belt (also called proton belt) usually stretches from 650 to almost 10 000 km above the surface but during strong solar flares the lower bound can drop down to 100 km [3]. It contains mainly electrons and energetic protons (several hundreds MeV [4]). These high energy protons are the result of beta decay of neutrons created by the collisions of cosmic rays with the molecules of thermosphere and exosphere.
Outer radiation belt extends from 13 000 to 65 000 km and is made mainly of high energetic electrons (up to 10 MeV)[5].
The inner radiation belt can significantly damage orbiting satellites and is therefore important to study its composition and influences.

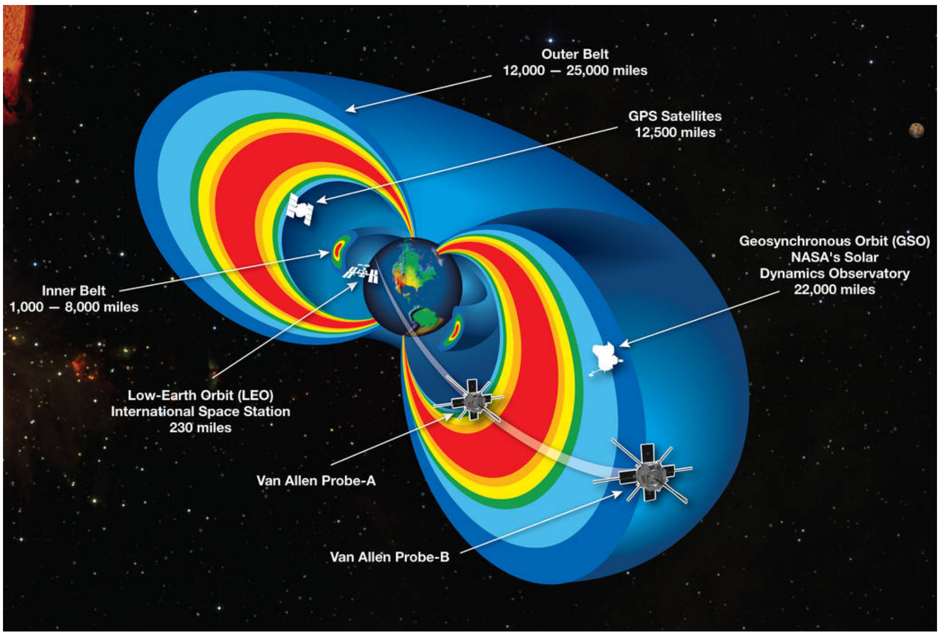

Figure 1: Illustration of Van Allen radiation belts around the Earth. Picture taken from [8].

2 Semiconductor detectors

Semiconductor is a material with conductive properties between conductors and insulators with atoms held together by covalent bonds. The bonding electrons can be splited into two separate groups (distincted by their energy), the valence and the conductive bands. Electrons in the valence band are bound rather tightly with the atom and cannot move freely. After adding energy (in form of heat or radiation for example) the atom can be vibrated enough to destroy the bond. The amount of energy required for this to happen in semiconductors is in order of eV (for comparison in isolants this energy is tens eVs). This energy is called band gap. The electron with enough energy to cross the band gap is free to move and is able to contribute to the conductive properties of the semiconductor. This group of electrons is called conductive band. In Fig.2 we can see the main difference between metal, semiconductor and insulator in terms of conductivity. E_F labels the Fermi's energy which is defined as the energy with which the electron has exactly 50% chance of being in conductive band or in valence band.
The main reason for using semiconductor detectors rather than other types is its compact dimensions, good energy resolution and high detection frequency. The main disadvantage is relatively high susceptibility to radiation damage.
These characteristics make the semiconductors viable option for detectors of cosmic radiation on the orbit of Earth and beyond.

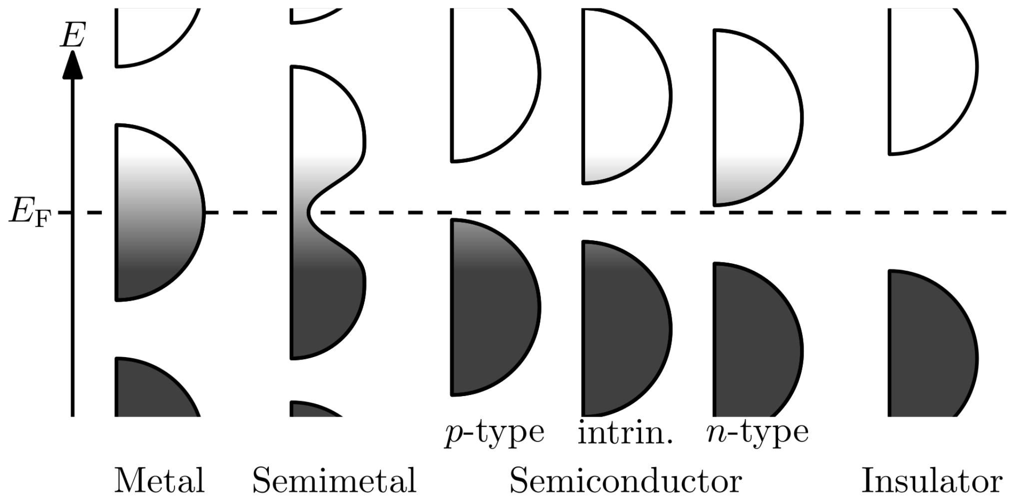

Figure 2: Schematic picture of the conductive (white) and valence (black) band as a function of energy. E_F is Fermi's energy. Picture taken from [7].

3 Radiation damage

There are two forms of radiation induced damage, cumulative and transient. The main cumulative damage is due to displacement of an atom from lattice. This is called point defect. Number of such defects in close proximity (along the radiation track) is called cluster defect. This type of damage is called Non Ionizing Energy Loss (NIEL). As a consequence the number of free charge pairs changes which then changes the reverse bias current. During the initial stage of irradiation the leakage current decreases due to creation of charged traps in the band gap. After longer irradiation the leakage current significantly increases as more and more energy levels in the band gap are introduced. It has been found the leakage current is dependent on radiation dose, the exposed volume and temperature.

$$i_l \propto T^2 \exp - \frac{E}{2kT} \tag{1}$$

On the other hand the transient radiation damage is a single event effect caused by strongly ionizing particle. Along its path the particle creates many electron-hole pairs which can lead to current pulse. This pulse can change the information in memory cells. The obvious consequence of leakage current is the increase of noise and signal degradation. To some extend this can be compensated by cooling down the device because of strong dependence on temperature as shown in (1).

References

[1] NASA. (2019). Van Allen Probes Spot an Impenetrable Barrier in Space. [online] Available at: https://www.nasa.gov/content/goddard/van-allen-probes-spot-impenetrable-barrier-in-space [Accessed 12 Mar. 2019].

[2] Science.nasa.gov. (2019). Van Allen Probes Discover a New Radiation Belt — Science Mission Directorate. [online] Available at: https://science.nasa.gov/science-news/science-at-nasa/2013/28feb_thirdbelt/ [Accessed 12 Mar. 2019].

[3] Space Environment Standard ECSS-E-ST-10-04C — ESA Requirements and Standards Division. November 15, 2008, 59. Retrieved 12 Mar. 2019.

[4] Freden, S. C., and White, R. S. (1960), Particle fluxes in the inner radiation belt, J. Geophys. Res., 65(5), 1377–1383, doi:10.1029/JZ065i005p01377.

[5] Brautigam, D. H., and Albert, J. M. (2000). Radial diffusion analysis of outer radiation belt electrons during the October 9, 1990, magnetic storm. Journal of Geophysical Research: Space Physics, 105, 291-309.

[6] AHMED, Syed Naeem. Physics and engineering of radiation detection. Boston: Academic Press, 2007. ISBN 978-0-12-045581-2.

[7] Nanite. “Semiconductor” Wikipedia, Wikimedia Foundation, 19 Mar. 2019, en.wikipedia.org/wiki/Semiconductor#/media/File:Band_filling_diagram.svg .

[8] Zell, Holly. “Radiation Belts with Satellites.” NASA, NASA, 23 Mar. 2015, www.nasa.gov/mission_pages/sunearth/news/gallery/20130228-radiationbelts.html.

Central Exclusive Production in proton-proton collisions at the STAR experiment

Tomáš Truhlář *(truhltom@fjfi.cvut.cz)*

1 Introduction

In 2017, The STAR experiment at the Relativistic Heavy Ion Collider (RHIC) measured proton-proton collisions at the center-of-mass energy $\sqrt{s} = 510$ GeV to study Central Exclusive Production process $pp \rightarrow pXp$ through Double IPomeron Exchange mechanism. The mechanism and the production will be explained in this article.

2 Double IPomeron Exchange

Double IPomeron Exchange (DIPE) mechanism in proton-proton collisions is a process when each proton emits a IPomeronan two IPomerons fuse and produce neutral state X and colliding protons emerge intact. The process is shown at Fig. 1. The process could be also describe by eg.: (1), where $\overset{\Delta\eta_1}{\oplus}$, $\overset{\Delta\eta_2}{\oplus}$ represent two gaps in pseudorapidity. Fig. 2 illustrate location of particle in the pseudorapidity and azimuthal angle. There are two rapidity gap, which separate **central** state X from the outgoing protons.

$$p + p \rightarrow p \overset{\Delta\eta_1}{\oplus} X \overset{\Delta\eta_2}{\oplus} p \tag{1}$$

At RHIC energies DIPE with $\pi^+\pi^-$ expected to be dominant. In this article we further focus only on $p + p \rightarrow p\pi^+\pi^-p$. From the conservation of momentum the total transverse momentum of all outgoing particle should be zero. For this reason, we define missing transverse momentum $p_{\mathsf{T}}^{miss} = (\vec{p}_1 + \vec{p}_2 + \vec{\pi}_+ + \vec{\pi}_-)_{\mathsf{T}}$ and events with small[1] p_{T}^{miss} are called **exclusive**.

3 Experimental setup

The STAR experiment has unique capabilities to measure central exclusive production. The Time Projection Chamber provides high-resolution tracking of charged particles and through the measurement of dE/dx and Time-of-Flight STAR is capable of precise particle

[1]Typically p_{T}^{miss} smaller than 100 MeV

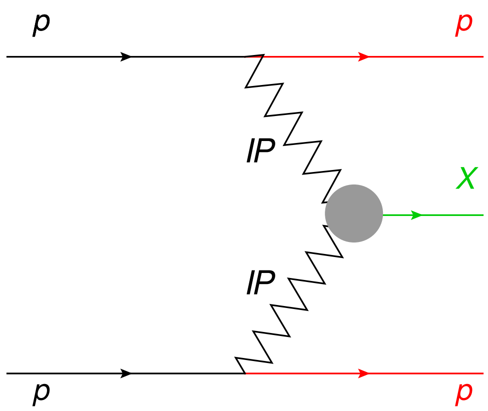

Fig. 1: The schema of Double IPomeron Exchange (DIPE) mechanism in proton-proton collisions.

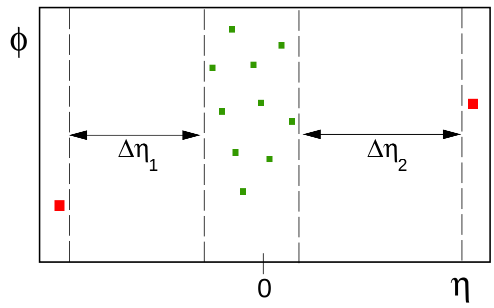

Fig. 2: The illustration of location of particle in the pseudorapidity and azimuthal angle in the central exclusive production.

identification. Forward rapidity is covered by Beam-Beam Counters to ensure rapidity gap and Silicon Strip Detectors in Roman Pots are used for measuring of forward protons.

Since 2015, Roman Pot Phase II* has been operating at the STAR experiment. There are 8 Silicon Strip Detector packages with active area about 79 mm × 49 mm installed in Roman Pot vessels. Package contains 4 SSDs (2 x-type and 2 y -type) with spatial resolution approx. 30 μm. Detectors are mounted in 4 stations. There are 2 stations on each site of STAR central detector, 15.8 m and 17.6 m from the interaction point. Each station composed of 2 vertically-oriented Roman Pots (above and below the beamline). Fig. 3 illustrate the layout of Silicon Strip Detectors at the STAR experiment.

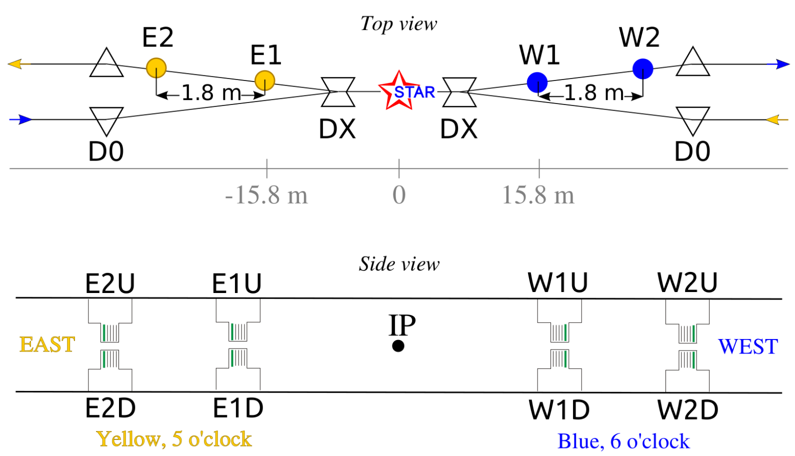

Fig. 3: The illustration of the layout of Silicon Strip Detectors at the STAR experiment.

4 Recent results

The most recent results were obtained from data measured in the STAR experiment at the RHIC in p-p collisions at $\sqrt{s} = 200$ GeV in 2015.

The invariant mass spectra of exclusively produced $\pi^+\pi^-$ pairs compared with some models of non-resonant CEP are shown in Fig. 4. Qualitatively good comparison between models predicted $\mathrm{d}\sigma/\mathrm{d}m(\pi^+\pi^-)$ and data is seen up to 0.7 GeV. This observation is consistent with the expectation of no narrow resonances in this mass range. The sharp drop of the cross section preceded with the peak below 1 GeV is might be due to $f_0(980)$ interference with production amplitude opposite in phase to $\pi^+\pi^-$ continuum. The peak between 1-1.5 GeV is probably from $f_2(1270)$ and maybe with possible contribution of $f_0(1370)$, whereas the rapid drop of the cross section at 1.5 GeV may be caused by $f_0(1500)$ interference with the remaining states [1].

In general, models of non-resonant CEP can not describe the data, which agrees with expectation of significant role of resonance production.

In run 2017 new data at higher center-of-mass energy of $\sqrt{s} = 510$ GeV were collected, which allow comparison of the DIPE in different kinematic regions.

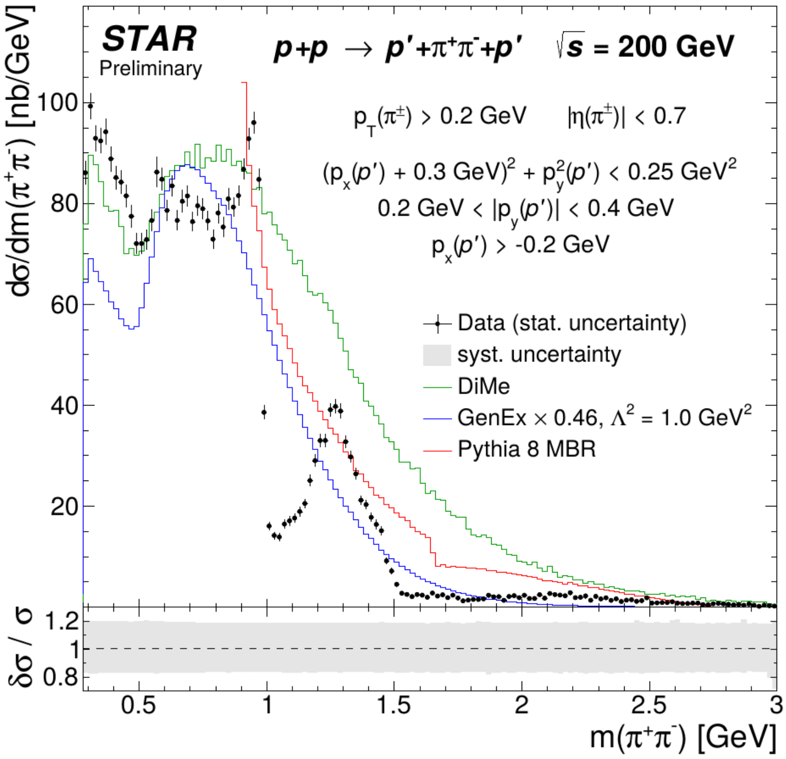

Fig. 4: Differential fiducial cross section as a function of invariant mass of $\pi^+\pi^-$ compared with some models of non-resonant CEP [1].

References

[1] SIKORA, Rafal. *Recent results on Central Exclusive Production with the STAR detector at RHIC* [online]. 2018 [cit. 201-02-20]. Available from: eprint arXiv:1811.03315

Multiplicity Fluctuations and Resonances in Heavy-Ion Collisions

Josef Uchytil *(Josef.Uchytil@fjfi.cvut.cz)*

The number of particles produced in ultra-relativistic nucleus-nucleus collisions is well described by the statistical model. In this model, the particle yields depend on temperature and chemical potential. However, statistical physics can also predict multiplicity fluctuations, which can subsequently be compared to experimental data. The aim of my talk was to provide information on how to compute multiplicity fluctuations along with higher moments of the multiplicity distribution using the central statistical moments. Furthermore, said moments of the multiplicity distribution in a hadron resonance gas model were investigated for both the chemical equilibrium and the chemical non-equilibrium, where the generation of temperature-dependent chemical potentials for each stable particle species was assumed. Finally, the results in form of the temperature dependence of the moments of the proton number distribution at chemical non-equilibrium were introduced for relevant cool-down scenarios based on the data from the RHIC BES programme.

The Quark-Gluon Plasma (QGP) is a state of matter where partons are *deconfined*, i. e. not confined in hadrons. Deconfinement is phenomenologically (i. e. within the QCD framework) defined as a phase transition. The phase transition is fully described (at sufficiently high collision energies) by a set of two parameters, these being the temperature T and the baryo-chemical potential μ_b.

As the HRG models reproduce the equilibrium lQCD results for the lowest order susceptibilities and their ratios (see further text) reasonably well [3] [7], we may further restrict on using the HRG model only. Statistical hadronization models have been successfully used to describe the data on hadron multiplicities in relativistic nucleus-nucleus (A+A) collisions [2]. In A+A collisions, the grand canonical ensemble (GCE) is preferred, whereas the canonical ensemble (CE) or the microcanonical ensemble (MCE) have been used for describing the $pp, p\bar{p}$ and e^+e^- collisions.

It has been shown that the moments of net-particle multiplicity distributions from the experiment can be related to susceptibilities of conserved charges calculated on the lattice [3]. Therefore, chemical freeze-out parameters can be directly determined in the thermally equilibrated GCE approach on the lattice without having to rely on statistical models. This makes said moments - which immediately lead to said fluctuations - a powerful tool in determination of the freeze-out parameters.

1 Calculation of the statistical moments within the Statistical Model

Statistical moments are an important mathematical tool used to describe and calculate multiplicity fluctuations in the statistical model. The m-th central moment $\varphi_m(X)$, where $m \in \mathbb{N}$ is defined as follows:

$$\varphi_m(X) = E(X - EX)^m$$

where EX is the mean value of the statistical quantity X. We will further concentrate on the quantities defined by the first four moments only, as those are of great significance. They are defined and called as follows:

mean: $M = \varphi_1$
variance: $\sigma^2 = \varphi_2$
skewness: $S = \varphi_3/\varphi_2^{3/2}$
kurtosis: $\kappa = \varphi_4/\varphi_2^2 - 3$

The constant -3 may or may not be added to kurtosis, which depends on whether we want the kurtosis of the Gauss distribution to be equal to zero. In our calculations, this factor is accounted for.

2 Fluctuations in a hadron resonance gas model with chemical equilibrium

We may describe fluctuations in the number of particles of species i in a thermally and chemically equilibrated Hadron Resonance Gas (HRG) using the corresponding susceptibilities defined as

$$\chi_l^{(i)} = \frac{\partial^l (P/T^4)}{\partial(\mu_i/T)^l} \, |_T \tag{1}$$

where $l \in \mathbb{N}$ and

$$P/T^4 = \frac{1}{VT^3} \sum_i \ln Z_{m_i}^{M/B}(V, T, \mu_B, \mu_Q, \mu_S).$$

The susceptibilities can be related to the cumulants of the multiplicity distribution of particle i via

$$\chi_1^{(i)} = \frac{1}{VT^3} \langle N_i \rangle_c = \frac{1}{VT^3} \langle N_i \rangle \tag{2}$$

$$\chi_2^{(i)} = \frac{1}{VT^3} \left\langle (\Delta N_i)^2 \right\rangle_c = \frac{1}{VT^3} \left\langle (\Delta N_i)^2 \right\rangle \tag{3}$$

$$\chi_3^{(i)} = \frac{1}{VT^3} \left\langle (\Delta N_i)^3 \right\rangle_c = \frac{1}{VT^3} \left\langle (\Delta N_i)^3 \right\rangle \tag{4}$$

$$\chi_4^{(i)} = \frac{1}{VT^3} \left\langle (\Delta N_i)^4 \right\rangle_c = \frac{1}{VT^3} \left(\left\langle (\Delta N_i)^4 \right\rangle - 3 \left\langle (\Delta N_i)^2 \right\rangle^2 \right) \tag{5}$$

where $\Delta N_i = N_i - \langle N_i \rangle$ and the subscript c denotes the corresponding cumulant value.

It is obvious that the first three cumulants are equal to the corresponding central moments, but the fourth cumulant is given by a combination of fourth and second central moments.

3 Fluctuations in a hadron resonance gas model with chemical non-equilibrium

Let us now perform the following denotations:

· $i \ldots$ all particles (resonances) included in the model
· $j \ldots$ j-th stable particle
· $A \ldots$ set of all stable particles
· $A_B \ldots$ set of stable baryons
· $N_{ji} \ldots$ average number of the j-th stable particle produced by channel i, equivalent to d_i^σ in 4.1
· $\mu_j \ldots$ chemical potential of stable particle j obtained as described in 4.1
· $m_i \ldots$ mass of resonance i
· $d_i \ldots$ isospin degeneracy of the i-th particle

As we shall further concentrate on baryons only, we may write the logarithm of the partition function for the i-th resonance as

$$\ln Z^B_{m_i}(V, T, \vec{\mu}) = \frac{V d_i}{(2\pi)^3} \int d^3k \ln \left(1 + \exp\left(\frac{\sum_{j \in A} N_{ji}\mu_j}{T} \right) \exp\left(-\frac{\sqrt{k^2 + m_i^2}}{T} \right) \right). \quad (6)$$

3.1 Ratios of susceptibilities

According to [7], the thermodynamic susceptibility χ_l of particle species a is given by

$$\chi_l^{(a)} = \frac{\partial^l (P/T^4)}{\partial(\mu_a/T)^l} = T^l \frac{\partial^l (P/T^4)}{\partial \mu_a^l}. \quad (7)$$

For partial pressure P/T^4 given by

$$\frac{P}{T^4} = \frac{1}{VT^3} \ln Z(V, T, \vec{\mu}) \quad (8)$$

which can be recast as

$$\frac{P}{T^4} = \frac{1}{2\pi^2 T^2} \sum_i \sum_{k=1}^{+\infty} d_i m_i^2 \frac{(-1)^{k+1}}{k^2} \exp\left(\frac{k}{T} \sum_{j \in A} N_{ji}\mu_j \right) K_2\left(\frac{k m_i}{T} \right), \quad (9)$$

Eq. (7) can be rewritten as

$$\chi_l^{(a)} = \frac{1}{2\pi^2 T^2} \sum_i \sum_{k=1}^{+\infty} d_i m_i^2 (-1)^{k+1} k^{l-2} N_{ai}^l \exp\left(\frac{k}{T} \sum_{j \in A} N_{ji}\mu_j \right) K_2\left(\frac{k m_i}{T} \right). \quad (10)$$

Obviously, the ratio of any two thermodynamic susceptibilities of the same particle species a, denoted $\chi_l^{(a)}$ and $\chi_n^{(a)}, l \neq n$, can be written as

$$\frac{\chi_l^{(a)}}{\chi_n^{(a)}} = \frac{\sum_i \sum_{k=1}^{+\infty} d_i m_i^2 (-1)^{k+1} k^{l-2} N_{ai}^l \exp\left(\frac{k}{T} \sum_{j \in A} N_{ji} \mu_j\right) K_2\left(\frac{k m_i}{T}\right)}{\sum_i \sum_{k=1}^{+\infty} d_i m_i^2 (-1)^{k+1} k^{n-2} N_{ai}^n \exp\left(\frac{k}{T} \sum_{j \in A} N_{ji} \mu_j\right) K_2\left(\frac{k m_i}{T}\right)}. \tag{11}$$

4 Results

The derived formulae will now be implemented using data from DRAGON with the newest PDG update. The calculations will be performed for the most central $Au + Au$ collisions (centrality 0-5 and 5-10) and for seven collision energies, these being $\sqrt{s_{NN}} = 7.7, 11.5, 19.6, 27.0, 39.0, 62.4, 200$ GeV. For our purposes, the ratio fits (GCER) have been used, for which there are always corresponding chemical freeze-out parameters for grand canonical ensemble. The temperature dependencies of the (net-)proton number densities $n = T^3 \chi_1$ and the ratios of thermodynamic susceptibilities $\omega = \frac{\chi_2}{\chi_1}$, $S\sigma = \frac{\chi_3}{\chi_2}$ and $\kappa\sigma^2 = \frac{\chi_4}{\chi_2}$ were presented for each of the collision energies and each centrality. For the sake of brevity, the detailed results were omitted in this review. An interested reader is therefore kindly referred to my Master's Thesis [8], where the results are presented and commented on in detail.

References

[1] W. Florkowski: *Phenomenology of Ultrarelativistic Heavy-Ion Collisions*, World Scientific, Singapore 2010

[2] V. V. Begun et al.: *Multiplicity fluctuations in hadron resonance gas*, Phys. Rev. C **74** (2006) 044903

[3] P. Alba et al.: *Sensitivity of multiplicity fluctuations to freeze-out conditions in heavy ion collisions*, Phys. Rev. C **92** (2015) 064910

[4] G. Torrieri, J. Letessier, J. Rafelski: *SHAREv2: Fluctuations and comprehensive treatment of decay feed-down*, Comput. Phys. Commun. **175** (2006) 635

[5] G. Torrieri, S. Jeon, J. Rafelski: *Particle yield fluctuations and chemical nonequilibrium in Au+Au collisions at* $s_{NN}^{1/2} = 200$ *GeV*, Phys. Rev. C **74** (2006) 024901

[6] H. Bebie, P. Gerber, J. L. Goity, H. Leutwyler: *The role of the entropy in an expanding hadronic gas*, Nucl. Phys. B378 (1992) 95

[7] M. Nahrgang et al.: *Impact of resonance regeneration and decay on the net proton fluctuations in a hadron resonance gas*, Eur. Phys. J. C(2015) 75:573, DOI 10.1140/epjc/s10052-015-3775-0, 1 Dec 2015

[8] J. Uchytil: *Multiplicity fluctuations and resonances in heavy ion collisions*, Master's Thesis (Ing.), Czech Technical University in Prague, Faculty of Nuclear Sciences and Physical Engineering, Department of Physics, 7 Jan 2019

Production of open-charm hadrons in Au+Au collisions at $\sqrt{s_{\mathrm{NN}}} = 200$ GeV measured by the STAR experiment

Jan Vaněk *(vanek@ujf.cas.cz)*

Charm quarks are commonly used as a probe of the Quark Gluon Plasma (QGP), since they are created at very early stages of ultra-relativistic heavy-ion collisions, during the hard partonic scattering. Measurements of open-charm hadrons production allow direct access to charm quark production and can therefore be used to study the properties of the QGP.

Decay channel	$c\tau$ [μm]	BR [%]
$\mathrm{D}^+ \rightarrow \mathrm{K}^-\pi^+\pi^+$	311.8 ± 2.1	9.46 ± 0.24
$\mathrm{D}^0 \rightarrow \mathrm{K}^-\pi^+$	122.9 ± 0.4	3.93 ± 0.04
$\mathrm{D}_s^+ \rightarrow \phi\pi^+ \rightarrow \mathrm{K}^-\mathrm{K}^+\pi^+$	149.9 ± 2.1	2.27 ± 0.08
$\Lambda_c^+ \rightarrow \mathrm{K}^-\pi^+\mathrm{p}$	59.9 ± 1.8	6.35 ± 0.33

Table 1: Summary of open-charm hadrons measured at STAR using the HFT. The left column contains decay channels used for the reconstruction, $c\tau$ is the mean lifetime of a given hadron, and BR is the branching ratio. Numbers are taken from Reference [1].

The STAR experiment is able to directly reconstruct the open-charm hadrons via their hadronic decay channels thanks to excellent spatial resolution of the Heavy Flavor Tracker (HFT) and state of the art tracking and particle identification enabled by the Time Projection Chamber (TPC) and the Time Of Flight (TOF) detectors. The list of open-charm hadrons presented in these proceedings and their basic properties are listed in the Table 1.

One of the most straightforward ways to quantify the charm quark interaction with the QGP comparing open-charm mesons production in heavy-ion and p+p collisions using the nuclear modification R_{AA}. Figure 1 shows the R_{AA} as a function of p_{T} for D^0 and $\mathrm{D}^{\pm}$ mesons in 0-10 % central Au+Au collisions. The high p_{T} open-charm mesons show significant suppression, suggesting strong interaction of the charm quarks with the medium.

Another way to study the charm quark interaction with the QGP, is to measure the elliptic flow v_2 of open charm mesons. As can be seen in the left panel of Figure 2, the magnitude of v_2 of D^0 mesons is similar to that of light flavor hadrons in high p_{T} region.

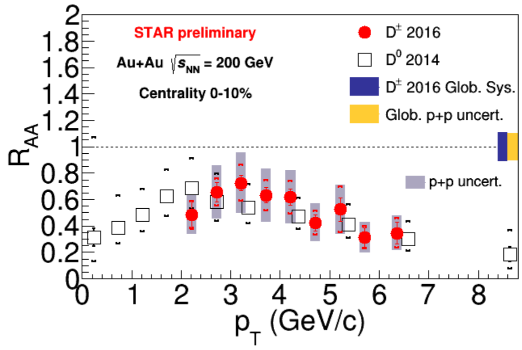

Figure 1: R_{AA} of D^0 [2] and $\mathrm{D}^{\pm}$ mesons as a function of p_{T} for 0-10% most central Au+Au collisions. The reference is combined $\mathrm{D}^{\star}$ and D^0 measurement in p+p at $\sqrt{s} = 200$ GeV [3].

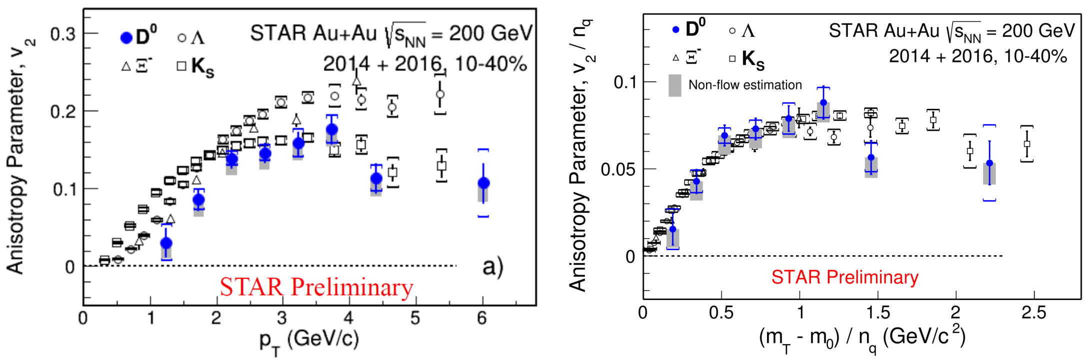

Figure 2: **(left)** The elliptic flow v_2 of D^0 mesons and light flavor hadrons [4] as a function of p_{T} in semi-central Au+Au collisions. **(right)** The elliptic flow v_2 divided by the umber of constituent quarks n_{q} as a function of $(m_{\mathrm{T}} - m_0)/n_{\mathrm{q}}$, where m_{T} is the transverse mass and m_0 is the rest mass. The v_2 of D^0 mesons and light flavor hadrons follows the NCQ scaling.

For low p_{T}, a mass ordering of v_2 is observed. It is also interesting to divide the v_2 by number of constituent quarks n_{q} and plot it as a function of $(m_{\mathrm{T}} - m_0)/n_{\mathrm{q}}$, where m_{T} is the transverse mass and m_0 is the rest mass. This dependency is shown in the right panel of Figure 2. All plotted particle species are on top of each other, which is called the Number of Constituent Quarks (NCQ) scaling. The fact that D^0 mesons follow the NCQ scaling suggests strong interaction of the charm quarks with the QPG and that they might be in thermal equilibrium with the medium at time of hadronization.

The hadronization process itself also plays very important role in open-charm hadrons production in heavy-ion collisions. For that reason, STAR has measured the $\Lambda_{\mathrm{c}}/\mathrm{D}^0$ ratio as a function of p_{T} (Figure 3, left panel) and a number of participants N_{part} (Figure 3, middle panel) in Au+Au collisions. Firstly, all data points are above the PYTHIA baseline, which means that the ratio is enhanced with respect to elementary collisions. This enhancement can be reasonably described by coalescence models [6, 7], but the Statistical Hadronization Model (SHM) [5] underpredicts the data. Another point is, that the ratio increases towards more central Au+Au collisions, suggesting that the enhancement is caused by the presence of the QGP. At the same time, the ratio increases above unity moving to low p_{T} region. This is very important for explaining the suppression of the low p_{T} D^0 mesons shown in Figure 1.

For better understanding of the charm quark hadronization process, STAR has also

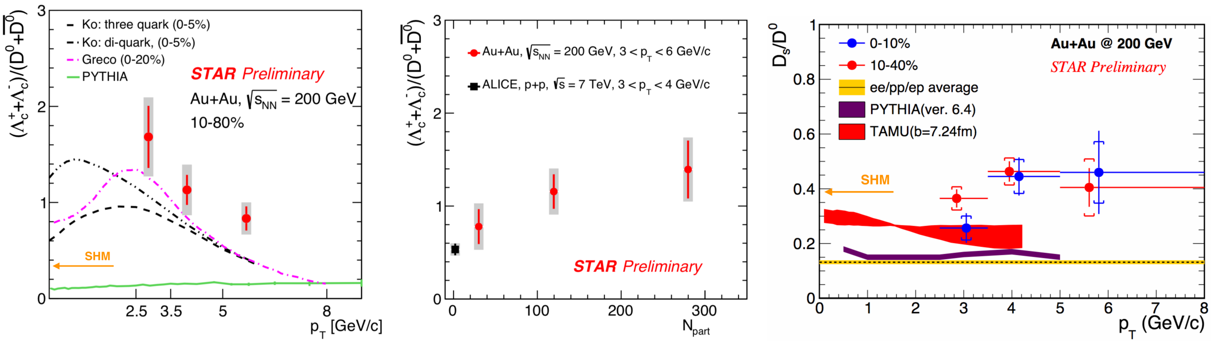

Figure 3: **(left)** The Λ_c/D^0 ratio as a function of p_T and **(middle)** N_{part} for semi-central Au+Au collisions at $\sqrt{s_{NN}} = 200\,\text{GeV}$. The p_T dependence is compared to PYTHIA, Statistical Hadronization Model (SHM) [5], and to coalescence models [6, 7], the N_{part} dependence is compared to p+p at $\sqrt{s} = 7$ TeV measurement by the ALICE experiment at the LHC [8]. **(right)** The D_s/D^0 ratio as a function of p_T. The data are compared to PYTHIA, combined e+e, e+p and p+p data [9], SHM [5] and TAMU model [10].

measured the D_s/D^0 ratio as a function of p_T, as shown in the right panel of Figure 3. Similarly to the Λ_c/D^0 ratio, an enhancement compared to elementary collisions (combined e+e, p+p and e+p) [9] and PYTHIA is observed. This phenomenon can be well described by the SHM, the TAMU model [10] underpredicts the data points at the moment. Both measurements (Λ_c/D^0 and D_s/D^0 ratios) suggest that coalescence hadronization plays very important role in hadronization of charm quarks inside the QGP.

In conclusion, STAR has extensively studied open-charm hadron production in Au+Au collisions at $\sqrt{s_{NN}} = 200\,\text{GeV}$. All presented measurements were possible thanks to excellent spatial resolution of the HFT. These precise results will bring significant constrains on model calculation and will help with better description of charm quark production and hadronization in heavy-ion collisions.

References

[1] M. Tanabashi, *et al.*, *Phys. Rev. Lett.* **2018**, *98*, 030001

[2] J. Adam, *et al.*, arXiv:1812.10224v1.

[3] Adamczyk L. *et al.*, *Phys. Rev. D*, **2012**, *86*, 072013

[4] B. I. Abelev, *et al.*, *Phys. Rev. C* **2008**, *77*, 054901

[5] A. Andronic, *et al.*, *Phys. Lett. B* **2003**, *571*, 36-44

[6] Y. Oh, *et al.*, *Phys. Rev. C* **2009**, *79*, 044905

[7] S. Plumari, *et al.*, *Eur. Phys. J. C* **2018**, *78*, 348

[8] S. Acharya, *et al.*, *J. High Energ. Phys.* **2018**, *9*, 108

[9] M. Lisovyi, *et al.*, *Eur. Phys. J. C* **2017**, *76*, 397

[10] M. He, *et al.*, *Phys. Rev. Lett.* **2013**, *110*, 112301

Quantum many-body problem in nuclear physics

Petr Veselý *(p.vesely@ujf.cas.cz)*

The atomic nucleus is a self-bound complex many-body system composed of A interacting nucleons: Z protons, and N neutrons. Since the nucleons are composite objects made of quarks and gluons, the description of nuclear structure should be, in principle, based on the fundamental theory of strong interaction, the quantum chromodynamics (QCD). Despite the first pioneering attempts [1, 2], this goal is currently unreachable. Therefore, the theory of nuclear structure relies on models and approximations. The lightest nuclei with $A \leq 4$ are often solved within a non-perturbative approach - the Fadeev-Yakubovsky method [3]. However, for $A > 4$ we cope with the **many-body problem** which is **one of the most challenging open problems in modern physics**. Even after decades of research theoretical nuclear physics often provides only qualitative description of nuclear phenomena and lacks quantitative predictive power. This is very limiting for the understanding of many physical processes in which atomic nuclei play an important role including those in extreme environments, from interiors of nuclear reactors to neutron stars and stellar explosions. The exact solution of nuclear many-body problem would significantly advance our knowledge not only in nuclear physics but also in fundamental physics, astrophysics, and applied physics.

The nuclear many-body problem can be currently solved only approximately within various approaches. An enormous effort is devoted to the development of *ab initio* methods, see Refs. [4, 5] for recent reviews, such as the no-core shell model (NCSM), coupled cluster method, fermionic molecular dynamics approach, in-medium similarity renormalization group (IMSRG), self-consistent green's function theory (SCGF), green's function Monte Carlo method, auxiliary field diffusion Monte Carlo method (AFDMC). The mentioned *ab initio* methods are, however, limited by their applicability. In fact, either they are solvable only for very light nuclei or they describe only part of energy spectra and physical phenomena in the studied nuclei.

Another class of models, which are generally applicable throughout a whole nuclear chart, is based on the idea of nuclear mean field which was introduced in order to explain the existence of a shell structure in nuclei (i.e. sudden and discontinuous changes of the nucleon separation energies in vicinity of the so called magic numbers of protons and neutrons). Nucleus is described as a set of non-interacting nucleons which occupy single-particle levels in a mean-field potential. Then the total nuclear Hamiltonian is composed of the mean-field operator and of a residual interaction which includes all the operator terms neglected in the mean-field approximation.

The nuclear mean-field potential can be either of phenomenolgical type (for instance as harmonic oscillator potential), or can be generated selfconsistently from the interaction among the nucleons using for example the Hartree-Fock (HF) method for the closed-shell nuclei and the Hartree-Fock-Bogolyubov (HFB) method for the open-shell nuclei [6]. However, the mean field provides only very rough approximation of the nuclear structure description. Therefore, the total nuclear Hamiltonian has to be diagonalized in a Hilbert space which is spanned by the many-body wave function, which represent the unperturbed ground state, and by its excitations. Most simple methods which provide the total nuclear Hamiltonian diagonalization are the Tamm-Dancoff (TDA) and, especially, the random-phase (RPA) approximations [7]. In both methods, the nuclear states are obtained as linear combinations of 1particle-1hole (1p-1h) (in doubly closed shell nuclei) or two quasi-particle (2qp) (in open shell nuclei) operators, often called phonons, acting on an unperturbed (TDA) or correlated (RPA) ground state. However, excitations more complex than 1p-1h (2qp) are known to play an important role in the description of nuclear structure but only few approaches succeed to include them. Let us mention the second RPA (SRPA) [8, 9], second TDA (STDA) [10], the core-coupling RPA model using the density dependent Migdal δ-function force [11], quasiparticle-phonon model (QPM) [12], and relativistic quasiparticle time blocking approximation (RTBA) [13]. However, most of these approaches do not take into account the Pauli principle because of the quasiboson approximation adopted in RPA.

Recently, an alternative approach has emerged, the equation of motion phonon method (EMPM) [14]. This method keeps its applicability throughout a whole nuclear chart. It derives and solves iteratively a set of equations of motion to generate an orthonormal basis of multiphonon states built of phonons obtained in particle-hole or quasiparticle TDA. Such a basis simplifies the structure of the Hamiltonian matrix and makes feasible its diagonalization in large configuration and phonon spaces. The diagonalization produces at once the totality of eigenstates allowed by the dimensions of the multiphonon space. The formalism treats one-phonon as well as multiphonon states on the same footing, takes into account the Pauli principle, and holds for any Hamiltonian.

The EMPM in its first version was implemented in the particle-hole basis to describe the closed-shell nuclei and recently it has been extended to open-shell [15] and odd-mass nuclei [16]. The EMPM occures to be successful in confirming that the complex configurations, higher than 1p-1h (or 2qp in the open-shell nuclei) excitations of the mean field, are crucial for the description of nuclear ground states and their binding energies [17], the fragmentation and width of the giant dipole resonances [18, 19] and the low-lying energy states [15, 16, 20, 21]. It is, however, still unreachable to include the 4-phonon (or higher-phonon) configurations into the EMPM. It is expected that inclusion of such configurations is important in order to reach satisfactory nuclear structure description [17]. Such task is very challenging and calls for further effort.

References

[1] S. R. Beane, E. Chang, S. Cohen, W. Detmold, H. W. Lin, K. Orginos, A. Parreño, M. J. Savage, B. C. Tiburzi, Phys. Rev. Lett. 113, 252001, (2014)

[2] S. R. Beane, E. Chang, S. D. Cohen, W. Detmold, H. W. Lin, T. C. Luu, K. Orginos, A. Parreño, M. J. Savage, A. Walker-Loud, Phys. Rev. D 87, 034506, (2013)

[3] O. A. Yakubovsky, Sov. J. Nucl. Phys. 5, 937, (1967)

[4] W. Leidemann, G. Orlandini, Prog. Part. Nucl. Phys. 68, 158, (2013)

[5] S. Bacca, and S. Pastore, J. Phys. G: Nucl. Part. Phys. 41, 123002, (2014)

[6] M. Bender, P.-H. Heenen, P.-G. Reinhard, Rev. Mod. Phys. 75, 121, (2003)

[7] P. Ring, P. Schuck, The Nuclear Many-Body Problem, Springer-Verlag, (1980)

[8] J. Sawicki, Phys. Rev. 126, 2231 (1962)

[9] D. Gambacurta, M. Grasso, J. Engel, Phys. Rev. C 92, 034303 (2015)

[10] F. Minato, Phys. Rev. C 93, 044319, (2016)

[11] J. Dehesa, S. Krewald, J. Speth, Phys. Rev. C 15, 1858, (1977)

[12] V. G. Soloviev, Theory of Atomic Nuclei, Quasi-particle and Phonons, CRC Press, (1992)

[13] E. Litvinova, P. Ring, Phys Rev. C 73, 044328, (2006)

[14] D. Bianco, F. Knapp, N. Lo Iudice, F. Andreozzi, A. Porino, Phys. Rev. C 85, 014313, (2012)

[15] G. De Gregorio, F. Knapp, N. Lo Iudice, P. Veselý, Phys. Rev. C 93, 044314, (2016)

[16] G. De Gregorio, F. Knapp, N. Lo Iudice, P. Veselý, Phys. Rev. C 94, 061301(R), (2016)

[17] G. De Gregorio, J. Herko, F. Knapp, N. Lo Iudice, P. Veselý, Phys. Rev. C 95, 024306, (2017)

[18] F. Knapp, N. Lo Iudice, P. Veselý, F. Andreozzi, G. De Gregorio, A. Porrino, Phys. Rev. C 90, 014310, (2014)

[19] F. Knapp, N. Lo Iudice, P. Veselý, F. Andreozzi, G. De Gregorio, A. Porrino, Phys. Rev. C 92, 054315, (2015)

[20] G. De Gregorio, F. Knapp, N. Lo Iudice, P. Veselý, Phys. Rev. C 95, 034327, (2017)

[21] G. De Gregorio, F. Knapp, N. Lo Iudice, P. Veselý, Phys. Rev. C 97, 034311, (2018)

Production and Detection of Antihydrogen Atoms in the AEgIS Experiment

Alena Zemanová*(Alena.Zemanova@fjfi.cvut.cz)*

1 The AEgIS Experiment

The AEgIS Experiment belongs to the six currently working experiments in the Antiproton Decelerator (AD) hall at CERN (together with ALPHA, ASACUSA, ATRAP, BASE and GBAR). The location of all these experiments is in the zone inside the ring of the Antiproton Decelerator. AD, as an unique source of cold antiprotons in the world, is able to produce bunches of $3 \cdot 10^7$ $\bar{\mathrm{p}}$ with an energy of 5.3 MeV every ~ 120 seconds.

The primary scientific goal of the experiment is to directly measure the Earth´s local gravitational acceleration g on $\bar{\mathrm{H}}$ with 1% relative precision. The current aim of AEgIS is to form a cold antihydrogen beam at 100 mK.

The experiment itself works in several steps. At first, positrons are produced by a ^{22}Na source, whereupon they are cooled down, captured and accumulated. From the hardware point of view, the positron apparatus is located on the second floor of the experiment as can be seen in Figure 1.

The next step is the production of positronium (Ps). The Ps formation mechanism chosen by AEgIS uses a silica converter where positrons are implanted at about keV energy in the surface. The last part concerning positronium is its excitation to a high Rydberg state by laser excitation by a group of lasers whose wavelengths are tuned in the range 204-206 nm for the first step ($n = 3$), and 1680-1715 nm for the second step ($n = 15 - 17$).

After that, antihydrogen is finally pulsed-formed by a resonant charge exchange between Rydberg Ps and cold antiprotons. This step is the last one in the current experimental setup. Trapping and cooling of antiprotons occurs in the central region of the experimental apparatus, in two Penning-Malmberg traps. The first one, operating with a magnetic field of 4.46 T (designed to operate at 5 T) is used to catch antiprotons and to cool them via electron cooling. The second one with a magnetic field of 1 T is the $\bar{\mathrm{H}}$ production trap. Both can be seen in Figure 1.

2 Antihydrogen formation

Unlike other experiments in the AD, which rely on the traditional three-body recombination scheme for antihydrogen formation, the AEgIS experiment went in the direction of a

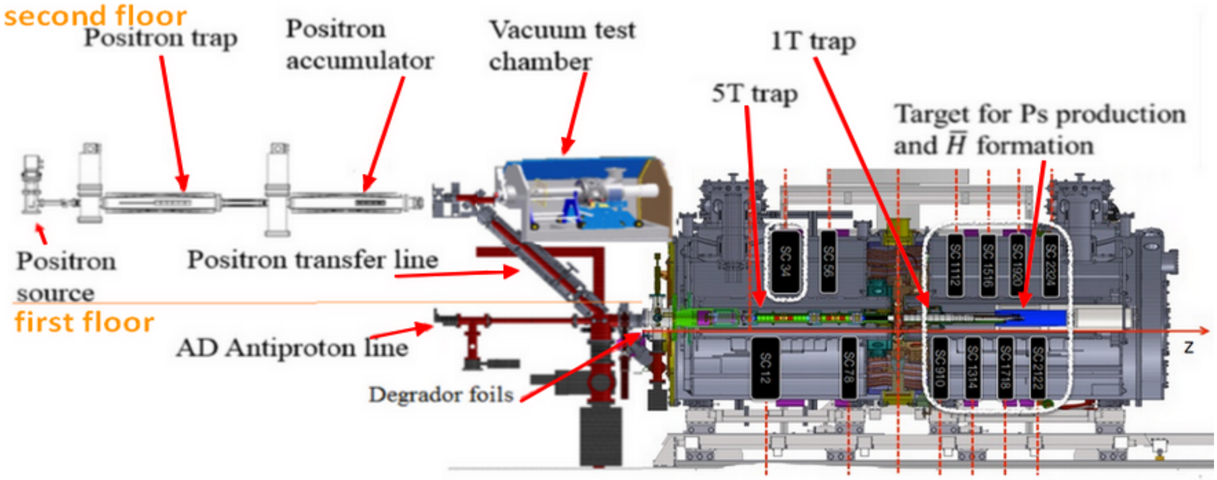

Figure 1: Schematic of the AEgIS apparatus.

pulsed production - antihydrogen is formed via a charge-exchange reaction:

$$Ps^* + \bar{p} \rightarrow \bar{H}^* + e^-,$$

where * stands for a high excited Rydberg state.

This reaction has the following advantages:

1. The cross section scales as $\sigma \propto n_{Ps}^4$, where n_{Ps} is the positronium principal quantum number.

2. The temperature of formed antihydrogen is given by the temperature of incoming antiprotons.

3. The principal quantum number of antihydrogen ($n_{\bar{H}}$) is determined by the quantum state n_{Ps} of positronium that formed it: $n_{\bar{H}} = \sqrt{2}n_{Ps}$.

The production itself takes place in the 1 T trap, which is divided into two smaller traps (on-axis - the storage trap and off-axis - the trap which allow positrons to reach the Ps target). A close up of this region can be seen in Figure 2. In the on-axis trap are antiprotons trapped, cooled and prepared for the oncoming Ps, which enters the production trap from above. The electrodes of the production trap are designed with small apertures to let Rydberg Ps atoms fly in. The Rydberg-exciting laser impinges on the Ps cloud orthogonally (see Figure 2).

3 Antihydrogen detection

Nowadays, the main system used for antihydrogen detection are scintillators placed around the main apparatus of the experiment. 12 external scintillator slabs are installed around the external surface of the vacuum chamber to monitor annihilations. All scintillators can be seen in Figure 1. Each scintillating slab is a cylindrical segment, about 100 mm in width, 20 mm in depth and made of plastic polystyrene doped with POPOP wavelength shifter. It covers a solid angle of about 3 % with respect to an annihilation happening in its centre. Each slab is optically coupled to two heavily shielded coincident photomultiplier tubes (PMTs).

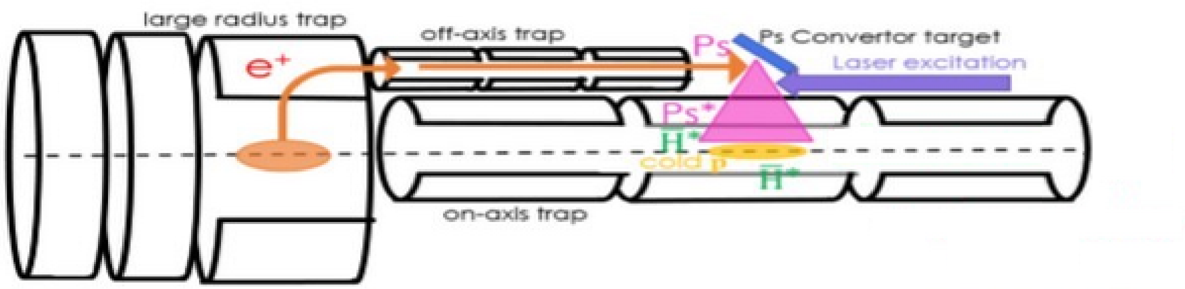

Figure 2: Schematic of the 1 T production region. The $\bar{\mathrm{p}}$ plasma is trapped on axis, whereas the positrons are loaded into the off-axis trap. The production target is placed off-axis, at about 2 cm distance from the on-axis trap.

From the analysis point of view it is difficult to distinguish between an annihilation of $\bar{\mathrm{p}}$ and $\bar{\mathrm{H}}$, because they are the same for this kind of statistics. The threshold for the voltage leading from the PMTs coincidences is used as a criteria. All measurements under a given threshold are called 'candidates'. Any candidates appearing within a given time range are interpreted as a detected antihydrogen atom.

Detection from scintillators copes with some problems: the main one is, that this is mainly a counting experiment, which means you have to take care of all the possible background interference. Furthermore, in this type of experiment statistics are very important and the experiment deals with very few events. Lastly, all possible errors (mainly systematic ones) need to be considered.

The main detector designed for antihydrogen formation is found around the production trap is called FACT (The Fast Annihilation Cryogenic Tracking detector). It is the only detector with vertex reconstruction capabilities, composed of 800 z-stacked rings of scintillating fibre arranged in four concentric layers around the production trap with an active region of about 300 mm in length. Each scintillating fibre is coupled to a plain fibre that carries the scintillation light to the external flange of the experiment, where it is read by a Multi-Pixel Photon Counter (MPPC) detector at room temperature. More details about this detector can be seen in [3]

However, this detector will need to be improved over the coming years in order to provide more accurate results for evidence of antihydrogen formation.

References

[1] AEGIS Collaboration: *Proposal for the AEGIS experiment at the CERN Antiproton Decelerator (Antimatter Experiment: Gravity, Interferometry, Spectroscopy)*, 2007. `http://cds.cern.ch/record/1037532/files/spsc-2007-017.pdf` [online 14/2/2019]

[2] Daniel Krasnický: *Antiproton Capture and Cooling for Production of Cold Antihydrogen*. Ph.D. Thesis, 2013.

[3] J. Storey et al.: *Particle tracking at 4K: the Fast Annihilation Cryogenic Tracking (FACT) detector for the AEgIS antimatter gravity experiment*. Nucl. Instrum. Methods Phys. Res., Sect. A, 732:437–441, 2013.